Dipl.-Ing. Beate Sudy

ESR-Spectroscopic Investigations on the Dynamics and Kinetics of Organic Radicals in Ionic Liquids

DISSERTATION

zur Erlangung des akademischen Grades

Doktorin der technischen Wissenschaften

eingereicht an der

Technischen Universität Graz

Betreuer

O.Univ.-Prof. Dipl.-Ing. Dr.rer.nat. Günter Grampp

Institut für Physikalische und Theoretische Chemie

Graz, Jänner 2015

EIDESSTATTLICHE ERKLÄRUNG

Ich erkläre an Eides statt, dass ich die vorliegende Arbeit selbstständig verfasst, andere als die angegebenen Quellen/Hilfsmittel nicht benutzt, und die den benutzten Quellen wörtlich und inhaltlich entnommenen Stellen als solche kenntlich gemacht habe. Das in TUGRAZonline hochgeladene Textdokument ist mit der vorliegenden Dissertation identisch.

15.01.2015
Datum

B. Sudy
Unterschrift

Acknowledgment

First of all, I want to thank my supervisor Prof. Günter Grampp for being a great teacher and bringing me to the Physical Chemistry. You, with your passion to chemistry, are one reason why I have started to study chemistry after my employment as a laboratory assistant at your institute.

I want to thank the Austrian Academy of Science to make my PhD study possible by financial support.

Very special thanks to my college and friend Kenneth Rasmussen for many hours you have spent to help me with my work and for proofreading. I am so happy to met you in my live!

Thanks to Helmut Lang for helping me to build my high pressure ESR cell and Helmut Eisenkölbl for supporting me in each data processing or electronic problem.

Thanks to my girls Hilde Freißmuth, Marion Hofmeister and Brigitte Bitschnau for being the best colleges ever. I will miss you!

Thanks Daniel Kattnig for providing me the great „Daniels hyperfitter“ ESR spectra simulation program.

Finally I want to thank the most important persons in my life. My husband, my children Maria and Konstantin and my mother for your love and understanding during the finale phase of my PhD study.

Abstract

The self-exchange reaction of the redox couples [TTF/$TTF^{\bullet+}$] and [TCNE/$TCNE^{\bullet-}$] has been investigated by ESR line broadening experiments in different Ionic liquids and organic solvents by variation of temperature and pressure. The question whether existing theories of organic solvents, especially the Marcus Theory, are applicable also to ionic liquids was the aim of this work.

Temperature dependent ESR- experiments yielded rate constants for the electron transfer reaction and activation energies. The self- exchange reaction of the redox couple [TTF/$TTF^{\bullet+}$] in ionic liquids is diffusion controlled and therefore permits no conclusions about the applicability of the Marcus theory. The solvent dynamics of the electron transfer reaction of [TCNE/$TCNE^{\bullet-}$] in ionic liquids seems to be comparable to organic solvents, but the calculation of the free Gibbs energy ΔG^* via the outer (λ_o) and inner (λ_i) sphere reorganization energy, as suggested by Marcus, seems to fail.

A high pressure ESR cell that offers ESR-measurements under elevated pressure up to 1000 bar has been constructed. Measurements of the rate constants of the redox couple [TTF/$TTF^{\bullet+}$] at elevated pressure deliver insights into the structure of ionic liquids.

Additionally measured was the electron transfer rates of the redox couples [TCNE/$TCNE^{\bullet-}$] and [DDQ/$DDQ^{\bullet-}$] in a special solvent mixture what offers the stabilization of solvent properties, like refractive index n_D and viscosity η by variation of the solvent dielectric constant ε_S.

Zusammenfassung

Mittels ESR Linienverbreitungsexperimente wurden Elektronen Selbstaustauschreaktionen der Redoxpaare [TTF/$TTF^{\bullet+}$] und [TCNE/$TCNE^{\bullet-}$] Temperaturabhängig und Druckabhängig in verschiedenen Ionischen Flüssigkeiten und organischen Lösungsmitteln untersucht. Im Rahmen dieser Arbeit galt es herauszufinden, ob aktuell gültige Theorien für organische Lösungsmittel, im Speziellen die Marcus Theorie, auch für Ionische Flüssigkeiten anwendbar ist.

Die Temperaturabhängigen ESR- Experimente lieferten Geschwindigkeitskonstanten und Aktivierungsenergien für den Elektronentransfer. Die Selbstaustauschreaktion des Redoxpaares [TTF/$TTF^{\bullet+}$] ist in Ionischen Flüssigkeiten diffusionskontrolliert was eine Interpretation über die Marcus Theorie unmöglich macht. Die Lösungsmitteldynamik der Elektronentransferreaktion von [TCNE/$TCNE^{\bullet-}$] scheint in den Ionischen Flüssigkeiten vergleichbar mit organischen Lösungsmitteln zu sein, aber die Berechnung der freien Gibbs Energien ΔG^* über die von Marcus vorgeschlagenen äußere (λ_o) und innere (λ_i) Reorganizationsenergie scheint fehlzuschlagen.

Eine Hochdruck-ESR-zelle wurde gebaut und ermöglichte damit druckabhängige ESR-Messungen bei erhöhtem Druck bis 1000 bar. Die gemessenen Geschwindigkeitsraten der Selbstaustauschreaktion von [TTF/$TTF^{\bullet+}$] bei höheren Drücken liefert Einblicke in die Struktureigenschaften der Ionischen Flüssigkeiten.

Zusätzlich wurde die Selbstaustauschreaktion der Redoxpaare [TCNE/$TCNE^{\bullet-}$] und [DDQ/$DDQ^{\bullet-}$] in einem speziellen Lösungsmittelgemisch untersucht. Dieses Lösungsmittelgemisch ermöglicht ein Konstanthalten bestimmter Löungsmitteleigenschaften wie Brechungsindex n_D und Viskosität η während die Dielektrizitätskonstante ε_S variiert.

1. Introduction

Within the present work the simplest kind of electron transfer reactions are investigated, the so called self-exchange reactions. These reactions describe the electron transfer of one single electron between two partners of a redox couple where the reactants and products are identical. The reaction appears without breaking or forming chemical bonds. Two versions of electron self-exchange reactions are relevant for this thesis. The electron self-exchange of one electron between a neutral molecule and its one electron reduced form (radical anion) and the reaction between a neutral molecule and its one electron oxidized form (radical cation). The reaction schemes below show the self-exchange reactions of the investigated redox couples. Reactions between tetracyanoethylene (TCNE) and its radical anion ($TCNE^{\bullet -}$)(see (1.1)), between 2,3-dichloro-5,6-dicyanobenzoquinone (DDQ) and its radical anion ($DDQ^{\bullet -}$) (see (1.2)) and between tetrathiavulvalene (TTF) and its radical anion ($TTF^{\bullet +}$) (see (1.3)).

$$TCNE + TCNE^{\bullet -} \rightleftharpoons TCNE^{\bullet -} + TCNE \quad \textbf{(1.1)}$$

$$DDQ + DDQ^{\bullet -} \rightleftharpoons DDQ^{\bullet -} + DDQ \quad \textbf{(1.2)}$$

$$TTF + TTF^{\bullet +} \rightleftharpoons TTF^{\bullet +} + TTF \quad \textbf{(1.3)}$$

Electron transfer reactions play an important role in organic synthesis as well as in biological processes like photosynthesis or electrochemistry, etc. The choice of the solvent for the electron transfer reactions is important. This has been established by the chemistry Nobel Prize winner in 1992, R. A. Marcus. He described the electron transfer reaction considering solvent properties such as the refractive index or the dielectric properties of the solvent. Solvent effects on the electron transfer reaction may be investigated by both implementation of suitable lab experiments in different solvents and by variation of the conditions like pressure and temperature. The experimental observables like rate constants and activation energies may afterwards be related to the corresponding equations of the theory. The applicability of the Marcus Theory has been proved many times for electron

transfer reactions in common organic solvents like e.g. acetonitrile etc. But what about ionic liquids (ILs)?

Room temperature ionic liquids (RTILs) have been focused on more and more in the last years because of their special properties. RTILs are liquid molten salts at room temperature and they have very good dissolving properties for inorganic and organic substances. Because of their non-volatility they are of interest to replace organic solvents in chemical processes. Most organic solvents are toxic and have a high vapor pressure. The low vapor pressure of ILs is therefore a big advantage and that is the reason why ILs are often called „green solvents“. This denotation leads rather to a misunderstandig because ILs are not really „green“. They are more or less toxic and have not yet been completely tested. The properties of ILs may be designed by the structure of the anion and the cation in the IL. This introduced a new field of research which has increased the number of known ILs in the recent years enormously. The ILs are primarily classified on the basis of their cations. The following picture presents possible IL cation classes whereas this work is only concerned with imodazolium based ILs.

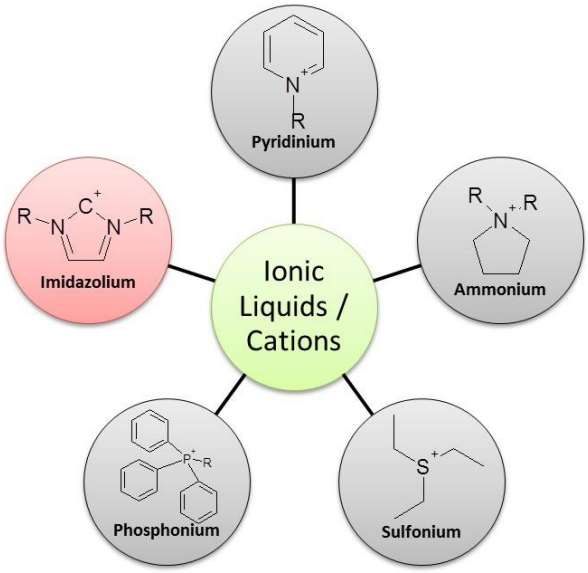

Figure 1.1: Common cations in ionic liquids.

The imidazolium based ILs can further be classified on the basis of their anion as can be seen in Figure 1.2. The investigations within this work is concentrated on the use of bis(trifluoromethylsulfonyl)imides and tetrafluoroborates.

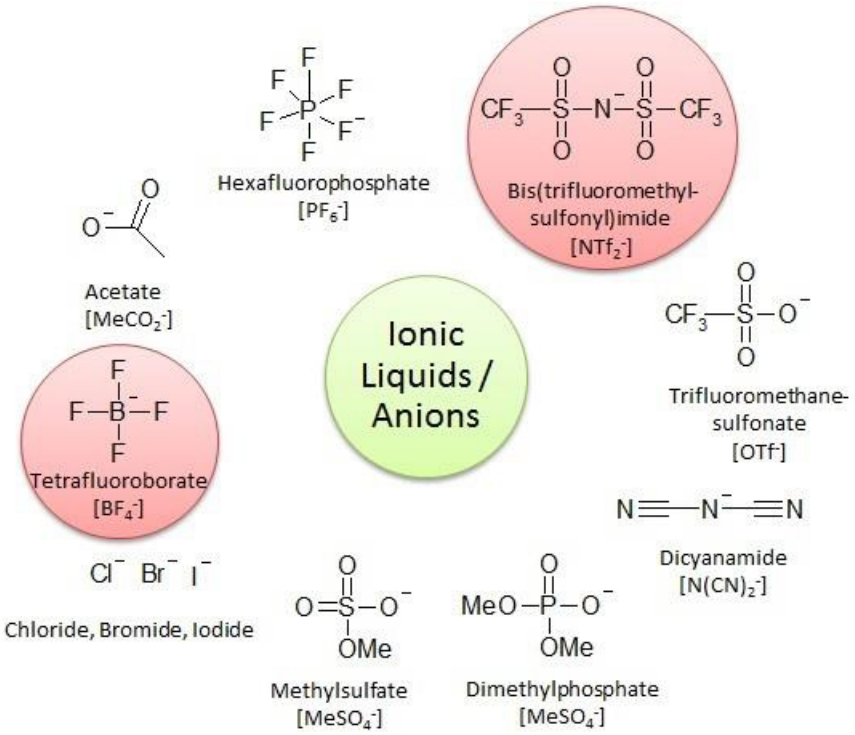

Figure 1.2: Common anions in ionic liquids.

Furthermore, ILs distinguish themselves completely from organic solvents. Organic solvents are composed of solvent molecules with certain polarities, whereas ILs are composed of discrete charged ions. This leads to very different solvent properties. For instance, viscosities of ILs are ten or more times higher than of common organic solvents. All of the mentioned differences between ILs and organic solvents lead to the consideration whether electron transfer reactions in ILs are comparable to ET reactions in organic solvents. During the electron transfer reactions, which are described in detail in chapter 2, the reactants are surrounded by solvent molecules of certain polarity. How the solvent molecules are oriented around the reactants depend on the charged nature of the reactants and solvent polarity (see Figure 1.3). The reaction scheme shows that the electron transfer reaction is composed of several steps during all of them the reactants, transition states and the products are surrounded by the solvent molecules. The solvent molecules must reorganize

according to each step, which is considered in Marcus Theory via the dielectric properties. The calculation of the energy required to rearrange the solvent molecules (outer-sphere reorganization energy, λ_o) includes the static dielectric constant ε_S and the refractive index n_D. The dielectric constant arises from the weakening of an external electrical field via polarisation effects.

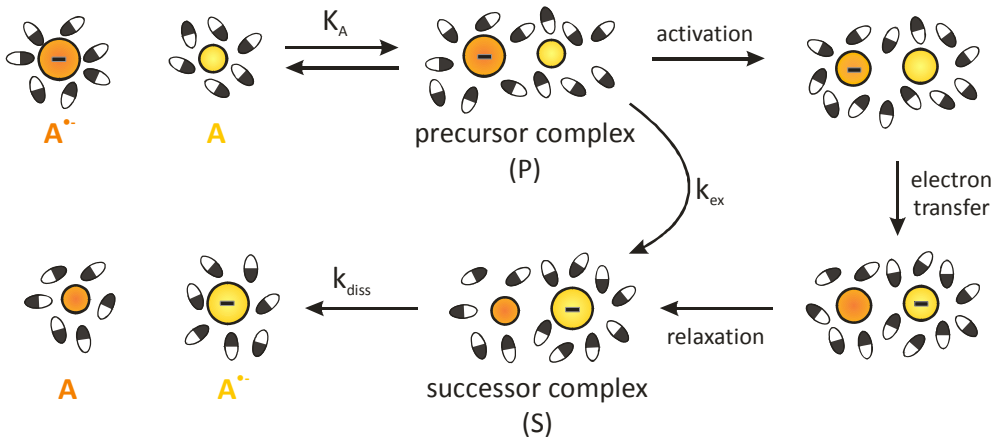

Figure 1.3: Electron self-exchange reaction in an organic solvent.

If we now try to imagine the same processes in ILs, this gives a totally different picture (see Figure 1.4). The cations and anions of the IL are arranged around the investigated redox couple but we do not know how they are rearranged during the electron transfer reaction. The ions bear positive and negative charges but have no polarity in the same sense as organic solvent molecules. It is possible to measure the dielectric constant of the ILs and there are already a lot of values published and available, but the origin of the weakening of an external electrical field cannot arise from polarisation effects like in organic solvents. Therefore, the use of the dielectric constant for calculating the reorganization of the solvent during the reaction in ILs is questionable. This is due to the fact that Marcus's approach to calculate the outer reorganization energy λ_o is based on a simple model which considered the solvent as a dielectric continuum and this is strictly not true for ILs.

Nevertheless, it was tried to use dielectric properties of ILs and the Marcus basic approach to prove the applicability of the Marcus Theory in ILs within this work.

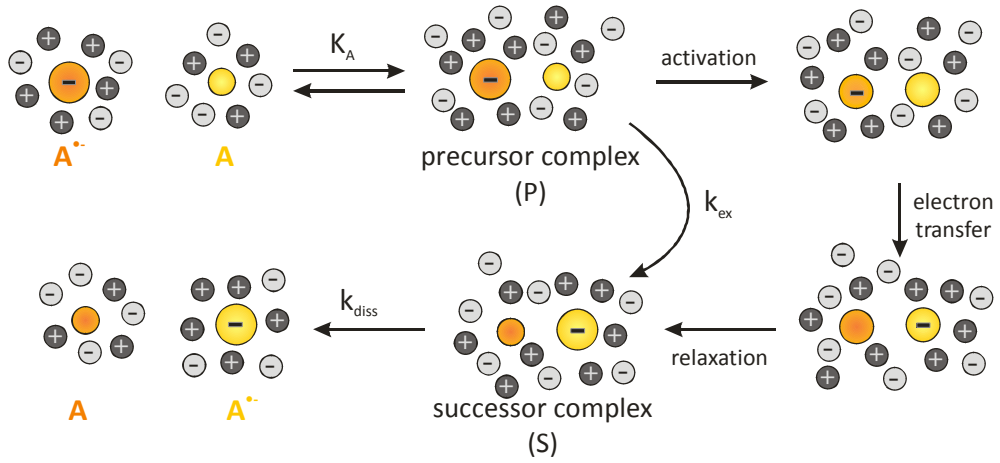

Figure 1.4: Electron self-exchange reaction in an ionic liquid.

One method to investigate such self-exchange reactions in different solvents is line broadening experiments by Electron Spin Resonance (ESR). ESR is a spectroscopic method which is only sensitive to paramagnetic species. This means that only substances with unpaired electrons, like in radicals, are detectable by ESR (see 2.6). The line shape changes by the occurring electron transfer reaction in dependence on the concentration of reactants and can therefore be used to determine rate constants for the observed reaction.

Temperature and pressure dependent ESR measurements are appropriate to prove the solvent dependencies on the rate constants and to receive activation energies and activation volumes. The ESR measurements at elevated pressure required the construction of an appropriate ESR cell within this work. With the custom-built ESR cell made of a special bent quartz capillary it was possible to measure up to 100 MPa (see 3.3.2). Temperature dependent measurement could be carried out by an existing temperature unit which offers measurements between 100 and 600K .

As mentioned before is the Marcus Theory a proven approach for investigating rate constants of redox reactions and their solvent dependence in organic solvents. But what

happens when the solvent is composed of several organic solvents? Is it possible to use the overall solvent properties of such solvent mixtures? For instance the overall dielectric constant measured in a mixture composed of different solvents may be different than the dielectric constants of the individual solvents. The Marcus Theory shall be used here to test a specially designed reaction medium composed of three different components. The aim of this solvent mixture is to vary only the dielectric constant while other solvent properties like the viscosity and the refractive index stay constant. In order to obtain this, propyl acetate and butyronitrile was used to set the dielectric constant and diethyl phthalate to adjust the viscosity (see chapter 3.1.8). Such solvent mixtures would provide a good tool for investigations on the dependence of the dielectric constant of chemical reactions. This could be very useful for other research areas such as photochemistry or electrochemistry.

2. Theory

2.1 Electron Transfer

Electron transfer reactions can be classified into two groups, namely the inner- sphere electron transfer and the outer- sphere electron transfer. Inner- sphere electron transfer reactions are reactions between two redox partners which transfer the electron via a covalent linkage. Typical inner- sphere ET- reactions occur in transition metal complexes. The pioneer in the field of inner- sphere ET-reactions is Henry Taube, who was awarded to the Nobel Prize in Chemistry in 1983.

In contrast to the inner- sphere mechanism is the outer- sphere electron transfer. In this type of reactions the redox partners are not connected and the electron is moving through space from one partner to the other. The pioneer of the theory to describe the outer-sphere electron transfer mechanism is the Chemistry Nobel Prize winner in 1992, Rudolph Arthur Marcus. The investigation of outer- sphere electron transfer reactions and the applicability of the „Marcus Theory“ is the main topic of this PhD thesis.

The chapter was written under guidance of the following References: [11], [43–49] ,[62]

2.2 Kinetics of the electron transfer mechanism

The outer- sphere electron transfer mechanism consists of three successive steps as pictured in the following reaction scheme.

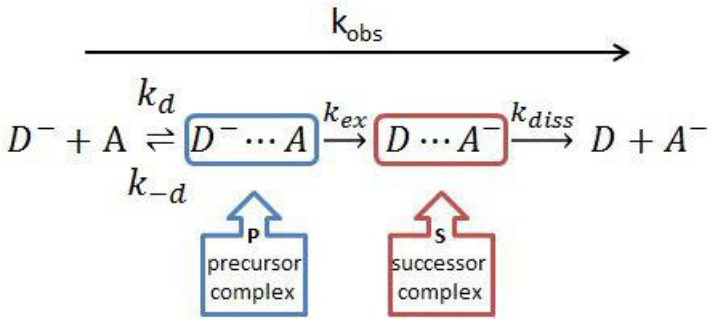

Figure 2.1: Reaction scheme of the outer- sphere electron transfer mechanism.

1. Formation of the precursor complex
2. Electron transfer from donor, D to acceptor, A
3. Dissociation of the successor complex

2.2.1 Formation of the precursor complex

$$D^- + \mathrm{A} \underset{k_{-diff}}{\overset{k_{diff}}{\rightleftharpoons}} D^- \cdots A$$

Figure 2.2: Association

In the first step the donor (D) and the acceptor (A) molecules diffuse together and form the precursor complex ($D^{-}\cdots A$). This reaction has an equilibrium constant for association, $K_A = k_{diff}/k_{-diff}$. The Association constant K_A is given by:

$$K_A = K_0 e^{\frac{-w(d)}{RT}} \qquad (2.1)$$

w(d) is the electrostatic energy as a function of the intermolecular distance, dielectric constant ε_S and charges.

Two models to describe K_0 are known. In (2.2) the hard sphere model from Eigen-Fuoss is shown.

$$K_0 = \frac{4}{3}\pi N_A d^3 \tag{2.2}$$

Another description of the association constant is given by Sutin using a reaction zone model:

$$K_0 = 4\pi N_A d^2 \delta r \tag{2.3}$$

δr…reaction zone (≈ r/3 ≈ 0,8Å)

d…reaction distance

N_A…Avogadro constant

2.2.2 The overall rate constant

The kinetic equations for the reaction in Figure 2.1 lead to the following expression for the overall rate constant k_{obs},

$$k_{obs} = \frac{k_{ex} k_{diff}}{k_{-diff} + k_{ex}} \tag{2.4}$$

assuming that no back electron transfer occurs and that the dissociation of the successor complex to the products is negligible.

$$K_A * k_{ex} = k_{et} \tag{2.5}$$

Transformation of equation (2.4), bearing in mind that $K_A = k_{diff}/k_{-diff}$ and insertion of $K_A k_{ex}$ as k_{et} leads to the common form of k_{obs}.

$$\frac{1}{k_{obs}} = \frac{1}{k_{et}} + \frac{1}{k_{diff}} \tag{2.6}$$

2.2.3 Self- exchange electron transfer

$$A^- + A \underset{k_{-diff}}{\overset{k_{diff}}{\rightleftharpoons}} A^- \cdots A \underset{k_{-ex}}{\overset{k_{ex}}{\rightleftharpoons}} A \cdots A^- \xrightarrow{k_{diss}} A + A^-$$

Figure 2.3: Reaction scheme of self- exchange electron transfer.

The simplest form of electron transfer is the reaction between two molecules of same kind. The only difference between the reactants is an electron that is exchanged during the reaction. The back electron transfer from successor to precursor complex can no longer be excluded and the expression for the overall rate constant k_{obs} changes to equation (2.7).

$$\frac{1}{k_{obs}} = \frac{1}{k_{diff}} + \frac{1}{K_A k_{ex}}\left(1 + \frac{k_{-ex}}{k_{diss}}\right) \tag{2.7}$$

Because the two reaction partners are identical it can be concluded that the dissociation of the successor complex and the back diffusion is the same and therefore $k_{diss}=k_{-d}$ must be

valid. This is also valid for the electron transfer and the back electron transfer $k_{ex}=k_{-ex}$. The additional insertion of k_{et} as $K_A k_{ex}$ leads to the equation:

$$\frac{1}{k_{obs}} = \frac{1}{k_{et}} + \frac{2}{k_{diff}} \tag{2.8}$$

2.2.4 Diffusion

The rate constant for diffusion k_{diff}, as described by Smoluchowski using a model of the Brownian motion, includes the radii of the acceptor and donor molecules r_A and r_D and the diffusion coefficients D_A and D_D.

$$k_d = 4\pi N_A (D_A + D_D)(r_A + r_D) \tag{2.9}$$

The diffusion constant is defined in the Stokes-Einstein equation:

$$D_i = \frac{k_B T}{6\pi r_i \eta} \tag{2.10}$$

k_B…Boltzmann constant

r_i…Radius of the molecule i

η…Viscosity of the solvent

If the radii of the redox couple have the same size (r_A = r_D), wich is often a practical assumption for self- exchange reactions, the expression of k_{diff} simplifies by insertion of the Stokes-Einstein relation to:

$$k_{diff} = \frac{8RT}{3\eta} \quad \textbf{(2.11)}$$

2.3 The Marcus Theory

$$D^- \cdots A \xrightarrow{k_{ex}} D \cdots A^-$$

Figure 2.4: Electron transfer

This step in the electron transfer mechanism was described by R.A. Marcus via the Marcus Theory. He described the electron transfer using the Transition State Theory (TST) and the Franck- Condon Principle. The reaction from the precursor complex to the successor complex appears via an activated transition state. The rates obey the Arrhenius and Eyring laws, but Marcus introduced the free energy ΔG* into the TST and this leads to an expression of the rate constant k_{ex} like in equation (2.12).

$$k_{ex} = Ze^{\left[\frac{-\Delta G^*}{k_B T}\right]} \quad \textbf{(2.12)}$$

The insertion of equation (2.5) for k_{ex} leads to the expression below

$$k_{et} = K_A Ze^{\left[\frac{-\Delta G^*}{k_B T}\right]} \quad \textbf{(2.13)}$$

Z…pre-exponential factor (=$\kappa_{el}\nu_n$)

ΔG^*…Gibbs free energy of activation

k_B…Boltzmann constant

T…temperature

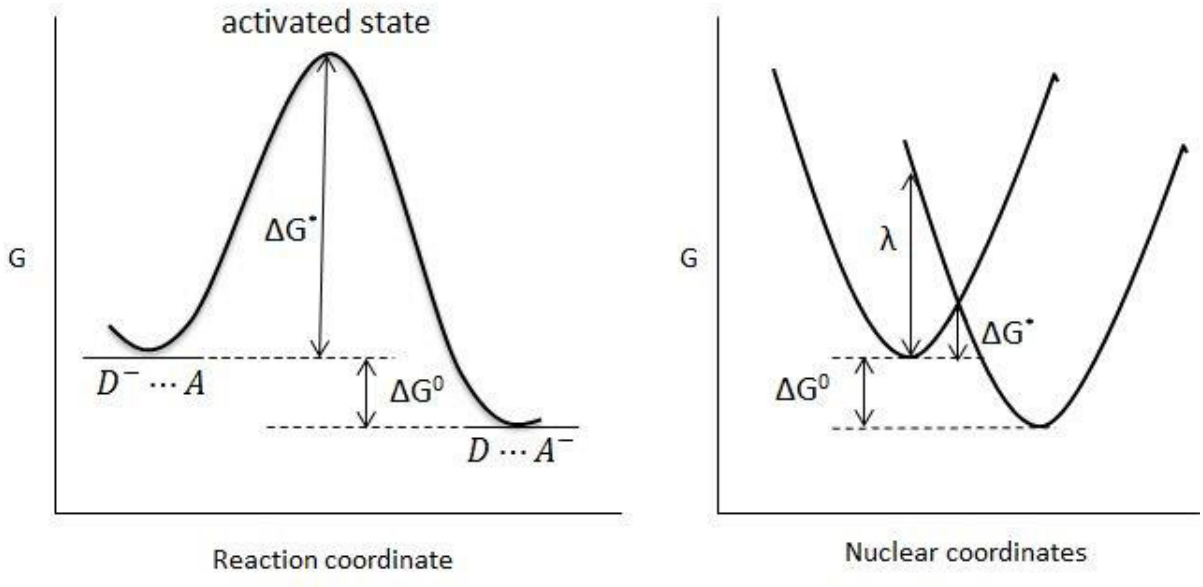

Figure 2.5: Reaction coordinate and potential energy diagram for a exergonic ET- reaction.

Figure 2.5 presents the electron transfer reaction in form of a reaction coordinate and in form of an energy diagram with two crossing parabolas. Both diagrams point out that the energy difference of precursor and successor complex denotes the standard Gibbs free energy ΔG^0. The figure presents an exergonic case with positive values of ΔG^0. Two other cases are possible. $\Delta G^0 < 0$ for the endergonic ET- reaction and $\Delta G^0 = 0$ such as for self-exchange reactions (Figure 2.8). ΔG^* is the energy needed to reach the transition state where the electron is transferred. It is the difference between the energy of the precursor complex and the maximum of the curve in the reaction coordinate diagram and the crossing point of the parabolas in the energy diagram.

The Gibbs energy of activation is given in the Marcus equation:

$$\Delta G^* = W + \frac{\lambda}{4}\left[1 + \frac{\Delta G^0}{\lambda}\right]^2 - V_{RP} \quad \textbf{(2.14)}$$

and simplifies, in the case of self- exchange reactions where either acceptor or donor has zero charge, to:

$$\Delta G^* = \frac{\lambda}{4} - V_{RP} \quad \textbf{(2.15)}$$

ΔG^0…standard Gibbs free reaction energy

λ…reorganization energy

V_{RP}…resonance splitting energy

W…describes the necessary electrostatic work to bring the reactants together.

The electrostatic work term is described by the Coulomb law.

$$W = \frac{z_A z_D e_0^2 N_A}{4\pi\varepsilon_0\varepsilon_s d} \quad \textbf{(2.16)}$$

z_A, z_D...point charge of acceptor and donor

ε_0…permittivity of vacuum

ε_s… static dielectric constant

d…distance between acceptor and donor

2.3.1 Inverted region

The equation (2.14) show the dependence of ΔG^* on ΔG^0 in a second order polynomial function. The dependence is plotted in Figure 2.6 and shows that the relation of $-\Delta G^0$ on ΔG^* (solid line) and of $-\Delta G^0$ on $\ln(k_{et})$ (dotted line) end up in a parabola.

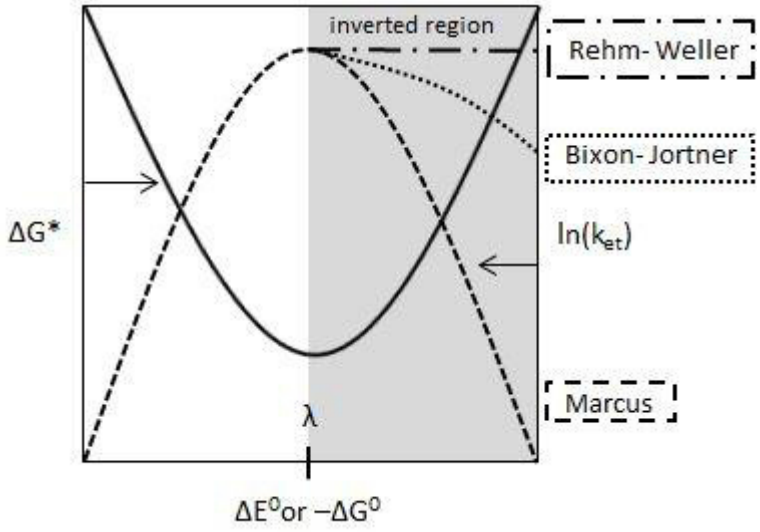

Figure 2.6: Marcus inverted region

The left side of the picture demonstrates that by increasing the driving force, the reaction goes faster ($-\Delta G^0<\lambda$) and reaches a maximum of the rate at ($-\Delta G^0=\lambda$). The right side of the picture tells us that by further increasing the driving force ($-\Delta G^0>\lambda$), the reaction gets slower. Marcus called this side of the parabola the “inverted region”. It was not easy to confirm the inverted region experimentally because by increasing the driving force the electron transfer gets faster. In many investigated redox systems the observed rates were diffusion controlled before the inverted region could be reached. Other models for the inverted region are known and plotted in the figure above. The rates in the Rehm-Weller-Model [58] remain constant after the maximum and in the Bixon- Jortner Model [4], they decrease, but not as strongly as Marcus predicts. The latter has proved for intramolecular electron transfer experiments [35].

2.3.2 Reorganization energy

A new component in ΔG* is the reorganization energy λ which can be split into a solvational part, the outer reorganization energy λ_o (depends on the solvent properties) and a vibrational part λ_i, the inner reorganization energy (depends on the geometry of the complex at the transition state).

$$\lambda = \lambda_o + \lambda_i \tag{2.17}$$

Marcus described the reorganization energy as follows. The reactants are surrounded by solvent molecules certain configuration. A reorganization of solvent molecules and reactants is necessary before the electron transfer takes place. After the electron transfer a relaxation process succeeds. The necessary energy for the rearrangement is given by λ.

2.3.2.1 Inner sphere reorganization energy

The energy term which depends on reorganization of the reactants in form of changes in bond lengths or angels contributes to the reorganization energy λ in form of the inner sphere reorganization energy λ_i. Marcus defined the inner sphere reorganization energy as follows

$$\lambda_i^{\infty} = \sum_j \frac{f_j^r f_j^p}{f_j^r + f_j^p} \left(\Delta q_j\right)^2 \tag{2.18}$$

Δq_j...change in length of bond j

f_j…force constant of bond j in reactants r and products p

Another common method to calculate the λ_i is using the quantum chemical Nelsen method [54] with the appropriate equation (2.19) below. Knowledge of the change in bond length and force constant is not necessary because the Nelsen method is based on quantum chemical calculations.

$$\lambda_i^{\infty} = [E(A,D) + E(D,A)] - [E(A,A) + E(D,D)] \quad \textbf{(2.19)}$$

E(A,D)and E(D,A)…energy in the most stable configuration of the products

E(A,A)and E(D,D)…energy in the most stable configuration of the reactants

According to Holstein [29] the temperature dependence of λ_i is calculated via equation (2.20) with the mean vibrational frequency $\bar{\nu}$ ($5 \cdot 10^{13} s^{-1}$ for organic redox couples) , the Boltzmann constant k_B and the Planck constant h

$$\lambda_i(T) = \lambda_i^{\infty} \left[\frac{4k_B T}{h\bar{\nu}} \tanh \frac{h\bar{\nu}}{4k_B T} \right] \quad \textbf{(2.20)}$$

2.3.2.2 Outer sphere reorganization energy

This energy part describes the necessary energy to rearrange the solvent molecules of certain polarities from the arrangement around the precursor complex to the arrangement around the activated complex. Marcus expressed λ_o on the basis of a two sphere model of the reactants[48].

$$\lambda_o = \frac{\Delta e_0^2 N_A}{4\pi\varepsilon_0} g(r,d) * \gamma \quad \textbf{(2.21)}$$

$r_{A,}$ r_D…radius of donor and acceptor

Δe_0…charge transferred from donor to acceptor

ε_0…permittivity of vacuum

d…reaction distance

γ…Pekar factor

A new parameter is the Pekar factor which is defined in equation (2.22) as a function of the dielectric properties of the solvent.

$$\gamma = \frac{1}{\varepsilon_\infty} - \frac{1}{\varepsilon_S} \quad \textbf{(2.22)}$$

ε_∞…optical dielectric constant (also referred to as ε_{opt}).

ε_S…static dielectric constant

The approximation $\varepsilon_\infty \approx n_D^2$ is often used for the optical dielectric constant.

The other new parameter in the expression of the outer sphere reorganization energy is the term g(r,d) which depends on the geometry of the activated complex and is defined as follows:

$$g(r,d) = \frac{1}{2r_A} + \frac{1}{2r_D} - \frac{1}{d} \tag{2.23}$$

Equation (2.23) is only valid for d > r_A , r_D and simplifies to (2.24) in the case of a self-exchange redox reaction, because it is usually valid to equate the dimensions of the reaction partners (r_A=r_D). Often used is the assumption of the closest contact, so that d = r_A+r_D and in the case of self- exchange reactions d = 2r.

$$g(r,d) = \frac{1}{r} - \frac{1}{d} \tag{2.24}$$

For organic reactants because of the non- spherical geometry the two sphere model is too simple. Therefore, a two ellipsoid model [19] must be used. As shown in Figure 2.7 the ellipsoids have three semiaxes a>b>c and a mean radius $\bar{r}$ which is defined as

$$r = \bar{r} \approx \frac{(a^2 - c^2)^{1/2}}{F(\varphi, \alpha)} \tag{2.25}$$

$F(\varphi, \alpha)$ are elliptical integrals of the first kind with $\varphi = \arcsin[\frac{(a^2-c^2)^{\frac{1}{2}}}{a}]$ and $\alpha = [\frac{a^2-b^2}{a^2-c^2}]^{1/2}$. A good approximation for the radius is r ≈ (a+b+c)/3. The geometric term g(r,d) becomes the expression (2.26) as described by Kharkats [36, 37], when the ellipsoids are lying upon each other or are slightly shifted.

$$g(r,d) = \frac{1}{r} - \frac{1}{d}\left[1 + \frac{2c^2 - a^2 - b^2}{3d^2} + \frac{abc}{d^3} + \frac{4(8c^4 + 3(a^4 + b^4) - 8c^2(a^2 + b^2) + 2a^2b^2)}{15d^4}\right] \quad \textbf{(2.26)}$$

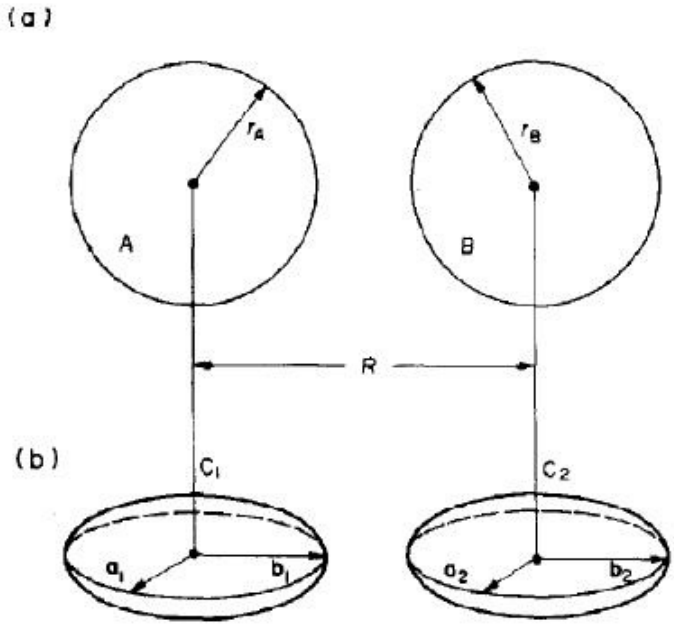

Figure 2.7: (a) Model of two conducting spheres, (b) model of two conducting ellipsoids, R is the separation distance(r).©Ref.[19]

2.3.3 Marcus Cross Relation

One of the most tested aspects of the Marcus Theory is the cross relation. The assumption that the reorganization of the redox partners appears independently leads to the approximation that rate constants of cross reactions k_{12} (2.27) can be expressed via self-exchange rate constants of the acceptor A with k_{11} (2.28) and the donor D with k_{22} (2.29).

$$A + D \overset{k_{12}}{\rightleftharpoons} A^- + D^+ \tag{2.27}$$

$$A + A^- \overset{k_{11}}{\rightleftharpoons} A^- + A \tag{2.28}$$

$$D + D^+ \overset{k_{22}}{\rightleftharpoons} D^+ + D \tag{2.29}$$

From equation (2.14),(2.12),(2.18)and (2.21) follows the expression for the reorganization energy λ (2.30) and the rate constant (2.31) of the cross reaction with the work term W (see equation (2.16)).

$$\lambda_{12} = \frac{1}{2}(\lambda_{11} + \lambda_{12}) \tag{2.30}$$

$$k_{12} = \sqrt{k_{11} k_{22} K_{12} f_{12}} * W_{12} \tag{2.31}$$

2.3.4 Resonance splitting energy

Because of the quantum mechanical non- crossing rule the wave functions must split at the intersection point. The electronic coupling of the precursor and the successor complex is the gap between the dotted lines in Figure 2.8 and is usually denoted by V_{RP}.

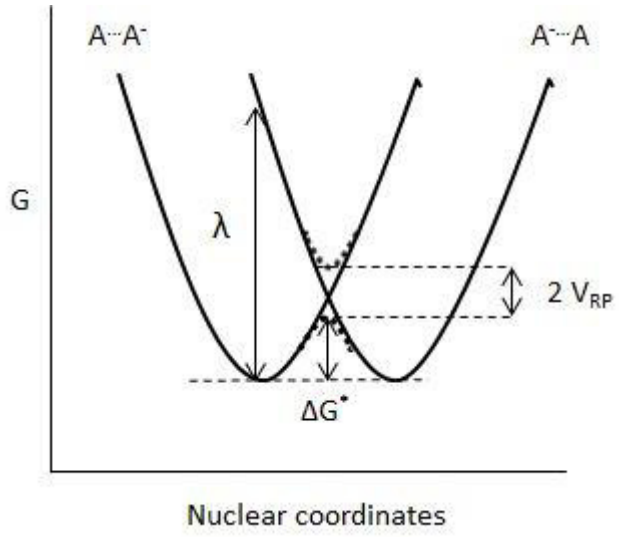

Figure 2.8: Energy diagram of a self-exchange ET.

How strong the coupling is depends on the nature of the complex at the transition state. The probability of the electron jumping from one potential curve to the other is dependent on the splitting and is fixed in the pre-exponential factor Z in (2.12). The pre- exponential factor is a function of the separation distance between donor and acceptor.

$$Z(d) = \nu_n \kappa_{el}(d) \tag{2.32}$$

ν_n…collision frequency

$\kappa_{el}(d)$…transmission coefficient or probability of electron jump

$$\kappa_{el}(d) = \kappa_0 e^{-\beta d} \tag{2.33}$$

The magnitude of the coupling element decides whether there is either a diabatic or an adiabatic reaction behavior. For diabatic reactions is the coupling weak and V_{RP} is small in comparison to the reorganization energy λ (see Figure 2.9 a). The top of the electron barrier is cusp and the electron transfer appears near the intersection with a certain

probability (κ_{el} << 1). The electron moves too fast through the transition state to form the product side. Only a few jumps are successful.

Adiabatic reactions have a strong coupling and therefore a higher V_{RP} (Figure 2.9 b). The energy barrier decreases with stronger couplings and leads continuously from reactants to products (κ_{el} ≈ 1). The top of the energy barrier is broadened and therefore the system has time enough to form the product side. Each jump is successful.

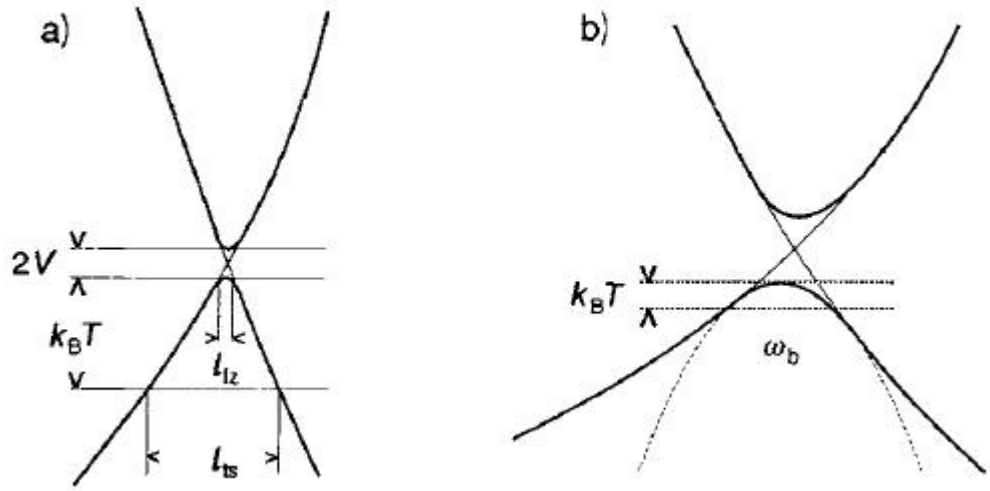

Figure 2.9: a) diabatic reaction, b) adiabatic reaction. ©[27]

2.4 Solvent dynamics

The surrounding solvent molecules can influence the motion along the reaction coordinate and the barrier crossing for the electron. The rate in equation (2.12) is given only by static solvent properties (polarity, refractive index). Under certain circumstances this is no longer enough and needs a correction of the rate constant. Kramer [41] was the first who realized a solvent dynamic effect or solvent friction. The theory of solvent dynamics on electron transfer reactions appears much later by Zusman [74–76].

Figure (2.10) a) shows the barrier crossing with weak solvent dynamic effects. Figure (2.10) b) shows the adiabatic reaction with solvent dynamic effect, where the system undergoes

several changes in direction within the transition state region before settling down on the product side.

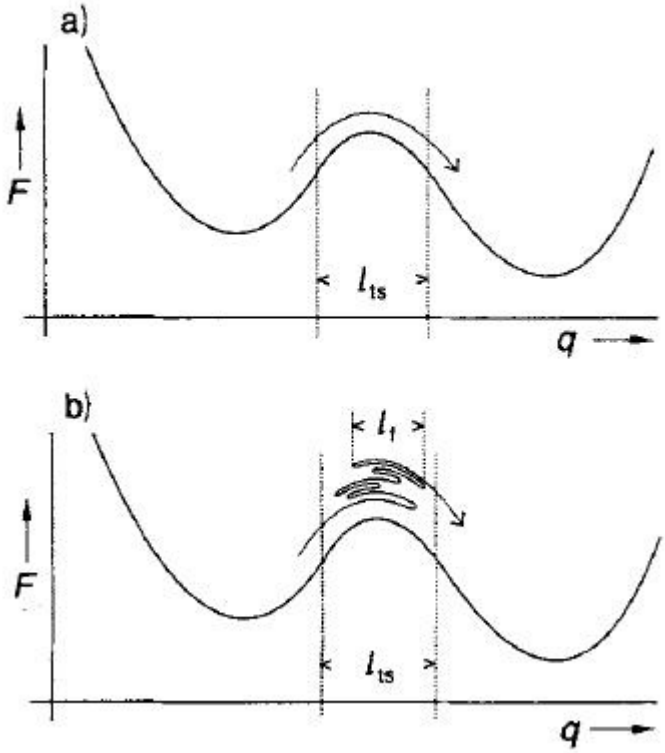

Figure 2.10: Motions along the adiabatic reaction coordinate a) without solvent dynamic effects b) with solvent dynamic effects.©[27]

As mentioned before, the barrier crossing is controlled by the pre- exponential factor Z as a function of the collision frequency ν_n and the transmission coefficient κ_{el} (2.32). For adiabatic reactions with κ_{el} of unity, the barrier crossing is only influenced by the collision frequency ν_n. The expression for the total frequency ν_n from Transition State Theory is a combination of a reactant part $\nu_i^2 \lambda_i$ and a solvent part $\nu_o^2 \lambda_o$.

$$\nu_n = \left(\frac{\nu_i^2 \lambda_i + \nu_o^2 \lambda_o}{\lambda}\right)^{1/2} \quad \textbf{(2.34)}$$

The longitudinal relaxation time τ_L must be included to take the solvent dynamics into account. It is composed of the dielectric parameters of the solvent and the Debye relaxation time τ_D.

$$\tau_L = \frac{\varepsilon_\infty}{\varepsilon_S} \tau_D \quad \textbf{(2.35)}$$

New quantities in the Debye relaxation time are the molar volume V_M and the solvent viscosity η.

$$\tau_D = \frac{3 V_M \eta}{RT} \quad \textbf{(2.36)}$$

Under assumption that the inner sphere contributions are negligible small, the ν_n can be expressed as follows:

$$\nu_n = \frac{1}{\tau_L}\left(\frac{\lambda_o}{4\pi RT}\right)^{1/2} \quad \textbf{(2.37)}$$

And in the case of a solvent controlled adiabatic electron transfer the rate constant obeys the following expression.

$$k_{ex,adiabat} = \frac{1}{\tau_L}\left(\frac{\lambda_o}{16\pi RT}\right)^{1/2} e^{\left[\frac{-\lambda}{4RT}\right]} \quad \textbf{(2.38)}$$

In comparison, the rate for diabatic electron transfer is given by

$$k_{ex,diabat} = \frac{2\pi V^2}{\hbar N_A (4\pi\lambda_o RT)^{1/2}} e^{\left(\frac{-\lambda_o}{4RT}\right)} \quad \textbf{(2.39)}$$

As suggested by Weaver[70, 71] it is possible to extract the solvent dynamic dependence from experimental obtained rates via double logarithmic plots (Weaver plots). The conversion of the equation (2.13) into an expression for the pre exponential factor gives equation (2.40). With calculated values of ΔG^* via equation (2.14) and the experimental observed rates k_{et} it is possible to calculate an experimental value for $\kappa_{el}\nu_n$.

$$\kappa_{el}\nu_n = \frac{k_{et}}{K_A} e^{\left(\frac{\Delta G^*_{calc}}{RT}\right)} \quad \textbf{(2.40)}$$

The following double logarithmic plot can be used for the diabatic case and has to produce slopes of unity.

$$\ln(\kappa_{el}\nu_n) = c + \ln\left(\gamma^{-\frac{1}{2}}\right) \quad \textbf{(2.41)}$$

For the adiabatic case the following plot gives a slope of unity.

$$\ln(\kappa_{el}\nu_n) = d + \ln\left(\gamma^{\frac{1}{2}}\tau_L^{-1}\right) \quad \textbf{(2.42)}$$

After determining the type of the electron transfer (diabatic or adiabatic) the linear functions of the Pekar factor can be used to calculate an experimental value of g(r,d).

$$diabatic: ln\left(k_{et}\gamma^{1/2}\right) = const - \left[\frac{e_0^2 g(r,d)}{16\pi\varepsilon_0 kT}\right]\gamma \quad \textbf{(2.43)}$$

$$adiabatic: ln\left(k_{et}\tau_L\gamma^{-1/2}\right) = const - \left[\frac{e_0^2 g(r,d)}{16\pi\varepsilon_0 kT}\right]\gamma \quad \textbf{(2.44)}$$

The intercepts of both straight lines are independent from the Pekar factor and show a g(r,d)/T dependent slope. Experimental values for g(r,d) can therefore be calculated from the obtained slope.

$$g(r,d) = slope * \left(\frac{-16\pi\varepsilon_0 kT}{e_0^2}\right) \quad \textbf{(2.45)}$$

2.5 Pressure dependence of the electron transfer Reaction

From the Marcus theory described before it is apparent that the rate constant has a temperature dependence under ambient pressure. But, there is also a dependency of the rate constant on the pressure. By variation of pressure the solvent properties changes like by variation of temperature. But pressure experiments have an advantage. Many of the

investigated radicals are not stable at higher temperatures what restricted the use of such experiments. Solvent properties like viscosity change in the other direction like at increasing temperatures. Therefore the investigation on pressure dependent rate constants is a very good tool to make conclusions about solvent effects.

Detailed general literature about high pressure chemistry are published by van Eldik, Le Noble and Asano [2, 10, 12, 13]. The high pressure application of the Marcus Theory has been investigated by Swaddle[65, 66].

2.5.1 Activation volume

The differentiation of the Arrhenius equation with respect to the pressure p gives the expression for the activation volume.

$$\Delta^{\ddagger}V = -RT\left(\frac{\partial lnk_{ex}}{\partial p}\right)_{T} \qquad \textbf{(2.46)}$$

Figure 2.11 presented the volume version of an reaction diagram with the volumes of the reactants (V_A+V_D^-) and products (V_A^-+V_D) and volume of the transition state $^{\ddagger}V$. The volume difference of products and reactants $\Delta_r V$ is in the case of self- exchange reactions zero. This is the case for all investigated reactions in this thesis.

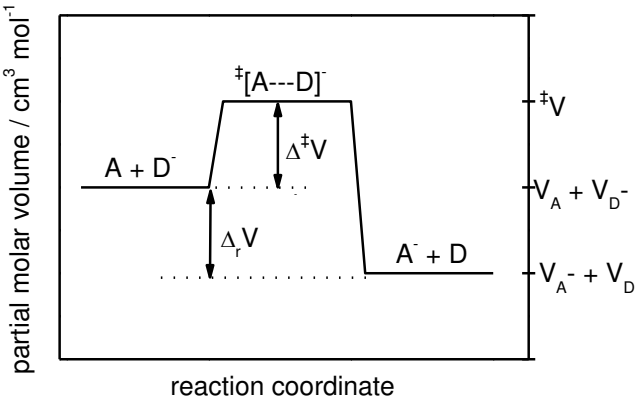

Figure 2.11: Volume diagram of an electron transfer reaction.©[56]

According to Swaddle the activation volume of the transition state can be written as the sum of different contributing volumes.

$$\Delta^{\ddagger}V = \Delta^{\ddagger}V_i + \Delta^{\ddagger}V_o + \Delta^{\ddagger}V_C + \Delta^{\ddagger}V_{DH} + \Delta^{\ddagger}V_{SD} \qquad (2.47)$$

$\Delta^{\ddagger}V_i$….inner sphere reorganizational contributions (in the most cases 0.6 cm^3mol^{-1}[63])

$\Delta^{\ddagger}V_o$….outer sphere reorganizational contributions

$\Delta^{\ddagger}V_C$….contribution from Coulombic work of the precursor complex

$\Delta^{\ddagger}V_{DH}$….contributions from Debye- Hückel type ion effects

$\Delta^{\ddagger}V_{SD}$…solvent dynamic contributions

Contributions from Coulombic work can be neglected in the case of the investigated self-exchange systems with one charged and one neutral redox partner. For the same reason (one neutral redox partner), Contributions from Debye- Hückel effects can also be neglected for self- exchange reactions in organic solvents so that equation (2.47) simplifies

to (2.48). $\Delta^{\ddagger}V_i$ is negligible because its contributions are around 0.6 cm^3mol^{-1}[63], wich is within region of experimental error.

$$\Delta^{\ddagger}V = \Delta^{\ddagger}V_o + \Delta^{\ddagger}V_{SD} \tag{2.48}$$

2.5.2 Volume from outer sphere contributions

Differentiation of the equation (2.21) with respect to the pressure p gives the following expression for the activation volume of the outer sphere contribution.

$$\Delta^{\ddagger}V_o = \frac{1}{4}\left(\frac{\partial\lambda_o}{\partial p}\right) = \frac{e_0^2 N_A g(r,d)}{16\pi\varepsilon_0}\left(\frac{\partial\gamma}{\partial p}\right) \tag{2.49}$$

Here, the geometric term g(r,d) is expected to be independent of pressure, what is questionable and shall be discussed later in the experimental part. Another important point is the compressibility β of the solvent. This includes the fact that the volume of the solvent decreases as pressure increases and is given as a function of the solvent density ρ.

$$\beta = \frac{1}{\rho}\left(\frac{\partial\rho}{\partial p}\right) \tag{2.50}$$

The compressibility can be included in equation (2.49) and gives the extended version of $\Delta^{\ddagger}V_o$.

$$\Delta^{\ddagger}V_o = \frac{1}{4}\left(\frac{\partial\lambda_o}{\partial p}\right) = \frac{e_0^2 N_A}{16\pi\varepsilon_0}\left[g(r,d)\left(\frac{\partial\gamma}{\partial p}\right) - \gamma\frac{\beta}{3d}\right] \quad \textbf{(2.51)}$$

2.5.3 Volume from solvent dynamic effects

Solvent dynamics are found in the pre- exponential factor. Its pressure dependence can be expressed by equation (2.52) for the case of a diabatic electron transfer reaction.

$$\Delta^{\ddagger}V_{SD} = RT\left[\frac{\partial}{\partial p}\left(ln\frac{2\pi V^2}{\hbar N_A(4\pi\lambda_o RT)^{1/2}}\right)\right] = -\frac{RT}{2}\left(\frac{\partial ln\gamma}{\partial p}\right) \quad \textbf{(2.52)}$$

In the case of an adiabatic electron transfer reaction the expression for the solvent dynamic part is given by a τ_L dependence in equation (2.53).

$$\Delta^{\ddagger}V_{SD} = RT\left[\frac{\partial}{\partial p}\left(ln\frac{1}{\tau_L}\left(\frac{\lambda_o}{4\pi RT}\right)^{1/2}\right)\right] = RT\left[\frac{1}{2}\left(\frac{\partial ln\gamma}{\partial p}\right) - \left(\frac{\partial ln\tau_L}{\partial p}\right)\right] \quad \textbf{(2.53)}$$

2.6 Electron Spin Resonance

Electron Spin Resonance (ESR) is a method to investigate paramagnetic substances like radicals. The major advantage of ESR spectroscopy is the high sensitivity for the investigated substances. The magnetic characteristic of one (or more) unpaired electron and the magnetic interaction between the electron and the magnetic nuclei gives information about the molecule. This chapter is a short introduction into the basics of the ESR and was written under guidance of the following references: [5], [33], [60],.[72]

2.6.1 Electron Spin in a magnetic field

Electrons in atoms and molecules have an orbital angular momentum and an intrinsic angular momentum, the spin. In organic molecules the orbital angular momentum is negligible and only the spin has to be considered. The angular momentum can be defined by the length and the direction of the vector. The magnetic moment μ is proportional to the electron spin S. This means that both are vectors and parallel to each other (see equation (2.54).The value g is the Lande factor or the g factor (g = 2.002319 for the free electron) and μ_B is the Bohr Magneton (9,27 $10^{-24.}$ JT^{-1}).

Figure 2.12: Spin S and magnetic moment μ of the electron.

$$\overrightarrow{\mu} = -g\,\mu_B\,\overrightarrow{S} \tag{2.54}$$

Radicals in solution can be visualized like a statistical arrangement of many magnetic moments with an Energy E_0. By introducing the sample into a homogeneous magnetic field, B_0 will orient the magnetic moments parallel or antiparallel to the magnetic field B_0. The orientation of the spin to the magnetic field is described by the magnetic quantum numbers m_S = +1/2 (α state) and m_S = -1/2 (β state). At zero magnetic field B_0=0 the α and β spin state differ in the orientation but have the same energy E_0. The interplay of the magnetic field with the magnetic moments results in the splitting of the Energy E_0 into two energy levels with the Energy $E = m_S g \mu_B B_0$ and is the so called "Zeeman-effect".

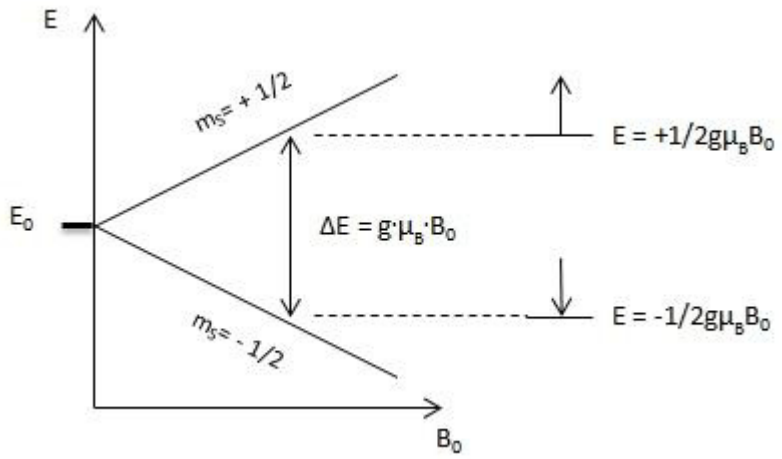

Figure 2.13: Energy levels of an electron placed in a magnetic field.

The energy difference between the two states is proportional to the magnetic field and the g factor. The low energy state (β state) can absorb a quantum of electromagnetic radiation energy hν to reach the higher energy state (α state). In contrast to this can the α state reach the lower β state by emitting the energy hν.

$$\Delta E = E_\alpha - E_\beta = h\nu = g\mu_B B_0 \tag{2.55}$$

Equation (2.55) results with a standard radiation frequency of ν=9.5 GHz, which is used in many ESR spectrometers, and a g factor of 2.0023, in magnetic field intensity of 0.35 T. This is within the microwave X-band region (8-12 GHz) and spectrometers that operate in this frequency region are called X-band spectrometers.

The electron spins of an ensemble have either α or β configuration. In absence of a magnetic field B_0=0 the distribution is equivalent but in presence of a magnetic field $B_0 \neq 0$ and when the spin ensemble can interact with the environment (the lattice), the distribution changes to have an excess of the lower energy level (β state). The distribution depends on the temperature of the lattice and is given by the Boltzmann distribution law:

$$\frac{N_\alpha}{N_\beta} = e^{\frac{-g\mu_B B_0}{k_B T}} \tag{2.56}$$

The quantities N_α and N_β are the spin populations in the higher and the lower energy states, k_B is the Boltzmann constant and T the temperature.

In contrast, when the spin ensemble cannot interact with the lattice (isolated spin), the continuously acting microwave (CW-ESR) would equalize the level population and the ESR spectra would disappear after a short time. Because the transition from β to α state and vice versa appears to the same extent and the absorption and the emission compensate each other (net effect is zero).

The spin lattice interaction restores the thermal equilibrium which leads to an excess in the low energy spin population. This means that the absorption is dominant in comparison to the emission and the recording of the absorption spectra is possible. Therefore it is a competition between the microwave field and the spin lattice interaction. But this implies that the ESR signal saturates when the microwave field gets too strong.

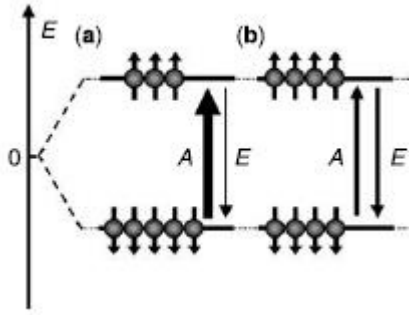

Figure 2.14: Population of the energy levels. (a) dominant population in the lower energy level leads to an absorption spectrum, (b) equal distribution of the spins in both energy levels does not lead to a ESR-spectra.©[5]

2.6.2 Magnetic Resonance

The observation of an absorption spectrum is possible, if equation (2.55) is fulfilled. To perform an ESR experiment the radical solution is placed in a cavity and irradiated with micro wave radiation of constant frequency ν while the magnetic field intensity is varied. The absorption takes place when the magnetic field reaches the intensity B_0 where the resonance condition is fulfilled. The line shape of the absorption line is determined by dynamical processes.

2.6.3 Hyperfine structure

From the previously discussed aspects we would expect one line in the ESR spectra caused by the transition of the electron from the β to α energy level. But in most of the cases, the ESR spectra contain more than one line. The reason for this is the interaction of the free electron with the magnetic moment of the atomic nucleus μ_N. Magnetic nuclei have similarly to the electron spin (S) a nuclear spin (I) which is oriented in an external magnetic field parallel or antiparallel to the field. Two mechanism of coupling between electron and nucleus are possible: the dipole-dipole interaction, which is anisotropic and can be

neglected for ESR-measurements in solution and a Fermi contact interaction. The latter interaction is isotropic and plays a major role in interpreting an ESR spectrum. This example is the simplest form of hyper fine splitting with one proton and its nuclear spin (I=1/2). Here, the electron gets the information about the orientation of the nuclear spin which results in a splitting of each Zeeman energy levels in two new energy levels. The four new energy levels allow two transitions (two lines in the ESR- spectrum) for the electron. The actual number and intensity of ESR lines depends on the number of equivalent nuclei and their nuclear spin I. The number of lines can be predicted via equation (2.57) where $\prod_I$ indicates the product over all different sets of equivalent nuclei (i). Here, n_i is the number of nucleus in set i and I_i is the nuclear spin of nucleus i.

$$N = \prod_i (2n_i I_i + 1) \tag{2.57}$$

2.6.4 g- value

As mentioned before in chapter 2.6.1 the electron angular momentum has two contributions, one from the orbital motion and one from the electron spin. The orbital and the spin angular momentum are coupled. This spin-orbit coupling results in a deviation of the g factor from that of the free electron. Because of the negligibly small contributions from the orbital angular momentum in organic free radicals is the deviation from the g factor of the free electron very small. Nevertheless, such small deviation can be useful for characterizing the radical species. The spin-orbit coupling is anisotropic which means that the g value becomes dependent on the direction of the magnetic field with respect to the molecular axis. But in solution, because of the free molecular motion, the anisotropy is averaged out and mean value of $g = g_{iso}$ is measured.

2.6.5 Magnetization

An electron spin ensemble consists of many individual electron spins, interacting both with the lattice and with each other. The spin properties can be described by the magnetization vector M as a sum of magnetic moments of each electron spin. Is such a system in a magnetic field B_0 and in thermal equilibrium with the lattice, the magnetization is oriented along the z axis (along the magnetic field direction). The magnetization components perpendicular to z are zero.

$$M_z = \sum \mu_{zi} = M_0$$

$$M_x = \sum \mu_{xi} = 0 \qquad \textbf{(2.58)}$$

$$M_y = \sum \mu_{yi} = 0$$

M_0 is the magnetization in the thermal equilibrium and μ_{zi}, μ_{xi} and μ_{yi} are the magnetic moments of the individual spins. The magnetization vector rotates around the z axis and the so-called Larmor precession can be described by the time evolution of M in a magnetic field B by

$$\frac{dM}{dt} = M \times g\mu_B B \qquad \textbf{(2.59)}$$

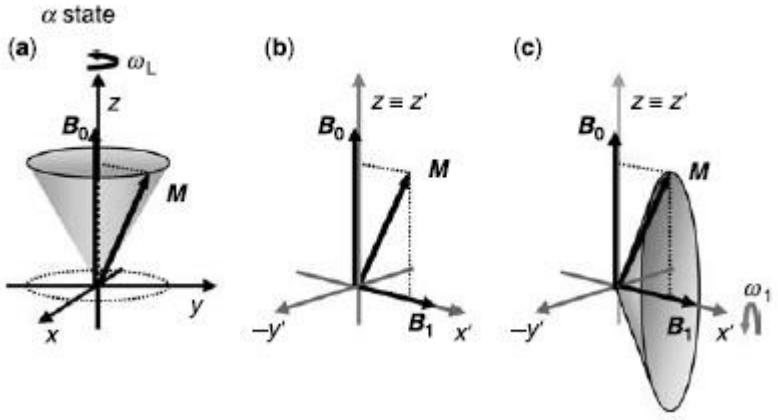

Figure 2.15: (a) rotation of M around z axis by placing in magnetic field B_0, (b) in a reference frame is the rotation of M about the z axis stationary, (c) a second magnetic field B_1 induces a rotation of M around the x-axis. ©Ref.[5]

The transition between the two Zeeman levels can appear by an electromagnetic field B_1 with frequency v. This additional field oscillates at microwave frequency along the x axis. This introduces an additionally rotation of the magnetization vector around the x axis. The use of a rotating reference frame simplifies the description of the motion of M. Figure 2.15 (a) presents the rotation of M along B_0. This motion observed in a rotating frame, where x' and y' rotating around z at angular frequency ω_0 is presented in Figure 2.15 (b). The precession of M around x' at an angular frequency ω_1, induced by the second magnetic field B_1 is presented in Figure 2.15 (c). Whereas the magnetic field $\omega_1 << \omega_0$ this in turn means that $B_1 << B_0$.The motion of M can be described by

$$\frac{dM}{dt} = M \times g\mu_B B_{eff} \tag{2.60}$$

$$\hat{B}_{eff} = (B_0 - \omega\hbar/g\mu_B)\boldsymbol{k} + B_1\boldsymbol{i} \tag{2.61}$$

Here, ω is the rotation angular frequency of the magnetization vector M in the rotating frame. **k** and **i** are the unit vectors directed along the z and x' axis.

2.6.6 Relaxation

Spin-lattice interactions and interactions between the spins each other are relaxation processes with are considered in the famous Bloch equations:

$$\frac{dM_z}{dt} = -M_y\omega_1 - \frac{(M_z - M_0)}{T_1}$$

$$\frac{dM_x}{dt} = M_y(\omega - \omega_0) - \frac{M_x}{T_2} \qquad \textbf{(2.62)}$$

$$\frac{dM_y}{dt} = -M_z\omega_1 - M_x(\omega - \omega_0)$$

New quantities here are the relaxation times T_1 and T_2. The longitudinal relaxation time T_1 relates to the energy transfer process between spin and lattice. The transverse relaxation time T_2 relates to the energy transfer between the spins. The ESR absorption signal is proportional to the magnetization M_y (magnetization perpendicular to B_1) which is obtained by solving the differential equations (2.62) under steady-state conditions. If the micro wave field is continuous and small ($B_1 << B_0$) which is usually the case, the following expression is valid:

$$M_y = \left(\frac{M_0}{B_0}\right)\frac{B_1 T_2}{[1 + (\omega - \omega_0)^2 T_2^2]} \qquad \textbf{(2.63)}$$

The equation above is a function of ω (Lorentzian function) and the line width is inversely proportional to the relaxation time T_2. Indeed, the use of the second derivative of the Lorentzian function is common. In some cases, for instance when some Lorentzian lines are superimposed, is the line shape better described by a Gauss function.

2.6.7 Dynamic line shape effect

Because of the Heisenberg uncertainty principle the ESR line cannot be infinitely narrow because the lifetimes of the different states of occupation of the energy levels are finite. The lifetimes are given by different relaxation processes as mentioned before. An additional chemical reaction like an electron transfer in the case of self- exchange reaction, results in a broadening of the ESR lines. Via the extended Bloch equations it is possible to calculate rate constants by observation the broadening of the lines. In the case of a self-exchange reaction the ESR- lines of the radical [D^-] get broadened by adding neutral substance [A] by starting the electron transfer reaction. By increasing the concentration of [A] the broadening gets more distinctive because of the increasing probability of collisions. Here can be distinguished between the two limiting cases, the slow exchange limit (see Figure 2.16(b)) and the fast exchange limit where the lines collapse to one single line (see Figure 2.16 (d)).

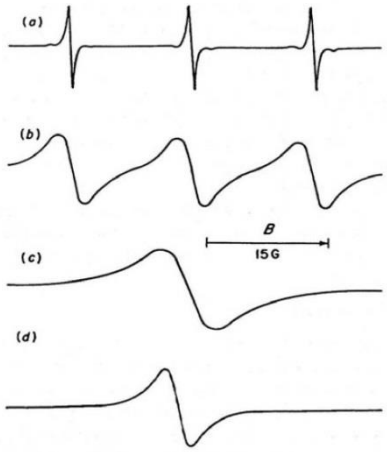

Figure 2.16: (a) no exchange (b) slow exchange, (c) intermediate exchange and (d) fast exchange. ©Ref.[72]

3. Experimental

3.1 Solvents and their properties

To make conclusions about solvent effects on the electron transfer an accurate knowledge on the solvent properties such as viscosity, density, refractive index and dielectric constant is important. Especially, it is necessary to have an idea about their dependence on pressure and temperature. Often it is a challenge to find the suitable solvent properties in the literature and also to trust in it. Some temperature dependent viscosities and densities presented here were measured during the course of this work while other solvent properties have been extracted from literature and others are simple approximations. All of the used solvent properties are listed in this chapter.

The ordered ILs are delivered in a good purity grade, but have very small amounts of impurities, which can influence their properties or initialize possible reactions with the substances added. The major impurity in the ILs is water which is decreasing the viscosity. In contrast, halide impurities like chloride, bromide and iodide increase the viscosity of the ILs. Further impurities of the educts (methylimidazolium) may influence the investigated substances. Methylimidazolium is a strong reducing agent and will, for example, reduce the neutral TCNE to the radical anion $TCNE^{\bullet-}$. This is a disturbing effect and thus methylimidazolium had to be eliminated before measurements with the redox couple [$TCNE/TCNE^{\bullet-}$] and [$DDQ/DDQ^{\bullet-}$] could be started. Therefore, to test if there are reducing impurities in the used ILs, a simple test was done. Dissolving of a small amount of DDQ in the IL clearly indicates by a red colour the presence of methylimidazolium. The colour of the ILs changes further depending on the production batch. After consultation with the company, we could relize that the colouring depends on imidazolium dimers, which do not affect the properties of the IL and the redox couple. The purification methods to remove such impurities are described in detail in the chapter 3.1.2-3.1.5 for each used IL, separately.

3.1.1 General Observations

3.1.1.1 Viscosity

The self-measured viscosities are from temperature dependent measurements with a micro-Ubbelohde viscosimeter. The solutions were kept under nitrogen during the measurement to avoid contact with air and humidity. The results were fitted to a Vogel – Fulcher - Tammann – equation.

$$\eta(T) = A \exp\left(\frac{B}{T - T_0}\right) \quad \textbf{(3.1)}$$

3.1.1.2 Density

Density measurements have been conducted using a home-built density meter based on an Anton Paar (Graz, Austria) L-Dens density transmitter for liquids. The OEM (Original Equipment Manufactured) parts have been equipped with an external thermal bath (5-90 °C). An LCD (Liquid Crystal Display) as well as a data transfer via RS232 allows single point measurements and temperature scans. The experimental error is ± 0.0002 g/ml (from 0.5000 to 2.0000) and ± 0.1 K (full range). The measured densities are linearly dependent on the temperature and were therefore fitted in this way. (equation (3.2)).

$$\rho(T) = a * T(K) + b \quad \textbf{(3.2)}$$

3.1.1.3 Dielectric parameters

Dielectric relaxation characterizes the rearrangement of a polar solvent by insertion of a changing electric field. This process appears in dependence on the particular solvent properties usually within a timescale of 1-100 ps, for organic solvents.

The dielectric behaviour of a solvent can be presented in form of Cole-Cole plots. A typical Cole-Cole plot of a Debye solvent like acetonitrile show one semi-circle, non-Debye solvents like the ILs show two or more semi-circles (see Figure 3.1) due to more than one relaxation processes. The abscissa presents the real part ε' of the relative permittivity ε, the ordinate presents the negative imaginary part ε''.

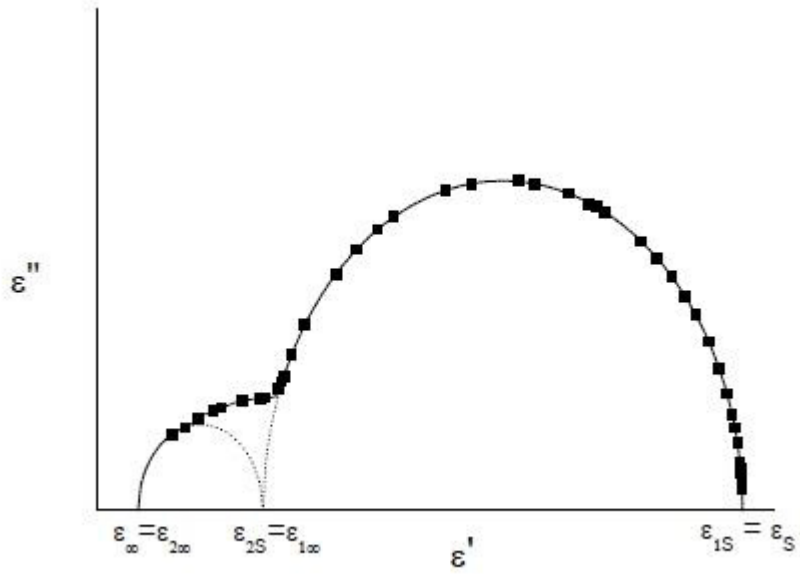

Figure 3.1: Cole-Cole plot for a solvent with two characteristic relaxation times. ©[56]

In the figure above are each of the two relaxations characterized by a low dielectric constant ε_{is}, a high dielectric constant $\varepsilon_{i\infty}$ and a relaxation time τ_{Di}. For a solvent with n relaxations is the static dielectric constant $\varepsilon_s=\varepsilon_{1s}$ and $\varepsilon_\infty=\varepsilon_{n\infty}$.According Hynes[31] and Fawcett [14, 15] is the frequency dependent dielectric response function after Laplace transformation given as

$$\hat{E}(s) = \sum_{i=1}^{n} \frac{f_i}{1 + s\tau_i} \tag{3.3}$$

with the definition of f_i

$$f_i = \frac{\varepsilon_{i0} - \varepsilon_{i\infty}}{\varepsilon_s - \varepsilon_\infty} \tag{3.4}$$

In the simplest case has the solvent only one Debye relaxation (n=1) with a longitudinal relaxation time τ_L given as in equation (3.5) with τ_D the Debye relaxation time.

$$\tau_L = \frac{\varepsilon_\infty \tau_D}{\varepsilon_s} \tag{3.5}$$

For solvents with two relaxation processes the estimation of τ_L gets more complex. The longitudinal relaxation time in such solvents varies between two limiting values $\tau_{L,0}$ and $\tau_{L,\infty}$.

$$\tau_{L,0} = \frac{\varepsilon_\infty}{\varepsilon_s}\left(f_1\tau_{D,1} + f_2\tau_{D,2}\right) \tag{3.6}$$

$$\tau_{L,\infty} = \frac{\varepsilon_\infty}{\varepsilon_s}\left(\frac{f_1}{\tau_{D,1}} + \frac{f_2}{\tau_{D,2}}\right)^{-1} \tag{3.7}$$

The transition between the two limits is determined by the time τ_m.

$$\tau_m = f_1\tau_{D,1} + f_2\tau_{D,2} \tag{3.8}$$

If the first relaxation process is dominant, which is the case for the investigated solvents in the present work, f_1 and $\tau_{D,1}$ are larger than f_2 and $\tau_{D,2}$ and $\tau_{L,0}$ is close to $\tau_{L,1}$. Hence, the longitudinal relaxation time $\tau_L = \tau_{L,\infty}$at very short times and $\tau_L = \tau_{L,0}$ at very long times.

$$\tau_L = \tau_0 + (\tau_\infty - \tau_0) * e^{\left(\frac{-t}{\tau_m}\right)} \quad \textbf{(3.9)}$$

Here, the time t describes the observed timescale. To estimate the observed timescale an example for two ILs will be discussed here. The rate constants k_{et} in Table 3-1 are extracted from the results part in chapter 4.3 and the rate constants k_{ex} are calculated via eq. (2.5) using the association constant K_0 = 0.42 M^{-1}[20]. The time t = $1/k_{ex}$ is arranged in the nanosecond region and therefore results equation (3.9) in $\tau_L = \tau_{L,0}$ for the ILs listed below.

Table 3-1: rate constants at 298 K of the self-exchange redox couple [TCNE/TCNE$^{\bullet-}$]

IL	k_{et} [$10^7 M^{-1}s^{-1}$]	k_{ex} [$10^8 s^{-1}$]	t [ns]
[$hmim^+$][Tf_2N^-]	9.19	2.19	4.57
[$bmim^+$][BF_4^-]	2.36	0.56	17.8

3.1.2 [emim$^+$][Tf$_2$N$^-$]

The structure of this ionic liquid is presented in Figure 3.2. The ionic liquid was purchased from io·li·tec Company (Germany) with the CAS-Nr. 174899-82-2. The most important specifications of the substance are the appearance (colourless to yellow), the water content (<100 ppm) and the halide content (<100 ppm).

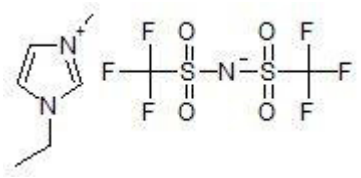

Figure 3.2: Structure of [emim$^+$][Tf$_2$N$^-$]

Before use, the IL was dried at 40-50°C in vacuo (< 5*10^{-5} Torr) for 24 h to remove water and subsequently stored under N_2 in a desiccator over P_4O_{10}. The IL used for measurements with the [TCNE/TCNE$^{\bullet-}$] redox couple was purified, prior to the high vacuum pump, by column chromatography over aluminium oxide (Al_2O_3, Fluka, type 504c acidic). The yellow IL was, after the purification, nearly colourless and did not show any reducing reaction with TCNE anymore. To be sure that the purification did not alter the properties of the IL, viscosity and density measurements with and without purification were done. In Figure 3.3 it appears that the purification method or in fact the impurities in the IL do not change the solvent properties noticeable.

3.1.2.1 Viscosity [emim$^+$][Tf$_2$N$^-$]

The temperature dependent viscosities are self- measured as described in chapter 3.1 and the results were fitted to a VFT–equation (3.1) (Vogel-Fulcher-Tammann). The resulting best-fit coefficients are listed in Table 3-2.

Table 3-2: Coefficients of best fit for equation (3.1) / [emim$^+$][Tf$_2$N$^-$]

η[mPa s] (298 K)	A [mPa s]	B [10^2 K]	T_0 [K]	Temperature range [K]
32.89	0.23±0.03	6.8±0.3	161±4	293-323

The pressure dependent viscosities are extracted from literature [1]. The viscosities are calculated via the Hybrid Tait-Litovitz equation (3.10)

$$\eta(p,T) = A\exp(\frac{B}{T^3})(\frac{D+p}{D+0{,}1})^E \qquad \textbf{(3.10)}$$

Table 3-3: Coefficients of best fit for equation (3.10) / [emim$^+$][Tf$_2$N$^-$]

η [mPa s] (296 K)	A [mPa s]	B [10^6 K^3]	D [MPa]	E
36.75	0.84±0.03	98±4	887±35	10.3±0.4

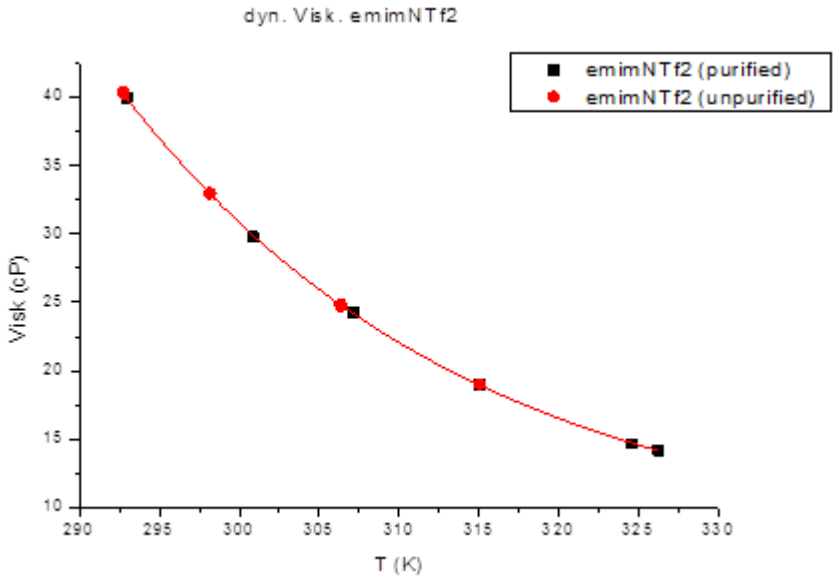

Figure 3.3: Temperature dependence of the viscosity of [emim$^+$][Tf$_2$N$^-$] purified and unpurified in comparison.

3.1.2.2 Density of [emim$^+$][Tf$_2$N$^-$]

The temperature dependent densities are calculated via eq. (3.2) with coefficients from Table 3-4.

Table 3-4: Coefficients of best fit for equation (3.2) / [emim$^+$][Tf$_2$N$^-$]

ρ (298K) [kg dm^{-3}]	a [10^{-4}kg dm^{-3} K^{-1}]	b [kg dm^{-3}]	Temperature range [K]
1.52	-9.7±0.2	1.810±0.007	293-323

The pressure dependent densities are extracted from literature [32] and calculated via a Tait-equation (3.11) and (3.12) with the related coefficients in Table 3-5

$$\rho(p, 296K) = \frac{\rho(296K, 0{,}1MPa)}{1 - C * \ln(\frac{B(T) + p}{B(T) + 0{,}1})} \quad (3.11)$$

$$B(T) = B_0 + B_1 T^1 + B_2 T^2 \quad (3.12)$$

Table 3-5: Coefficients of best fit for equation (3.11) / [emim$^+$][Tf$_2$N$^-$]

B$_1$ [MPa K^{-1}]	B$_2$ [10^{-3} MPa K^{-2}]	B$_0$ [MPa]	C [10^{-2} MPa K^{-2}]	B(T) / MPa
-1.546	1.284	579.62	8.849±0.001	1246.99±0.07

3.1.2.3 Refractive index [emim$^+$][Tf$_2$N$^-$]

The refractive indices are extracted from literature [68] and fitted linearly. To obtain the refractive index for each temperature, the coefficients in Table 3-6 were used.

$$n_D(T) = a * T(K) + b \quad (3.13)$$

Table 3-6 : Coefficients of best fit for equation (3.13) / [emim$^+$][Tf$_2$N$^-$]

n$_D$ (298K)	a [10^{-6} K^{-1}]	b	Temperature range [K]
1.422	-254±5	1.498±0.1	293-333

3.1.2.4 Summary of solvent properties for [emim$^+$][Tf$_2$N$^-$]

Table 3-7: Solvent properties of [emim$^+$][Tf$_2$N$^-$] at atmospheric pressure and different temperatures.

T [K]	ρ [kg m^{-3}]	n_D	ε_S	ε_∞	τ_L [ps]	n_D^2	η [mPa s]
288	1526	1.425				2.030	49.06
298	1517	1.422	12.25[(a)] 12.3[(c)]	3.23[(a)] 4.7[(c)]	58.92[(b)] 33.32[(d)]	2.023	32.89
308	1507	1.420				2.016	23.38
318	1497	1.417				2.009	17.41
328	1488	1.415				2.002	13.37
338	1478	1.412				1.994	10.78
348	1468	1.410				1.987	8.67
358	1459	1.407				1.980	7.19

[(a)] From Ref. [8]

[(b)] calculated via equation (3.9) with data from ref. [8]

[(c)] From Ref.[53]

[(d)] calculated via equation (3.9) with data from ref. [53]

Table 3-8: Solvent properties of [emim$^+$][Tf$_2$N$^-$] at 296K and elevated pressures.

P [MPa]	ρ [kg m^{-3}]	η [mPa s]
0.1	1519	36.75
10	1524	41.19
20	1530	46.16
30	1535	51.67
40	1540	57.77
50	1545	64.51
60	1550	71.95
70	1554	80.16
80	1559	89.20
90	1563	99.16
100	1568	110.10

3.1.3 [bmim$^+$][Tf$_2$N$^-$]

The structure of the ionic liquid is presented in Figure 3.4. The yellow to orange ionic liquid (CAS-Nr. 174899-83-3) was purchased from io·li·tec Company (Germany) with a water content <100 ppm and halides content <100 ppm. Before use, the IL was dried at 40-50°C in vacuo (< 5×10^{-5} Torr) for 24 h to remove water and subsequently stored under N_2 in a desiccator over P_4O_{10}. The IL used for measurements with the [TCNE/TCNE$^{\bullet-}$] redox couple was purified, prior to the high vacuum pump as follows. The IL was extracted with 3,7 % HCl in a separating funnel 4 times and subsequently washed with bidistilled water until the separated washing water was pH neutral.

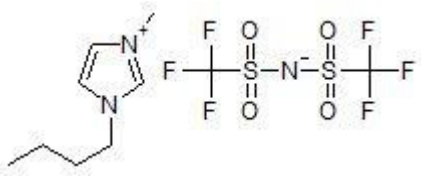

Figure 3.4 Structure of [bmim$^+$][Tf$_2$N$^-$]

3.1.3.1 Viscosity of [bmim$^+$][Tf$_2$N$^-$]

Best-fit coefficients for the VFT equation describing the self-measured temperature dependent viscosities are listed inTable 3-9.

Table 3-9: Coefficients of best fit for equation (3.1) / [bmim+][Tf2N-]

η [mPa s] (298 K)	A [mPa s]	B [10^2 K]	T_0 [K]	Temperature range [K]
51.73	0.18±0.002	7.4±0.3	168±3	293-343

The pressure dependent viscosities are extracted from literature [26]. The viscosities are calculated via a modified VFT- equation (3.14) with coefficients from Table 3-10.

$$\eta(T,p) = \exp(A + B * p + \frac{C + D * p + E * p^2}{T - T_0}) \quad \textbf{(3.14)}$$

Table 3-10: Coefficients of best fit for equation (3.14)/ [bmim$^+$][Tf$_2$N$^-$]

A	B [10^{-3}MPa^{-1}]	C [K]	D [K MPa^{-1}]	E [10^{-5}K MPa^{-1}]	T_0 [K]
-1,77±0.03	-0.96±0.09	755±10	1.71±0.02	-75±2	165.7±0.9

3.1.3.2 Density of [bmim$^+$][Tf$_2$N$^-$]

The densities for each temperature were calculated via (3.2) with the resulted best-fit coefficients (Table 3-11) from the temperature dependent density measurements like described in chapter 3.1.1.2.

Table 3-11: Coefficients of best fit for equation (3.2) / [bmim$^+$][Tf$_2$N$^-$]

ρ (298K) [kg dm^{-3}]	a [10^{-4}kg dm^{-3} K^{-1}]	b [kg dm^{-3}]	Temperature range [K]
1.44	-8.75±0.03	1.697±0.001	293-343

Calculation of the pressure dependent densities at 298 K were done via a polynomial function eq. (3.15) with best-fit coefficients extracted from literature [26].

$$\rho = A + Bp + Cp^2 \quad \textbf{(3.15)}$$

Table 3-12: Coefficients of best fit for equation (3.15) / [bmim$^+$][Tf$_2$N$^-$]

A [kg dm^{-3}]	B [10^{-5}kg dm^{-3}bar^{-1}]	C [10^{-8}kg dm^{-3}bar^{-2}]
1.4366	7.33	-1.36

3.1.3.3 Refractive index of $[bmim^+][Tf_2N^-]$

The temperature dependent refractive indices are calculated according to equation (3.13) with the best-fit coefficients extracted from literature [68].

Table 3-13: Coefficients of best fit for equation (3.13)/ $[bmim^+][Tf_2N^-]$

n_D (298K)	a [10^{-6} K^{-1}]	b	Temperature range [K]
1.426	-296±9	1.514±0.003	293-333

3.1.3.4 Summary of solvent properties for $[bmim^+][Tf_2N^-]$

Table 3-14: Solvent properties of $[bmim^+][Tf_2N^-]$ at atmospheric pressure and different temperatures.

T [K]	ρ [kg m^{-3}]	n_D	ε_S	ε_∞	τ_L [ps]	n_D^2	η [mPa s]
288	1445	1.4299				2.045	83.26
298	1437	1.4269	11.52[a] 13.7[c]	3.03[a] 4.25[c]	112.1[b] 132.2[d]	2.036	51.73
308	1428	1.4239				2.028	34.55
318	1419	1.4210				2.019	24.35
328	1410	1.4180				2.011	17.92
338	1402	1.4151				2.002	13.68
348	1393	1.4121				1.994	10.753
358	1384	1.4092				1.986	8.689

[a] Extracted from Ref. [8], [b] calculated via equation (3.9) with Data from Ref. [8], [c] Extracted from Ref.[53]
[d] calculated via equation (3.9) with Data from Ref.[53]

Table 3-15: Solvent properties of $[bmim^+][Tf_2N^-]$ at 296K and elevated pressures.

p [MPa]	ρ [kg m^{-3}]	η [mPa s]	p [MPa]	ρ [kg m^{-3}]	η [mPas]
0.1	1437	56.06	60	1476	116.18
10	1444	63.24	70	1481	131.21
20	1451	71.42	80	1487	148.19
30	1457	80.66	90	1492	167.36
40	1464	91.09	100	1496	189.01
50	1470	102.87			

3.1.4 [hmim$^+$][Tf$_2$N$^-$]

The structure of the ionic liquid is presented in Figure 3.5. The ionic liquid was purchased from io·li·tec company (Germany) with the CAS-Nr. 382150-50-7. The water and halides content is smaller than 100 ppm and the colour of the IL may vary from colorless to orange. Before use, the IL was dried at 40-50°C in vacuo (< 5×10^{-5} Torr) for 24 h to remove water and subsequently stored under N_2 in a desiccator over P_4O_{10}. The IL used for measurements with the [TCNE/TCNE$^{\bullet-}$] redox couple was purified, prior to the high vacuum pump as follows. The IL was extracted with 3,7 % HCl in a separating funnel 10 times and subsequently washed with bidistilled water until the separated washing water was of neutral pH. Subsequently a column chromatography over silica gel 60 (Roth, 0.06-0.2 mm) was needed to remove all of the reducing impurities.

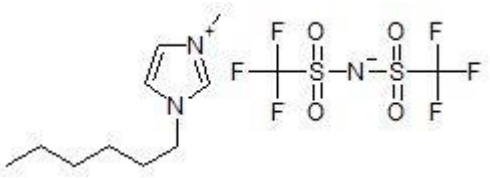

Figure 3.5 Structure of [hmim$^+$][Tf$_2$N$^-$]

3.1.4.1 Viscosity of [hmim$^+$][Tf$_2$N$^-$]

The self- measured temperature dependent viscosities (chapter 3.1.1.1) were fitted to a VFT- equation (3.1) with resulting coefficients of best fit listed in the following table.

Table 3-16: Coefficients of best fit for equation (3.1) / [hmim$^+$][Tf$_2$N$^-$]

η [mPa s] (298 K)	A [mPa s]	B [K]	T_0 [K]	Temperature range [K]
72.19	0.14 ± 0.02	818 ± 32	166 ± 3	293 - 328

3.1.4.2 Density of [hmim$^+$][Tf$_2$N$^-$]

For the calculation of the temperature dependent densities eq. (3.2) was used with appropriate coefficients from Table 3-17.

Table 3-17: Coefficients of best fit for equation (3.2) / [hmim$^+$][Tf$_2$N$^-$]

ρ (298K) [kg dm^{-3}]	a	b	Temperature range [K]
1.37	-0.000923	1.6452	293 - 327

3.1.4.3 Refractive index of [hmim$^+$][Tf$_2$N$^-$]

The temperature dependent refractive indices from Ref. [52] were fitted linearly and calculated according equation (3.13) with the following best-fit coefficients.

Table 3-18: Coefficients of best fit for equation (3.13) / [hmim$^+$][Tf$_2$N$^-$]

n_D (298K)	a [10^{-6} K^{-1}]	b	Temperature range [K]
1.430	-187±5	1.486±0.002	303-333

3.1.4.4 Dielectric Properties of [hmim$^+$][Tf$_2$N$^-$]

The used dielectric properties for [hmim$^+$][Tf$_2$N$^-$] were extracted from literature [34]. All other values in Table 3-19 were calculated as described in chapter 3.1.1.3.

Table 3-19: Dielectric properties for [hmim$^+$][Tf_2N^-]

T[K]	ε_s(a)	$\tau_{D,1}$ (a) [ps]	$\varepsilon_{\infty,1}$(a)	$\tau_{D,2}$ (a) [ps]	ε_∞(a)	f_1(b)	f_2(b)	$\tau_{L,0}$ (c)[ps]	$\tau_{L,\infty}$ (d)[ps]	τ_m (e)[ps]	τ_l (f)[ps]
278	13.8	925	3.2	0.8	2.77	0.9610	0.0390	178.44	4.03	888.97	178.44
288	12.1	299	3.38	0.8	2.71	0.9286	0.0714	62.20	2.43	277.72	62.20
298	12.7	233	3.3	0.8	2.58	0.9289	0.0711	43.98	2.19	216.48	43.98
308	11.6	128	3.49	0.69	2.4	0.8815	0.1185	23.36	1.16	112.92	23.36
318	11.9	107	3.5	0.8	2.52	0.8955	0.1045	20.31	1.52	95.90	20.31
328	11.3	73.1	3.62	0.8	2.38	0.8610	0.1390	13.28	1.14	63.05	13.28
338	11.2	64	3.64	1.2	2.66	0.8852	0.1148	13.49	2.17	56.79	13.49

(a) values extracted from Ref.[34], (b) calculated via equation (3.4), (c) calculated via equation (3.6), (d) calculated via equation (3.7), (e) calculated via equation (3.8), (f) calculated via equation (3.9)

To obtain the dielectric parameters for each temperature the static permittivity ε_s and the infinite frequency permittivity ε_∞ were fitted linearly (equation (3.16)), with resulting the parameters listed in Table 3-20.

$$\varepsilon(T) = a * T(K) + b \tag{3.16}$$

Table 3-20: Coefficients of best fit for equation (3.16)/ [hmim$^+$][Tf_2N^-]

ε (298K)	a	b	Temperature range [K]
12.5	-0.036±0.009	23±3	278-328
ε_∞ (298K)			
2.6	-0.008±0.002	4.9±0.5	278-328

3.1.4.5 Summary of solvent properties for [hmim$^+$][Tf$_2$N$^-$]

Table 3-21: Solvent properties of [hmim$^+$][Tf$_2$N$^-$] at atmospheric pressure and different temperatures.

T [K]	ρ [kg m^{-3}]	n_D	ε_S	ε_∞	τ_L [ps]	n_D^2	η [mPa s]
288	1379	1.4322	12.82	2.68	58.62	2.0512	120.08
298	1370	1.4303	12.46	2.60	40.40	2.0459	71.85
308	1361	1.4285	12.09	2.52	28.53	2.0405	46.23
318	1352	1.4266	11.73	2.45	20.59	2.0352	31.53
328	1342	1.4247	11.36	2.37	15.16	2.0299	22.55
338	1333	1.4229	11.00	2.29	11.36	2.0245	16.77
348	1324	1.4210	10.63	2.21	8.66	2.0192	12.89
358	1315	1.4191	10.27	2.14	6.70	2.0139	10.18

3.1.5 [bmim$^+$][BF$_4^-$]

The ionic liquid presented in Figure 3.6 was purchased from io·li·tec company (Germany) with the CAS-Nr. 174501-65-6. The IL with a yellow to orange appearance has with <250 ppm slightly higher water content than the previous mentioned ILs. The halide content (<100 ppm) however is in the same condition. After the drying procedure (40-50°C, < 5×10^{-5} Torr, 24 h) the IL was stored under N_2 in a desiccator over P_4O_{10}. The IL did not show any reducing impurities and could therefore be used without any additional purification for measurements with TCNE.

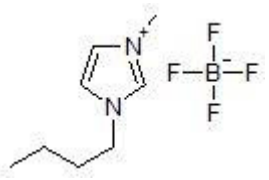

Figure 3.6 Structure of [bmim$^+$][BF$_4^-$]

3.1.5.1 Viscosity of [bmim$^+$][BF$_4^-$]

The temperature dependent viscosities are extracted from literature [7] and calculated according to equation (3.17) with the fitting parameters in Table 3-22.

$$\eta(T) = AT^{0,5}\exp\left(\frac{B}{T-T_0}\right) \qquad (3.17)$$

Table 3-22: Coefficients of best fit for equation (3.17)/ [bmim$^+$][BF$_4^-$]

η [mPa s] (298 K)	A [mPa s K$^{-0,5}$]	B [K]	T_0 [K]	Temperature range [K]
106.0±0.1	0.0061	885	170	293 - 353

3.1.5.2 Density of [bmim$^+$][BF$_4^-$]

The temperature dependent densities for [bmim$^+$][BF$_4^-$] were calculated via a polynomial function (3.18) with best-fit coefficients extracted from literature [67].

$$\rho = A_0 + A_1 T + A_2 T^2 \qquad \textbf{(3.18)}$$

Table 3-23 Coefficients of best fit for equation (3.18) / [bmim$^+$][BF$_4^-$]

ρ (298K) [kg dm^{-3}]	A_0 [kg dm^{-3}]	A_1 [10^{-4} kg K^{-1}dm^{-3}]	A_2 [10^{-7}kg K^{-2}dm^{-3}]	Temperature range [K]
1.20	1.44333	-9.10294	3.22186	293 - 353

3.1.5.3 Refractive index of [bmim$^+$][BF$_4^-$]

The refractive indices are as well as the densities extracted from ref [67] and were fitted linearly. The temperature dependent refractive indices were calculated according equation (3.13) with coefficients listed below.

Table 3-24: Coefficients of best it for equation (3.13) / [bmim$^+$][BF$_4^-$]

n_D (298K)	a [10^{-6} K^{-1}]	b	Temperature range [K]
1.424	242±3	1.4970±0.0009	293 - 353

3.1.5.4 Dielectric Properties of [bmim$^+$][BF$_4^-$]

The dielectric properties of [bmim$^+$][BF$_4^-$] extracted from ref. [34] were used for a linear fit as described in chapter 3.1.4.4 for [hmim$^+$][Tf$_2$N$^-$]. The temperature dependent static permittivity ε_s and infinite frequency permittivity ε_∞ were calculated via equation (3.16) with the resulting parameters in Table 3-26. The relaxation parameters in Table 3-25 were calculated as described in chapter 3.1.1.3.

Table 3-25: Dielectric properties for [bmim$^+$][BF$_4^-$]

T[K]	ε_s(a)	$\tau_{D,1}$ (a) [ps]	$\varepsilon_{\infty,1}$(a)	$\tau_{D,2}$ (a) [ps]	ε_∞(a)	f_1(b)	f_2(b)	$\tau_{L,0}$ (c)[ps]	$\tau_{L,\infty}$ (d)[ps]	τ_m (e)[ps]	τ_l (f)[ps]
278	14.4	670	4.3	0.26	1.1	0.7594	0.2406	38.87	0.08	508.86	38.87
288	14.1	351	4.46	0.4	1.72	0.7787	0.2213	33.35	0.22	273.40	33.35
298	14.6	284	4.6	0.62	2.57	0.8313	0.1687	41.57	0.64	236.18	41.57
308	13.8	140	4.71	0.8	2.98	0.8401	0.1599	25.43	1.05	117.74	25.43
318	13.3	93.7	4.87	0.94	3.11	0.8273	0.1727	18.16	1.21	77.68	18.16
328	12.5	59.4	4.94	0.97	3.17	0.8103	0.1897	12.25	1.21	48.32	12.25
338	12.5	52.5	5.16	1.42	3.56	0.8210	0.1790	12.35	2.01	43.36	12.35

(a) values extracted from Ref.[34], (b) calculated via equation (3.4), (c) calculated via equation (3.6), (d) calculated via equation (3.7), (e) calculated via equation (3.8), (f) calculated via equation (3.9)

Table 3-26: Coefficients of Best Fit for equation (3.16)/ [bmim$^+$][BF$_4^-$]

ε_s (298K)	a	b	Temperature range [K]
13.97	-0.036±0.007	25±2	278-338
ε_∞ (298K)	a	b	Temperature range [K]
2.21	0.039±0.006	-9±2	278-338

3.1.5.5 Summary of solvent properties for [bmim$^+$][BF$_4^-$]

Table 3-27: Solvent properties of [bmim$^+$][BF$_4^-$] at atmospheric pressure and different temperatures.

T [K]	ρ [kg m^{-3}]	n_D	ε_S	ε_∞	τ_L [ps]	n_D^2	η [mPa s]
288	1217	1.4273	14.33	1.82	36.37	2.0372	187.17
298	1211	1.4249	13.97 14.1[(a)]	2.21 5.45[(a)]	28.54 290[(b)]	2.0303	105.97
308	1204	1.4225	13.61	2.60	22.75	2.0234	65.28
318	1198	1.4200	13.24	2.98	18.39	2.0165	43.00
328	1191	1.4176	12.88	3.37	15.07	2.0097	29.91
338	1185	1.4152	12.51	3.75	12.49	2.0028	21.76
348	1178	1.4128	12.15	4.14	10.46	1.9960	16.42
358	1171	1.4104	11.78	4.53	8.85	1.9891	12.78

[(a)] From Ref.[53]

[(b)] calculated via equation (3.9) with Data from Ref.[53]

3.1.6 Dimethylphthalate

The solvent Dimethylphthalate (DMP, CAS 131-11-3) was purchased from Fluka with a purity grade of 98%. The liquid was dried over 4Å molecular sieve and distilled afterwards in vacuo and stored under nitrogen.

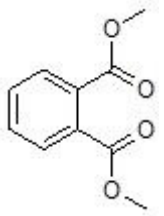

Figure 3.7: Structure of DMP

3.1.6.1 Viscosity of DMP

The temperature dependent viscosities are self- measured as described in chapter 3.1 and calculated via equation (3.1) with coefficients in Table 3-28.

Table 3-28: Coefficients of best fit for equation (3.1) / DMP

η [mPa s] (298 K)	A [mPa s]	B [K]	T_0 [K]	Temperature range [K]
13.64	0.23±0.01	344±10	213±1	283 - 353

3.1.6.2 Density of DMP

The self-measured temperature dependent densities (see chapter 3.1.1.2) were fitted linearly. With the coefficients from Table 3-29 was it possible to calculate densities for each used temperature via equation (3.2).

Table 3-29: Coefficients of best fit for equation (3.2) / DMP

ρ (298K) [kg dm^{-3}]	a [10^{-4} kg dm^{-3} K^{-1}]	b [kg dm^{-3}]	Temperature range [K]
1.18	-9.0±0.1	1.450±0.004	283 - 353

3.1.6.3 Dielectric properties of DMP

The static dielectric constants ε_s were extracted from literature [17] and fitted linearly according to equation(3.16). The resulting coefficients are listed below.

Table 3-30: Coefficients of best fit for equation (3.16) / DMP

ε_s (298K)	a	b	Temperature range [K]
8.37	-0.0130±0.0006	12.2±0.2	298-318

3.1.6.4 Summary of solvent properties for DMP

Table 3-31: Solvent properties of DMP at atmospheric pressure and different temperatures.

T [K]	ρ [kg m^{-3}]	n_D	ε_S	n_D^2	η [mPa s]
298	1184	1.5149(a)	8.37	2.2949	13.65
308	1175		8.25		9.00
318	1166		8.12		6.31
328	1157		7.99		4.73
338	1148		7.86		3.71
348	1139		7.73		3.02
358	1130		7.60		2.52
368	1121		7.47		2.16

(a) extracted from Ref. [17]

3.1.7 Acetonitrile

The acetonitrile (AN) used from Sigma-Aldrich, 99.8%, CAS: 75-05-8 was dried over 3Å molecular sieve. The solvent was kept after a distillation under nitrogen in an appropriate Schlenk flask.

3.1.7.1 Densities of AN

The pressure and temperature dependent viscosities are extracted from literature [24] and calculated via equation (3.19)

$$\rho(P,T) = 0{,}7766\left(\frac{P + 3403 - 7{,}53T}{1 + 3403 - 7{,}53}\right)^{0{,}125} \qquad \textbf{(3.19)}$$

$$* \exp(-3{,}304 * 10^{-4}[T - 298{,}25] - 1{,}756 * 10^{-6}[T^2 - 298{,}25^2])$$

3.1.7.2 Viscosity of AN

The densities used, were calculated via equation (3.20) which was taken from ref.[24]. This equation includes both the temperature dependence and the pressure dependence.

$$\eta(p,T) = 10^{(-1{,}757+(\frac{386}{T})}(1 + 6{,}263 * 10^{-4}[p - 1]) \qquad \textbf{(3.20)}$$

3.1.7.3 Refractive index of AN

The refractive indices are approximated as given in [65] via the Lorenz-Lorenz equation

$$n^2 = \frac{\rho + 2Q}{\rho - Q} \tag{3.21}$$

The correction factor Q given in equation (3.22) is nearly independent of pressure and temperature.

$$Q = \frac{n_D^2 - 1}{n_D^2 + 2} \tag{3.22}$$

The correction factor was calculated using literature values of the refractive index[65].

3.1.7.4 Summary of solvent properties for AN

Table 3-32: Solvent properties of AN at elevated pressure and 296K

p [MPa]	ρ [kg m^{-3}]	n_D	ε_S[(a)]	n_D^2	η [mPas]
0.1	780.1	1.7949	37.50	1.3397	0.36
10	787.9	1.7848	37.90	1.3360	0.38
20	795.4	1.7756	38.30	1.3325	0.40
30	802.4	1.7671	38.65	1.3293	0.42
40	808.9	1.7593	39.00	1.3264	0.44
50	815.2	1.7521	39.30	1.3237	0.47
60	821.1	1.7453	39.60	1.3211	0.49
70	826.7	1.7390		1.3187	0.51
80	832.1	1.7331	40.15	1.3165	0.53
90	837.2	1.7275		1.3143	0.56
100	842.1	1.7222	40.65	1.3123	0.58

[(a)]… values for 293 K extracted from literature Ref. [28]

3.1.8 Solvent mixture

An additional task of this thesis was to test a special solvent mixture composed of propyl acetate (PA), Aldrich 99% CAS:109-60-4, butyronitrile (BN), Alfa Aesar 99% CAS: 109-74-0 and diethyl phthalate (DEP), Merck 99% CAS: 84-66-2. The used solvents were bubbled by nitrogen over a few minutes to remove the remaining oxygen in the solution. The degassed solutions were kept under nitrogen in a Schlenk tube. The composition of the mixtures are extracted from ref.[69]. Solvent mixtures at three different temperatures were used and their compositions are listed in the tables below.

Table 3-33: Mole fraction X of the components in the used solvent mixtures at 298K and the associated solvent properties extracted from Ref. [69]**.**

Mixture	T[K]	$X_{[PA]}$	$X_{[BN]}$	$X_{[DEP]}$	ε_s	η [mPa s]	n_D
M1a	298	0.970	0.000	0.030	5.9	0.6135	1.3884
M1b	298	0.780	0.195	0.025	8.6	0.6055	1.3890
M1c	298	0.590	0.390	0.025	11.6	0.6062	1.3883
M1d	298	0.390	0.585	0.025	15.1	0.6108	1.3894
M1e	298	0.200	0.780	0.020	18.7	0.6064	1.3885
M1f	298	0.000	0.980	0.020	23.4	0.6054	1.3886

Table 3-34: Mole fraction X of the components in the used solvent mixtures at 288K and the associated solvent properties extracted from Ref. [69]**.**

Mixture	T[K]	$X_{[PA]}$	$X_{[BN]}$	$X_{[DEP]}$	ε_s	η [mPa s]	n_D
M1j	288	0.8	0.2	0	8.9	0.6277	1.3871
M1h	288	0.4	0.6	0	16.0	0.6287	1.3868
M1i	288	0	1.0	0	25.2	0.6298	1.3877

Table 3-35 Mole fraction X of the components in the used solvent mixtures at 328K and the associated solvent properties extracted from Ref. [69]**.**

Mixture	T[K]	$X_{[PA]}$	$X_{[BN]}$	$X_{[DEP]}$	ε_s	η [mPa s]	n_D
M155b	328	0.69	0.170	0.140	7.5	0.6027	1.4011
M155c	328	0.52	0.345	0.135	9.6	0.6051	1.4007
M155e	328	0.175	0.700	0.125	14.8	0.6051	1.4016

3.2 Redox couples

The redox couples TTF / $TTF^{\bullet+}$, TCNE / $TCNE^{\bullet-}$ and DDQ / $DDQ^{\bullet-}$ were investigated within this work. The neutral substances and the appropriate radicals are the acceptor A and donor A^- molecule.

Preparation of the substances and structure information for the molecules and the precursor complexes are described in detail in the subsequent chapters.

3.2.1 TTF / $TTF^{\bullet+}$

Tetrathiafulvalene (TTF, CAS: 31366-25-3) was purchased from Fluka with a purity grade of 99%.The substance was sublimated in vacuo and the orange substance was stored in a Schlenk tube under nitrogen.

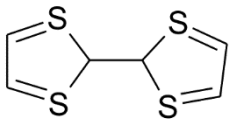

Figure 3.8: Structure of TTF

The $TTF^{\bullet+}$ radical cation was synthesized as a perchlorate salt ($TTF^{\bullet+}ClO_4^-$) as described by Hünig [30]. The sublimated TTF (0.255 g) was solved in 100 ml acetic acid (100 %) under stirring and gives an ochre brown solution. Afterwards a solution of 0.283 g Lead(IV) acetate in 8.5 ml acetic acid was added drop wise during cooling so that the solution keeps at room temperature. The solution gets dark brown to black and was stirred additionally 10 minutes. Afterwards a solution of 0.615 g sodium perchlorate ($NaClO_4$) in 25 ml distilled water and 5 ml perchloric acid (70%, $HClO_4$) was added. The solution crystallized by cooling with an ice bath. The brown crystals were filtered and washed with carbon tetrachloride (CCl_4) and dried in a desiccator over diphosphorus pentoxide (P_4O_{10}). The dry crystals were stored in a Schlenk tube under nitrogen.

The structure of the TTF/$TTF^{\bullet+}$ precursor complex is expected to be slightly shifted along the long semiaxis as given from crystal structure.

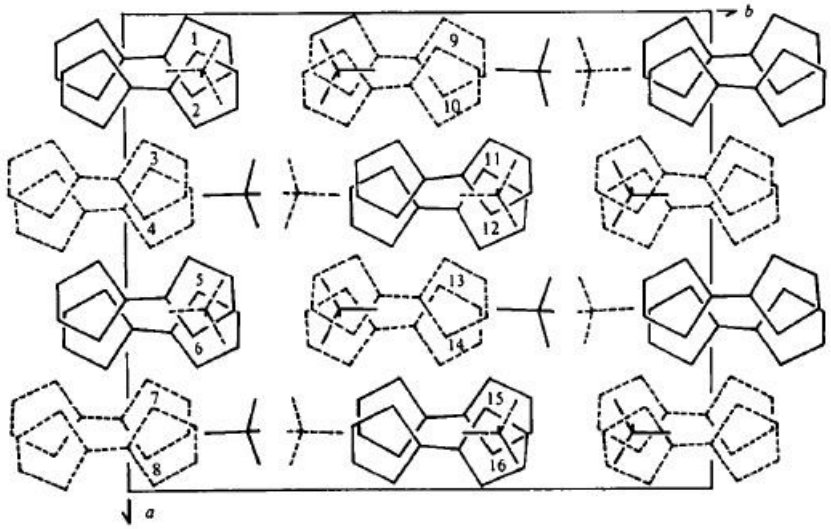

Figure 3.9: Crystall structure of the TTF perchlorate along the c-axis.©[73]

The geometrical data of the TTF/$TTF^{\bullet+}$ precursor complex can be estimated by the structure of a TTF cation dimer as described in ref.[73] or via an ellipsoid model described in ref.[20]. The semiaxis in the ellipsoid model are given as a=0.500 nm, b=0.270 nm and c=0.170 nm.

Table 3-36: Description of the transition state complex TTF/$TTF^{+\cdot}$ with the reaction distance d, the geometrical term g(r,d), the mean elliptical radius r and the resonance splitting energy V_{RP}

$r^{(a)}$ [nm]	$d_{(cryst.)}$ [nm]	$d_{(exp.)}{}^{(c)}$ [nm]	$d^{(b)}{}_{(Kharkats)}$ [nm]	$g(r,d)^{(h)}{}_{(exp)}$ [10^8 m^{-1}]	$\lambda_{i,\infty}$ [kJ mol^{-1}]	V_{RP} [kJ mol^{-1}]
0.304[20]	0.340[73] $0.342^{(g)}$	0.34±0.02 [20]	0.51[20]	3.3±0.8 [20]	34.9 [20] 27.2[59]	$4.0^{(d)}$[20] $8.9^{(e)}$[20] $19.1^{(f)}$[61]

$^{(a)}$from equation (2.25), $^{(b)}$from equation (2.26), $^{(c)}$from equation (2.24) with $g(r,d)_{(exp)}$, $^{(d)}$calculated from $\gamma_{LZ}=1$

$^{(e)}$from overlap integrals, $^{(f)}$experimental value (used solvent CH_2Cl_2),

$^{(g)}$CDFT(constrained density functional theory) calculations Ref.[59], $^{(h)}$ experimental values (293 K different solvents)

3.2.2 DDQ / $DDQ^{\bullet-}$

The yellow 2,3-Dichloro-5,6-dicyano-1,4-benzoquinone (DDQ, CAS: 84-58-2) was purchased from Fluka with a purity grade of 97%.

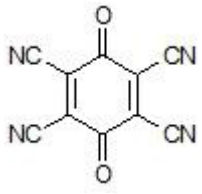

Figure 3.10: Structure of DDQ

The radical $DDQ^{\bullet-}$ was produced in situ in the DDQ solution at a certain concentration by adding equimolar tetrabutylammonium iodide (TBAI). The TBAI reduces the DDQ to the radical anion $DDQ^{\bullet-}$ with TBA^{+} as counterion (see eq. (3.23)). The choice to use TBA^{+} is because of the voluminous structure of that ion which prevents any ion pairing effects.

$$2\,DDQ + 2\,TBA^{+}I^{-} \rightarrow 2\,DDQ^{\bullet-} + 2\,TBA^{+} + I_2 \qquad (3.23)$$

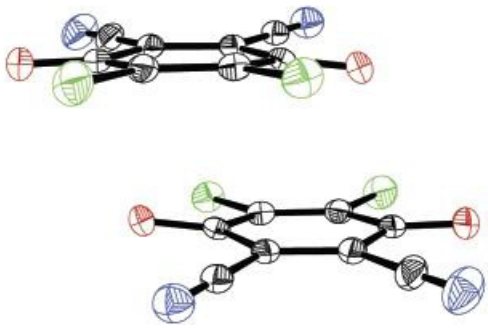

Figure 3.11:Activated complex of DDQ/$DDQ^{\bullet-}$©Ref.[61]

Table 3-37: Description of the transition state complex DDQ / $DDQ^{\bullet-}$ with the reaction distance d, the geometrical term g(r,d), the mean elliptiacal radius r and the resonance splitting energy V_{RP}

$r^{(a)}$ [nm]	$d_{(cryst.)}$ [nm]	$d_{(exp.)}^{(c)}$ [nm]	$d^{(b)}_{(Kharkats)}$ [nm]	$g(r,d)_{(exp)}$ [10^8 m^{-1}]	$\lambda_{i,\infty}$ [kJ mol^{-1}]	V_{RP} [kJ mol^{-1}]
0.459 [42]	0.29 [18]	0.30 [21]	0.848 [42]	10.0[21]	40.9 [42]	21.1 [42]
0.23[d] [18]				9.4[56]		13.4 [18]

[a]from equation (2.25), [b]from equation (2.26)

[c]from equation (2.24) with $g(r,d)_{(exp)}$, [d]experimental value

3.2.3 TCNE / $TCNE^{\bullet-}$

Tetracyanoethylene (TCNE, 670-54-2) was purchased from Fluka with a purity grade of 97%.

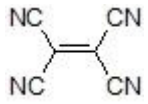

Figure 3.12: Structure of TCNE

The TCNE radical anion was produced in situ with $[bmim^+][I^-]$ as reducing agent in the sample or was added in form of the TBA salt. The $TCNE^{\bullet-}TBA^+$ was synthesized like described in [18]. Figure 3.13 shows the structure of the $[TCNE_2]^{2-}$ dimer with the interplanar distance of 2.87 Å obtained from the crystal structure [39].

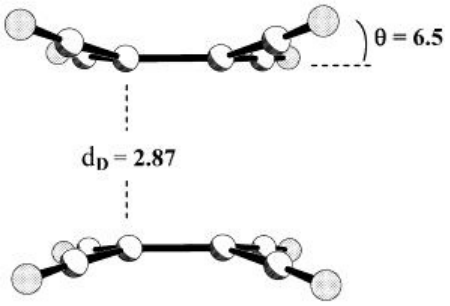

Figure 3.13: Dimeric pair of $TCNE^{\bullet-}$ in a $TCNE^{\bullet-}$ $(Bu_4N)^+$ crystal structure with an interplanar distance d.©[39]

Table 3-38: Description of the transition state complex TCNE / $TCNE^{\bullet-}$ with the reaction distance d, the geometrical term g(r,d), the mean elliptical radius r and the resonance splitting energy V_{RP}

$r^{(a)}$ [nm]	$d_{(cryst.)}$ [nm]	$d_{(exp.)}^{(c)}$ [nm]	$d^{(b)}_{(Kharkats)}$ [nm]	$g(r,d)_{(exp)}$ [10^8 m^{-1}]	K_0 [dm^3 mol^{-1}]	$\lambda_{i,\infty}$ [kJ mol^{-1}]	V_{RP} [kJ mol^{-1}]
0.310[20]	0.370[20]	0.44±0.02 [20]	0.55[20]	9.6±0.7 [20]	0.42	27.1 [59]	$4.7^{(d)}$[20]
	0.287[39]						$0.21^{(e)}$[20]
	$0.35^{(g)}$	0.42±0.02 [20]	0.53[20]	8.2±0.7 [20]	0.40		$9.45^{(f)}$[18]

[(a)]from equation (2.25),[(b)]from equation (2.26), [(c)]from equation (2.24) with $g(r,d)_{(exp)}$, [(d)]calculated from γ_{LZ}=1
[(e)]from overlap integrals, [(f)]experimental value (in acetonitrile), [(g)]CDFT calculations Ref.[59]

3.3 Apparatus

During the course of this work two ESR spectrometers were used. The Bruker spectrometer was used for the temperature dependent experiments and the Jeol spectrometer was used for the pressure dependent experiments. This chapter provides a description of the used ESR spectrometers and the associated sample preparation.

3.3.1 Bruker ELEXSYS E500 / Temperature unit

The temperature dependent ESR spectra were recorded with a Bruker ELEXSYS E500 X-Band spectrometer. The instrument is equipped with a temperature control unit (ER4131VT) working at temperatures 100-500K.

For the sample preparation a special glass construction (Figure 3.14) was used which enables the sealing of the sample solution under elimination of air.

Figure 3.14: Sample preparation under elimination of air.

The glass construction was connected to a one-way Pasteur pipette (sealed at the cone end) via a screw cap. This installation was evacuated and vented with nitrogen 3 times. After that, the sample was filled via a transfer pipette under nitrogen into the Pasteur

pipette. The system was afterwards closed and frozen by dunking the Pasteur pipette into a Dewar vessel with liquid nitrogen. The frozen system was evacuated and closed again afterwards before the sample was melted. Through the melting process the remaining gas in the sample solution was removed. This so called freeze-pump-thaw steps were repeated 3 times and finished by sealing the Pasteur pipette in vacuo.

3.3.2 Jeol 3-PX / high-pressure unit

The pressure dependent ESR spectra were recorded with a Jeol 3-PX X-band spectrometer equipped with a home built high-pressure unit [40, 57]. The high-pressure unit was modified by a high-pressure ESR cell. The construction of the ESR cell was done during this work and is made of a fused silica capillary[1] (o.d.:370 µm, i.d.:100 µm) according to Hubbell [50] and Yonker [55]. A silica capillary with a length of around 2 m was bent in a glass blower flame 20-24 times.

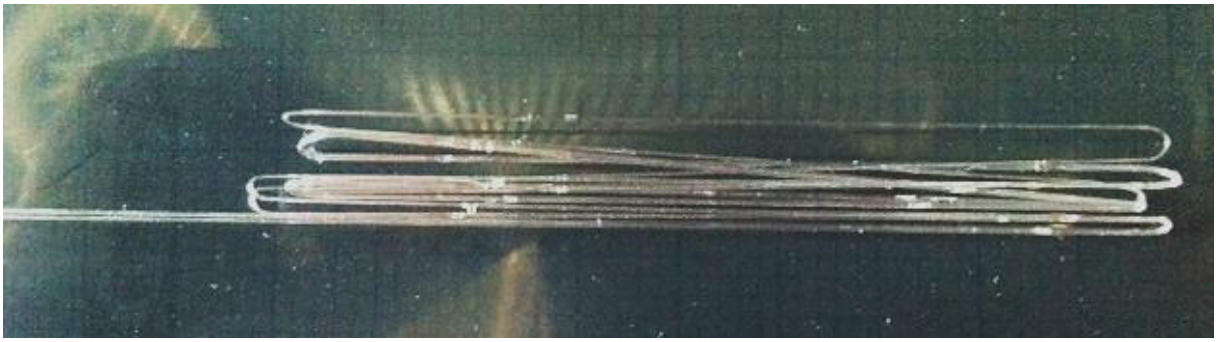

Figure 3.15: High pressure ESR cell

The capillary was connected to the pressure generating part via a VHP Micro Ferrule 360µm (Kinesis). Through an additionally added vessel at the end of the capillary it is possible to clean and fill the cell easily. The sample pressure was varied between 0.1 and 100 MPa at 296 K. The structure of the high pressure unit is illustrated in the diagram in Figure 3.16. Before filling the system with the sample, the system was completely evacuated. In the meantime the sample was filled in the sample reservoir and bubbled

[1] Polymicro Technologies

with nitrogen to avoid contact with air. Afterwards the vacuum was used to fill the sample side of the system with the sample. By pulling the separation disc in direction of the pressure generating part the media exchanger was filled with the sample solution. After closing all valves at the sample side the pressure generating side was evacuated and filled with the transmission fluid ethylene glycol. After closing all remaining valves the solution was pressed via the mechanical hand pump into the high pressure cell. Because of the high viscosity in the case of ILs this step takes longer and needs a bit of patience. When the solution dripped out of the valve at the end, the filling of the ESR cell was finished and the end valve could be closed. Now the pressure could be adjusted and ESR measurement started.

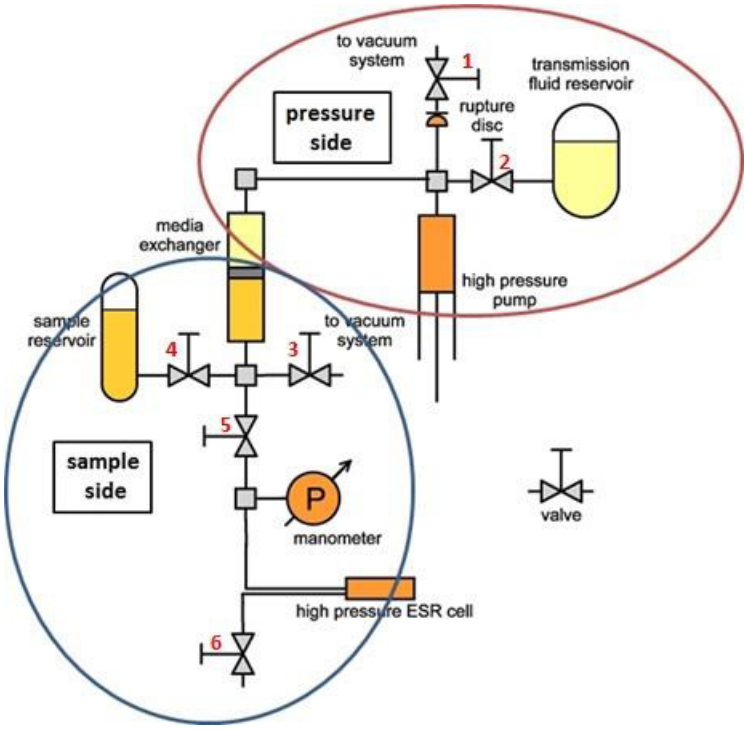

Figure 3.16: Scheme of the high pressure unit.

Step by Step instruction for filling:

1. The separation disc has to be completely pushed to the sample side
2. Switch on vacuum pump
3. Close valve 1, 2, 4, 6 and open valve 5 and 3 -> evacuation
4. Connect the empty sample reservoir with the nitrogen line
5. Close valve 3 and open valve 4 -> ventilation with nitrogen
6. Close valve 4 and open valve 3 -> evacuation
7. Repeat step 5. and 6
8. Close valve 3
9. Fill the sample reservoir and bubble nitrogen through the solution
10. Open valve 4 and move the separation disc to the pressure side
11. Close valve 4
12. Open valve 1 -> evacuation of the pressure side
13. Close valve 1 and open valve 2
14. Filling of the high pressure pump with the transmission fluid by screwing the mechanical regulation
15. Close valve 2
16. Open valve 6 -> screwing of the high pressure regulation slowly until the solution drops out of valve 6. By filling the system with ILs do not exceed the pressure of 400 MPa. Brakes during the filling process meanwhile the pressure can drop down are advised
17. Valve 6 should stay open until the pressure drops down to standard atmospheric pressure
18. After closing valve 6 the measurements can start

3.4 Interpretation of the ESR spectra

All ESR- spectra expect those measured in the solvent mixtures were simulated with a home written computer program. The program is written in Matlab and Fortran 95 and is based on the density matrix algorithm and simulates spectra based on an advanced quantum mechanical approach [22]. An advantage of the program is the separate simulation of each ESR line which allows the simulation of ESR spectra measured in ionic liquids. Those are asymmetric because of the high viscosity, which makes it impossible to simulate the spectra with other simpler programs.

The ESR- spectra measured in the solvent mixtures are simulated with a home written compute program developed by Stiegler [23]. The program yields in linewidths and rate constants.

4. Results

4.1 Self-exchange reaction of [TTF/TTF$^{\bullet+}$] in dependence of temperature

Temperature dependent ESR spectra were recorded for the self-exchange of TTF/TTF$^{\bullet+}$ in the ILs [emim$^+$][Tf_2N^-] and [bmim$^+$][Tf_2N^-] and the organic solvent dimethylphthalate (DMP). The shape on an ESR spectra changes with temperature and by increasing the concentration of the neutral redox partner TTF. Responsible for this event is the electron transfer between the charged radical and the neutral partner. The electron transfer is inhibited in the high-viscous ILs, but by increasing the temperature it is possible to observe the “slow exchange” region (Figure 4.1b) as well as the “intermediate” region (Figure 4.1c) and the “fast exchange” region (Figure 4.1d). In the IL [emim$^+$][Tf_2N^-] the fast exchange limit is reached at concentration of [TTF] = 27.9 mM and 358 K. The line broadening effect in [bmim$^+$][Tf_2N^-] is not as distinctive as in [emim$^+$][Tf_2N^-]. The reason for this is the higher viscosity and the lower temperature limit. Above 338 K the signal disappears because the radical decomposes. The maximum line broadening effect is reached at [TTF] = 20.0 mM and 338K (Figure 4.2 d). The line broadening in DMP as an example of high-viscous organic solvent reached the maximum broadening at 368 K and [TTF] = 14.1 mM in the fast exchange region.

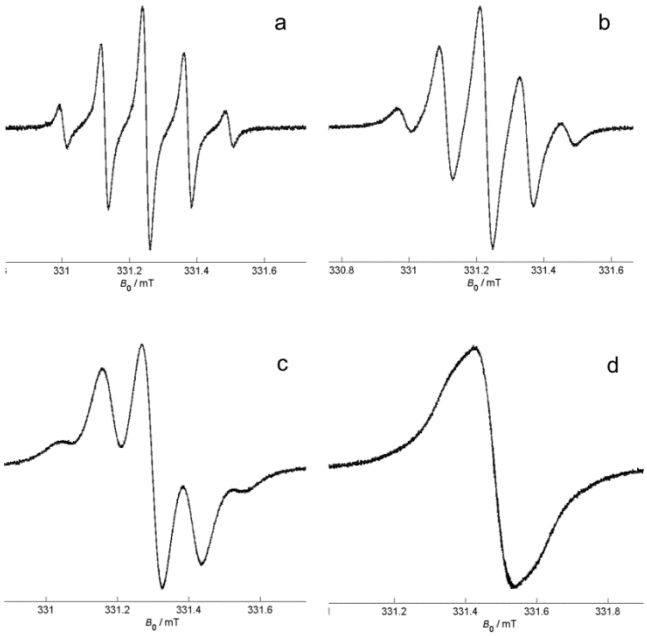

Figure 4.1: ESR spectra of 0.4 mM $TTF^{\cdot+}$ in $[emim^+][Tf_2N^-]$.with different concentrations of [TTF] at 358 K. (a) [TTF] = 0 mM, (b) [TTF] = 5.66 mM (c) [TTF] = 15.5 mM, (d) [TTF] = 27.9 mM

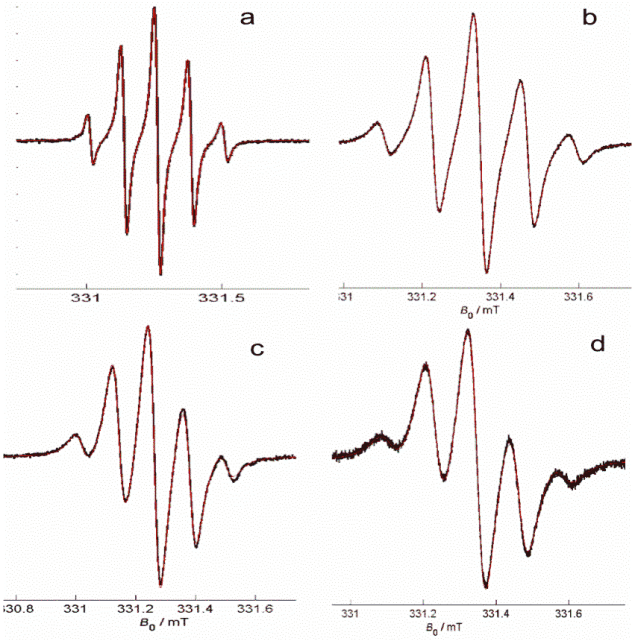

Figure 4.2: ESR spectra of 0.4 mM $TTF^{\cdot+}$ in $[bmim^+][Tf_2N^-]$.with different concentrations of [TTF] at 338 K. (a) [TTF] = 0 mM, (b) [TTF] = 7.08 mM (c) [TTF] = 13.8 mM, (d) [TTF] = 20.0 mM

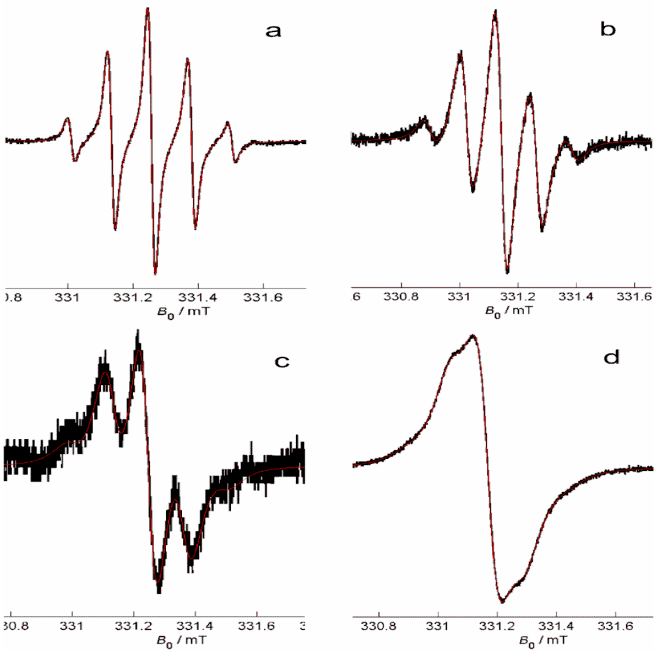

Figure 4.3: ESR spectra of 0.4 mM $TTF^{\cdot+}$ in DMP with different concentrations of [TTF] at 368 K. (a) [TTF] = 0 mM, (b) [TTF] = 4.19 mM (c) [TTF] = 8.42 mM, (d) [TTF] = 14.1 mM

The concentration dependences of the observed exchange rates are plotted in Figure 4.4 - Figure 4.6 for the different temperatures. The slopes of the very nice straight lines give the concentration independent rates constants of the self-exchange reaction [$TTF/TTF^{\bullet+}$] in three different solvents listed in Table 4-1 - Table 4-3.

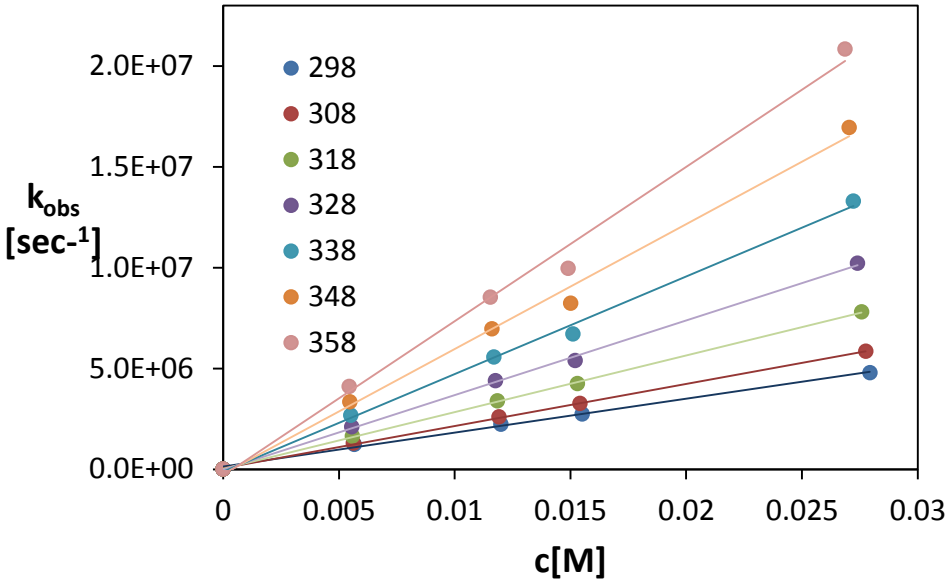

Figure 4.4: Temperature and concentration dependence of the exchange rate [TTF/$TTF^{\bullet+}$] in [$emim^+$][Tf_2N^-].

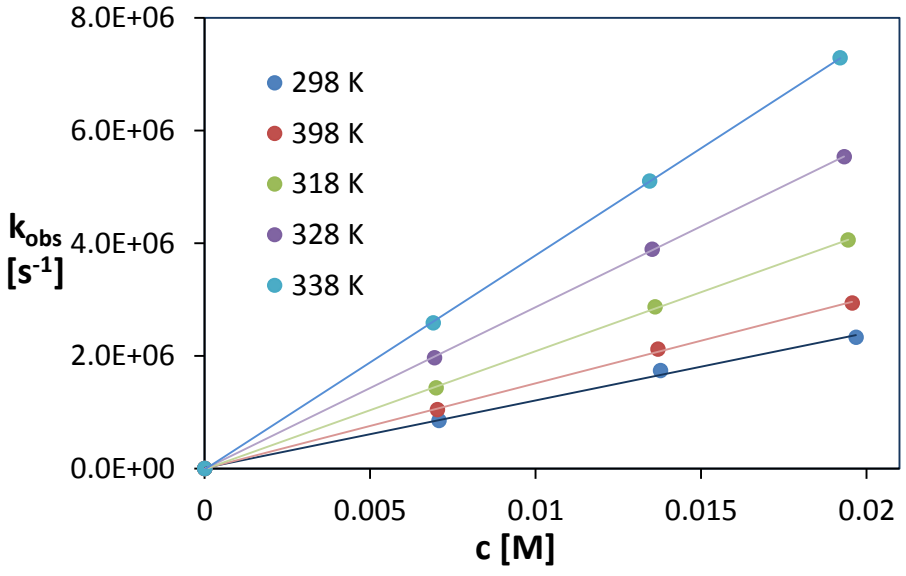

Figure 4.5: Temperature and concentration dependence of the exchange rate [TTF/$TTF^{\bullet+}$] in [$bmim^+$][Tf_2N^-].

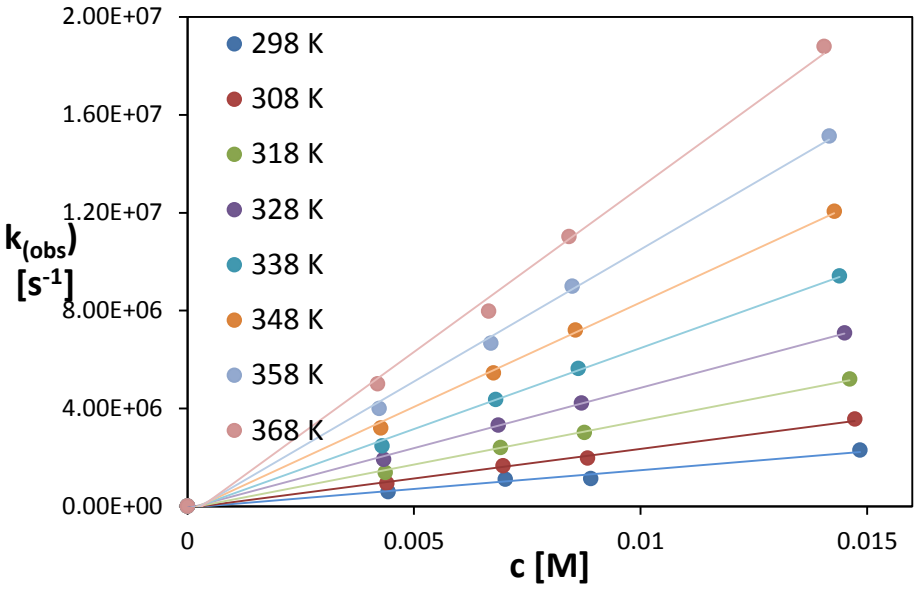

Figure 4.6: Temperature and concentration dependence of the exchange rate [TTF/TTF$^{\bullet+}$] in DMP.

Table 4-1: Rates for the self-exchange reaction of [TTF/TTF$^{\bullet+}$] in [emim^{+}][Tf_2N^{-}]. Observed rate constants k_{obs} and rates for diffusion k_{diff} calculated via equation (2.11) .

T [K]	k_{obs} [10^8 $M^{-1}s^{-1}$]	k_{diff} [10^8 $M^{-1}s^{-1}$]
298	1.68±0.06	2.01
308	2.09±0.03	2.92
318	2.81±0.03	4.05
328	3.70±0.07	5.45
338	4.8±0.2	6.94
348	6.2±0.3	8.91
358	7.7±0.4	11.0

Table 4-2: Rates for the self-exchange reaction of [TTF/TTF$^{\bullet+}$] in [bmim$^+$][Tf$_2$N$^-$]. Observed rate constants k_{obs} and rates for diffusion k_{diff} calculated via equation (2.11)

T [K]	k_{obs} [10^8 $M^{-1}s^{-1}$]	k_{diff} [10^8 $M^{-1}s^{-1}$]
298	1.20±0.04	1.28
308	1.51±0.03	1.98
318	2.09±0.02	2.90
328	2.87±0.01	4.06
338	3.80±0.02	5.48

Table 4-3: Rates for the self-exchange reaction of [TTF/TTF$^{\bullet+}$] in DMP in dependence of temperature. Observed rate constants k_{obs}, rates for diffusion k_{diff} (via equation (2.11)) and k_{et} (via equation (2.6))

T [K]	η [mPa s]	k_{obs} [10^8 $M^{-1}s^{-1}$]	k_{diff} [10^8 $M^{-1}s^{-1}$]	k_{et} [10^8 $M^{-1}s^{-1}$]
298	13.65	1.5±0.1	4.84	4.2±0.9
308	9.00	2.42±0.08	7.58	6.7±0.7
318	6.31	3.58±0.08	11.2	10.0±0.6
328	4.73	4.92±0.09	15.3	13.8±0.7
338	3.71	6.6±0.2	20.2	19±1
348	3.02	8.5±0.2	25.5	26±2
358	2.52	10.8±0.3	31.5	34±3
368	2.16	13.5±0.4	37.7	47±6

It is evident from the plots of ln(k_{obs}) vs. 1/T (Figure 4.7 - Figure 4.8) that the calculated rate constants of diffusion are so closed to the observed exchange rate constants that we can expect a diffusion controlled electron exchange mechanism. A correction via equation (2.6) would result in a negative value of k_{et}. In DMP, a highly viscous organic solvent, the observed rate constant is small enough (see Figure 4.9) to perform a diffusion correction via equation (2.6) and this leads to the electron transfer rates k_{et}. However, the rate constants of the electron transfer and the rate constants of the diffusion are almost identical (see Table 4-3). This indicates that the electron transfer reaction in DMP operates in a region between diffusion and kinetic control.

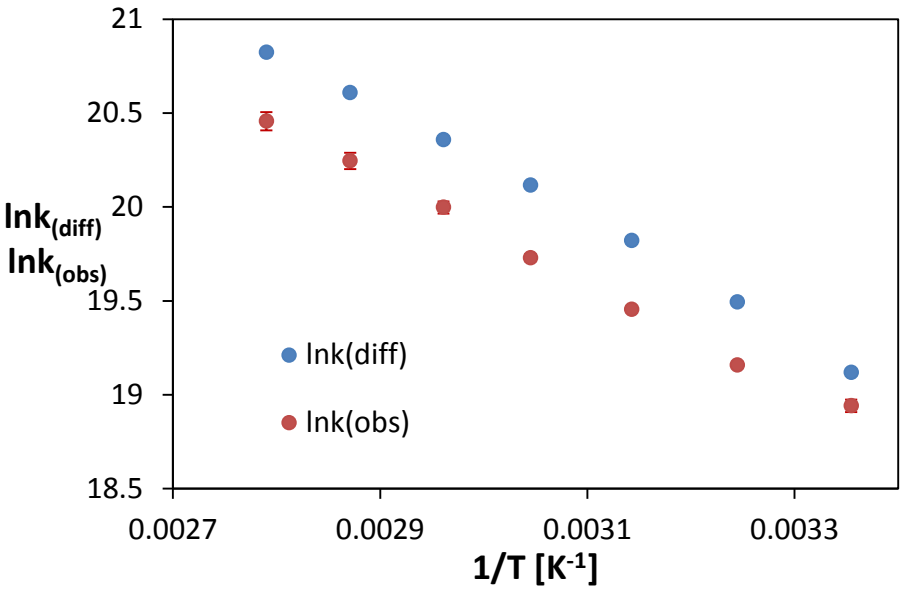

Figure 4.7: Temperature dependence of the experimental observed rate constant k_{obs} (•) and the calculated rate constants of diffusion k_{diff} (•) of the redox couple [TTF/$TTF^{\bullet+}$] in [$emim^+$][Tf_2N^-].

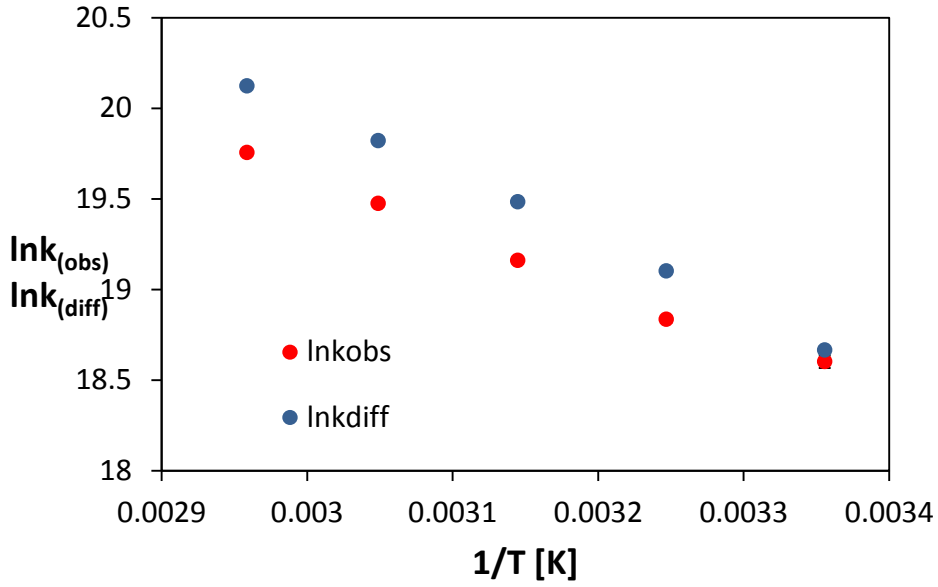

Figure 4.8: Temperature dependence of the experimental observed rate constant k_{obs} (•) and the calculated rate constants of diffusion k_{diff} (•) of the redox couple [TTF/$TTF^{\bullet+}$] in [$bmim^+$][Tf_2N^-].

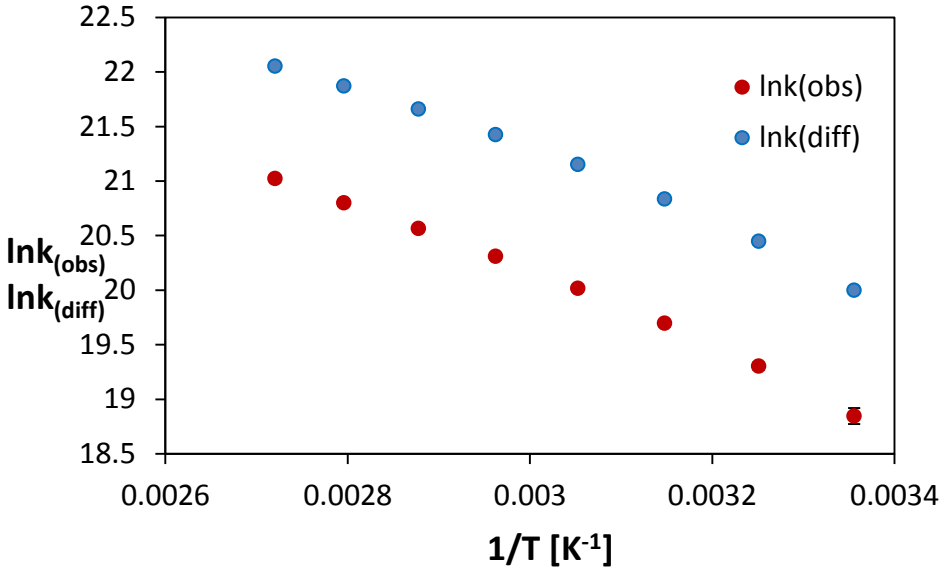

Figure 4.9: Temperature dependence of the experimental observed rate constant k_{obs} (●) and the calculated rate constants of diffusion k_{diff} (●) of the redox couple [TTF/$TTF^{\bullet+}$] in DMP.

4.1.1 Activation energies / Discussion

Arrhenius plots of ln(k_{obs}) versus 1/T for the ILs and ln(k_{et}) versus 1/T for DMP gave the corresponding activation energies from the temperature dependent rate constants. Plots are shown in Figure 4.7 and Figure 4.8 for the ILs and in Figure 4.10 for the DMP. The resulting activation energies are listed in Table 4-4.

Table 4-4: Activation energies obtained from Arrhenius plots.

solvent	E_a [kJ mol^{-1}]	H_η [kJ mol^{-1}]	Temperature range [K]
[$bmim^+$][Tf_2N^-]	25±1[(a)]	27.3±0.7	298 - 338
[$emim^+$][Tf_2N^-]	23.0±0.5[(a)]	22.3±0.5	298 – 358
Dimethylphthalate	31.0±0.5[(b)]	24±1	298 - 368

Note: E_a= Activation energy: ln k = const.-E_a/RT

H_η from ln η = const + H_η/RT

[(a)] from ln k_{obs}=ln A – E_a/RT (Figure 4.8 and Figure 4.7)

[(b)] from ln k_{et}=ln A – E_a/RT (Figure 4.10)

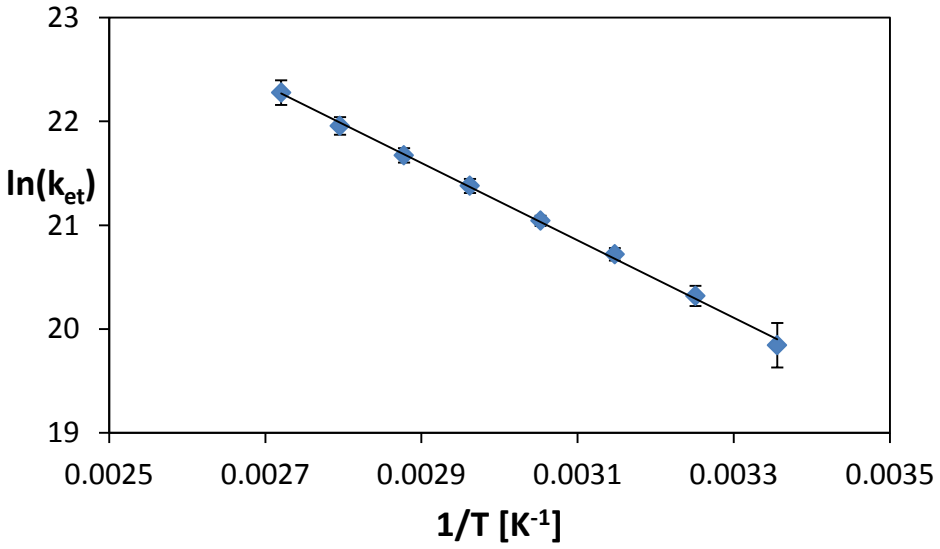

Figure 4.10: Arrhenius plots of $\ln(k_{et})$ versus 1/T for DMP.

The electron transfer of the redox couple [TTF/$TTF^{\bullet+}$] is controlled by adiabatic solvent dynamics in several organic solvents as published by Grampp and Jaenicke[20]. The activation energy is according to the authors composed of two terms [20].

$$E_a = \Delta G^*_{exp} + H_L \qquad (4.1)$$

Here, H_L the longitudinal relaxation energy is obtained from $\ln\tau_L = \ln b + H_L/RT$. Because of the lack of temperature dependent dielectric data for DMP the approximation $H_L \approx H_\eta$ was used whereas the viscosity energy H_η is obtained from $\ln\eta = \text{const} + H_\eta/RT$.

Table 4-5: Reorganization energies and free Gibbs energies for the redox couple [TTF/$TTF^{\bullet+}$] in DMP

λ_o [a] [kJ mol^{-1}]	λ_i [kJ mol^{-1}]	ΔG^*_{calc} [b] [kJ mol^{-1}]	ΔG^*_{exp} [kJ mol^{-1}]	$\lambda/4$ [c] [kJ mol^{-1}]
14.5	17[20]	3.88	7.2±1.5	7.88

[a]…calculated via equation (2.21), [b]…calculated via equation (2.15), used V_{RP}=4.0 kJ/mol[20], [c]…calculated via equation (2.27)

As can be seen in the table above are the obtained ΔG^*_{exp} for the electron transfer in DMP almost twice as high than expected from the calculated ΔG^*_{calc}. A comparison of the experimental value to the $\lambda/4$ shows that it seems to be, that the used V_{RP} is a bit overestimated. Other reasons for the disagreement with the calculated values could be that possibly the reaction distance in the high viscous solvent is larger so that the coupling is not as strong as predicted. This assumption was confirmed by Rosokha and Kochi [61] who found a very high resonance splitting energy of 19 kJ mol^{-1} in the low viscous solvent CH_2Cl_2. Furthermore an error from the estimation $H_L \approx H_\eta$ may arise. The activation energies in the two ILs are close to the activation energies for viscosity, what is expected because of the diffusion controlled reactions.

4.2 Pressure dependence of the self-exchange reaction of [TTF/$TTF^{\bullet+}$]

The self-exchange of the redox couple [TTF/$TTF^{\bullet+}$] was investigated on temperature dependence in two different ILs, [$emim^+$][Tf_2N^-] and [$bmim^+$][Tf_2N^-] and two organic solvents, dimethylphthalate (DMP) and acetonitrile (AN). A few recorded spectra are presented below.

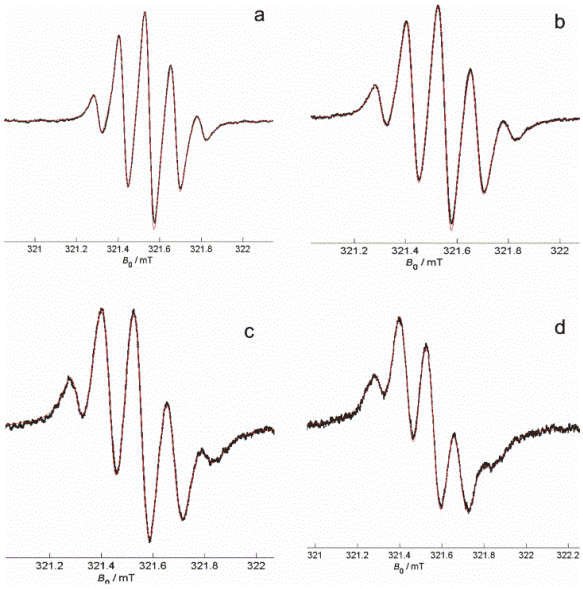

Figure 4.11: ESR spectra of 0.4 mM $TTF^{\bullet+}$ in [$emim^+$][Tf_2N^-] at different pressures at 296 K. (a) 0.1 MPa, (b) 30 MPa, (c) 70 MPa, (d) 100 MPa.

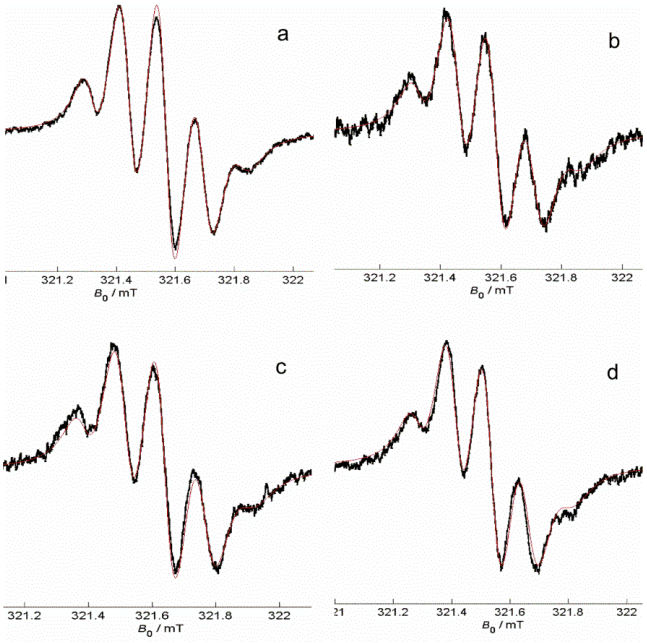

Figure 4.12: ESR spectra of 0.4 mM $TTF^{\bullet+}$ in [$bmim^{+}$][Tf_2N^{-}] at 296 K and 30 MPa. (a) [TTF] = 0 mM, (b) [TTF] = 3.0 mM (c) [TTF] = 6.7 mM, (d) [TTF] = 10.1 mM.

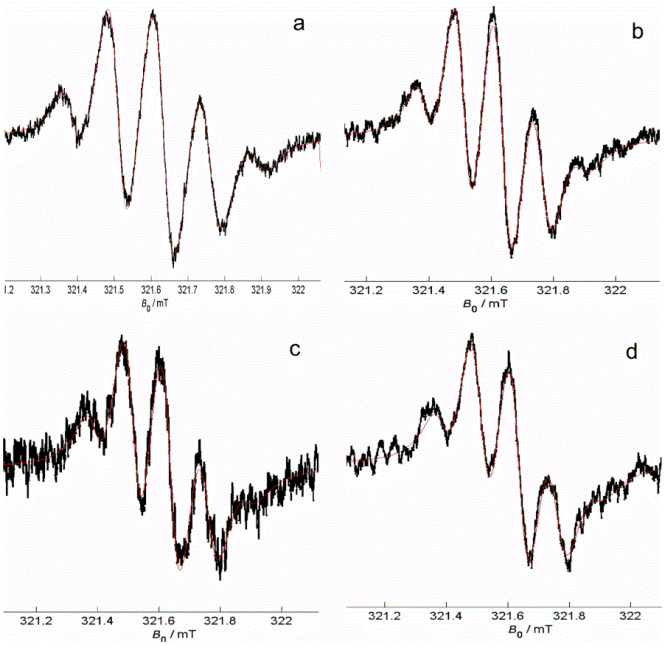

Figure 4.13: ESR spectra of 0.4 mM $TTF^{\bullet+}$ in DMP at 296 K and 50 MPa. (a) [TTF] = 0 mM, (b) [TTF] = 4.19 mM (c) [TTF] = 8.42 mM, (d) [TTF] = 14.0 mM.

The pressure dependence of the line broadening effect is not as distinctive as the temperature dependence. Figure 4.11 presents the line broadening of a radical solution of 0.4 mM $TTF^{+\cdot}$ in dependence on pressure. The broadening of the lines in Figure 4.11 is only due to the increasing viscosity caused by increasing pressure. The line broadening effect at elevated pressure in dependence on concentration is presented in Figure 4.12 - Figure 4.13. The red lines in the figures are the simulated spectra and black ones are the experimental spectra. The observed rate constants k_{obs}, from the simulation, are plotted against the concentration for each pressure. It is apparent from the following plots that the points are spread out. This difference in comparison to the temperature dependent experiments can first of all be attributed to the ESR cell. The bent capillary has a lot of air cavities between the single strings (see chapter 3.3.2) which leads to a higher signal to noise ratio.

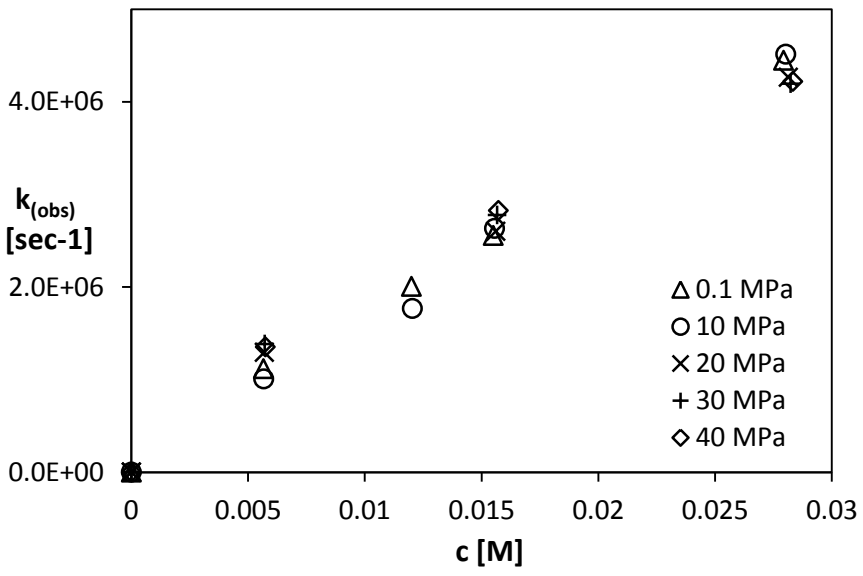

Figure 4.14: Pressure (0.1 – 40 MPa) and concentration dependence of the exchange rate [$TTF/TTF^{\bullet+}$] in [$emim^{+}$][Tf_2N^{-}].

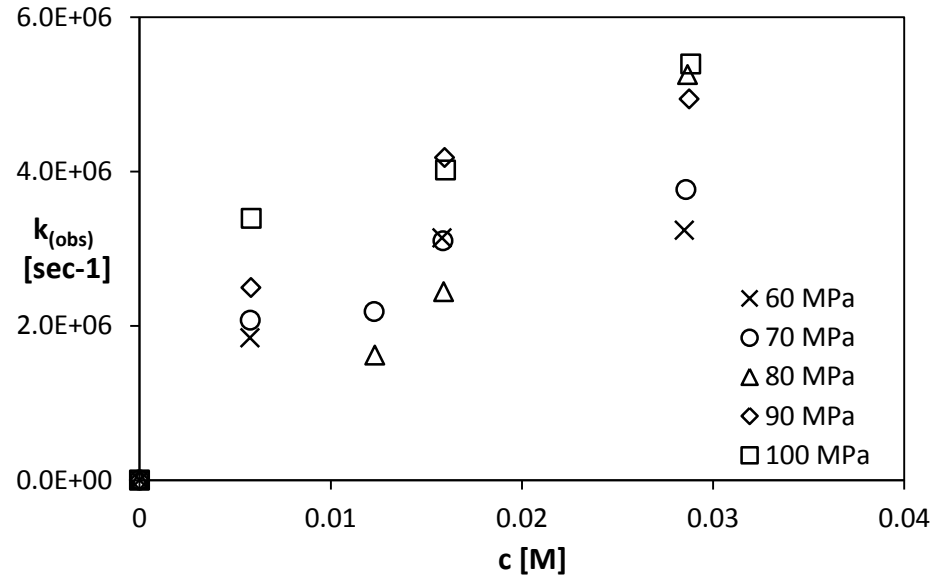

Figure 4.15: Pressure (60 – 100 MPa) and concentration dependence of the exchange rate [TTF/$TTF^{\bullet+}$] in [$emim^+$][Tf_2N^-].

The spreading of the points at higher pressures is more distinctive than at lower pressures. This leads to errors below 10% for until 40 MPa and up to 30% for the higher pressures for the bimolecular rate constants received from the slopes. All results are listed in Table 4-6.

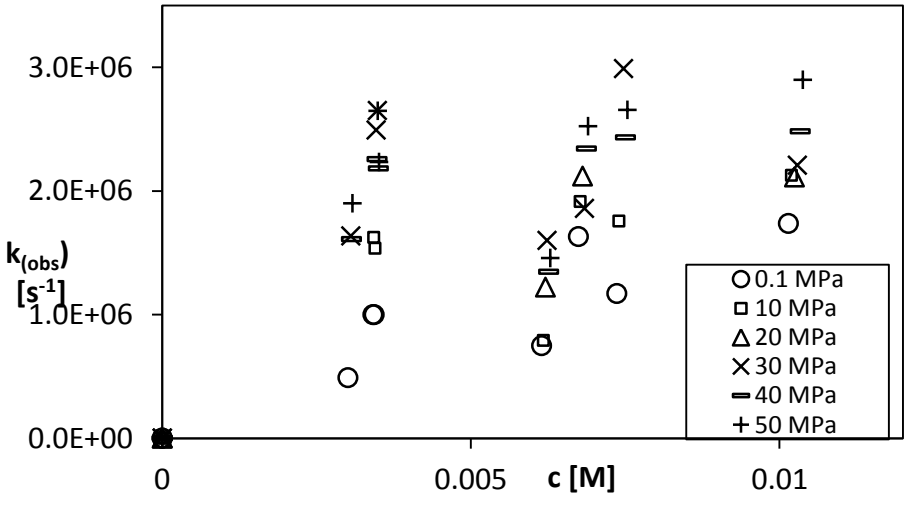

Figure 4.16: Pressure (0.1 - 50 MPa) and concentration dependence of the exchange rate [TTF/$TTF^{\bullet+}$] in [$bmim^+$][Tf_2N^-].

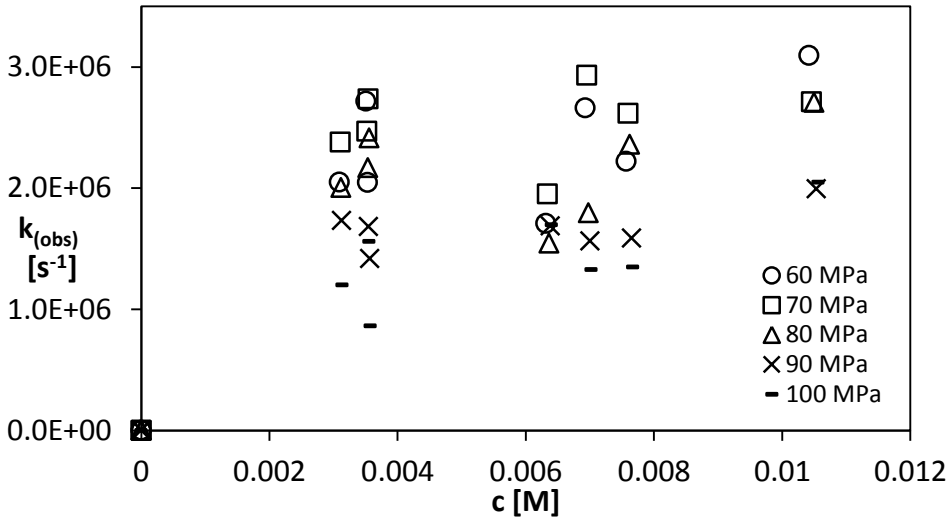

Figure 4.17: Pressure (60-100 MPa) and concentration dependence of the exchange rate [TTF/$TTF^{\bullet+}$] in [$bmim^+$][Tf_2N^-].

The measurements in [$bmim^+$][Tf_2N^-] resulted in the largest spreading within the high pressure series. Although many points were measured, the slopes lead to rate constants with errors around 30% and more (see Table 4-6). The reproducibility of several points was not good, which leads to the assumption that the pressure increasing rate plays an important role, as shall be discussed later.

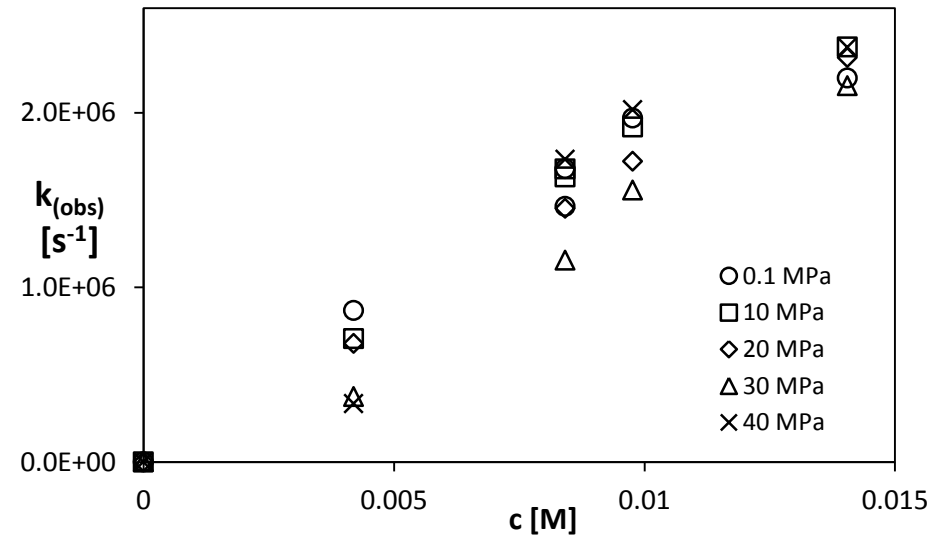

Figure 4.18:Pressure(0.1 – 40 MPa) and concentration dependence of the exchange rate [TTF/$TTF^{\bullet+}$] in DMP.

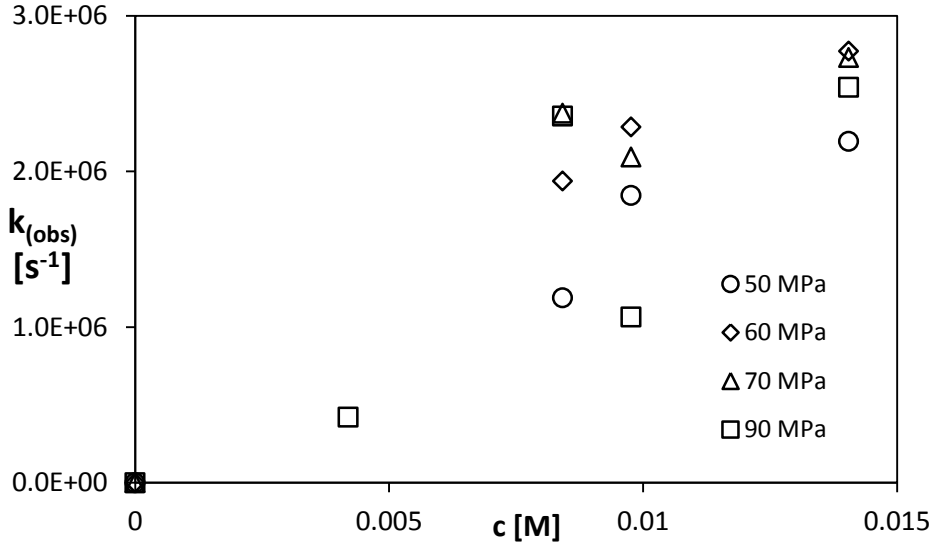

Figure 4.19: Pressure(50 – 90 MPa) and concentration dependence of the exchange rate [TTF/TTF$^{\bullet+}$] in DMP.

The high pressure ESR experiments in the organic solvent DMP lead to rate constants listed in Table 4-7 with errors below 20 % except for the measurements at 70 and 90 MPa.

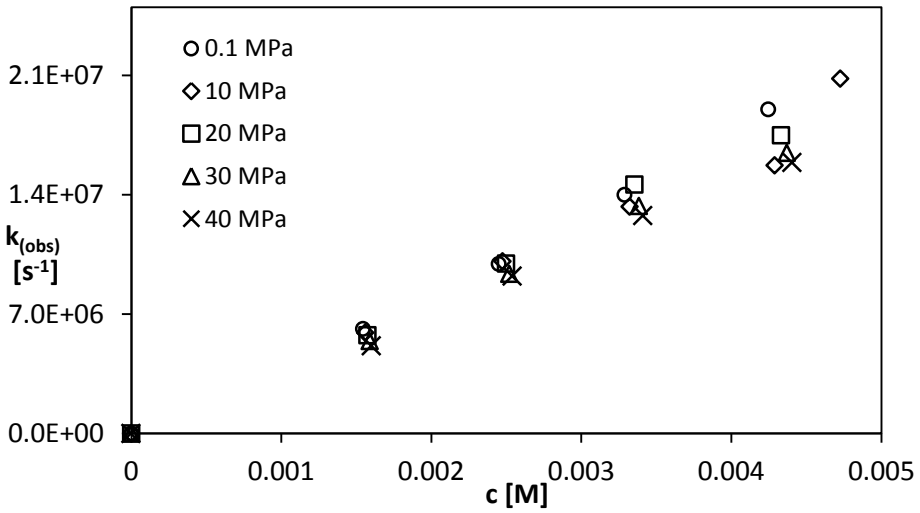

Figure 4.20: Pressure (0.1-40 MPa) and concentration dependence of the exchange rate [TTF/TTF$^{\bullet+}$] in AN.

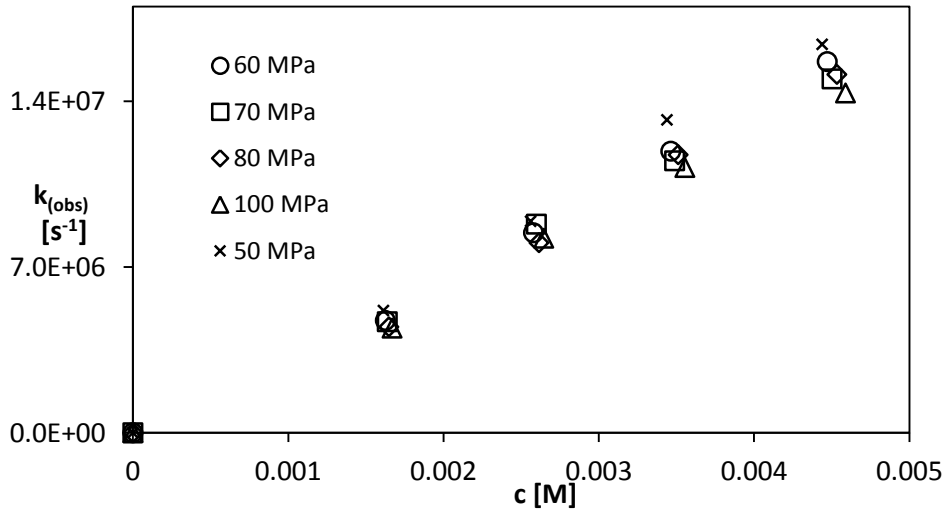

Figure 4.21: Pressure (0.1-40 MPa) and concentration dependence of the exchange rate [TTF/TTF$^{\bullet+}$] in AN.

Measurements of the self-exchange reaction of [TTF/TTF$^{\bullet+}$] in the low-viscous solvent acetonitrile are done to compare with the high viscous solvents. The points lead to nice straight lines and provide rate constants with an error below 5 % (see Table 4-7). Temperature dependent measurements were also done, but the system is not stable at higher temperatures in AN so that the results could not be used for further calculations. However, in the pressure dependent experiments there was no evidence of any problem with the stability of the substance.

Table 4-6: Rates for the self-exchange reaction of [TTF/TTF$^{\bullet+}$] in [emim$^+$][Tf$_2$N$^-$] and [bmim$^+$][Tf$_2$N$^-$] in dependence of pressure at 296 K. Observed rate constants k_{obs} and rates for diffusion k_{diff} (equation (2.11)).

P [MPa]	[emim$^+$][Tf$_2$N$^-$]			[bmim$^+$][Tf$_2$N$^-$]		
	η [mPa s]	k_{obs} [10^7 M^{-1}s^{-1}]	k_{diff} [10^7 M^{-1}s^{-1}]	η [mPa s]	k_{obs} [10^7 M^{-1}s^{-1}]	k_{diff} [10^7 M^{-1}s^{-1}]
0.1	36.75	15.7±0.5	18.0	56.06	17±3	11.8
10	41.19	16.1±0.6	16.0	63.24	21±6	10.4
20	46.16	15.1±0.9	14.3	71.42	20±7	9.25
30	51.67	15±1	12.8	80.66	22±9	8.19
40	57.77	15±1	11.4	91.09	23±7	7.25
50	64.51	16±3	10.2	102.87	26±7	6.42
60	-	-	-	116.18	26±7	5.69
70	80.16	17±5	82.4	131.21	25±8	5.04
80	89.20	18±1	74.1	148.19	22±7	4.46
90	99.16	17±4	66.6	167.36	17±5	3.95
100	110.10	18±5	60.0	189.01	16±4	3.50

Table 4-7: Rates for the self-exchange reaction of [TTF/TTF$^{\bullet+}$] in DMP and AN in dependence of pressure at 296 K. Observed rate constants k_{obs} ,electron transfer rates k_{et} (via equation (2.8)) and rates for diffusion k_{diff} (via equation (2.11)).

P [MPa]	DMP	AN			
	k_{obs} [10^7 M^{-1}s^{-1}]	η [mPa s]	k_{obs} [10^8 M^{-1}s^{-1}]	k_{diff} [10^8 M^{-1}s^{-1}]	k_{et} [10^8 M^{-1}s^{-1}]
0.1	16±2	0.36	44±1	186	83±5
10	18±1	0.38	41±2	175	77±8
20	16.8±0.5	0.40	42±2	165	84±8
30	16±1	0.42	39±1	156	76±5
40	19±3	0.44	37±1	148	73±5
50	18±3	0.47	38±2	141	81±8
60	23±5	0.49	35±1	135	74±6
70	23±6	0.51	34±1	129	70±5
80		0.53	34±2	124	75±8
90	18±6	0.56	33±1	119	73±7
100		0.58	32±1	114	72±6

The in listed rate constants k_{obs} Table 4-6 and Table 4-7 are plotted together with the calculated rate constants of diffusion in the following figures.

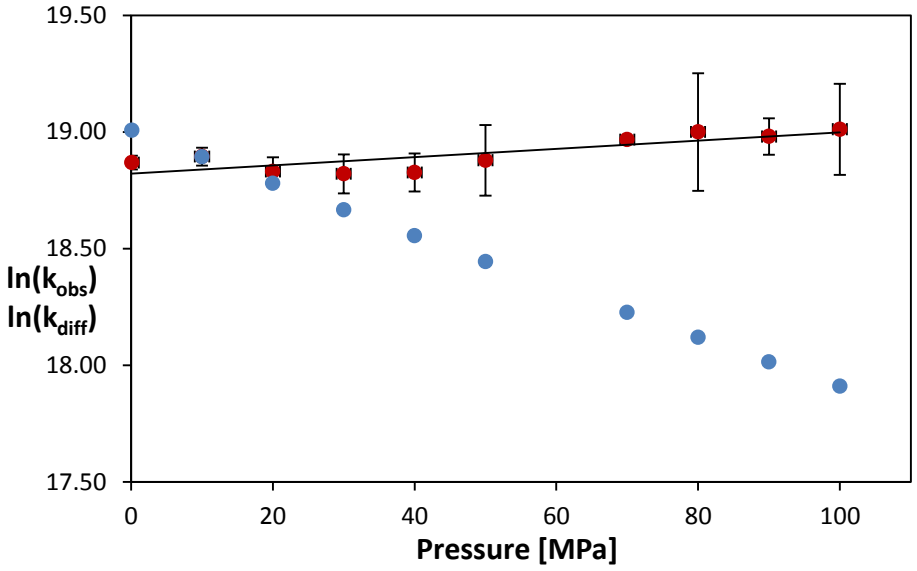

Figure 4.22: Pressure dependence of the experimental observed rate constant k_{obs} (•) and the calculated rate constants of diffusion k_{diff} (•) of the redox couple [TTF/TTF$^{\bullet+}$] in [emim$^+$][Tf_2N^-] at 296 K .

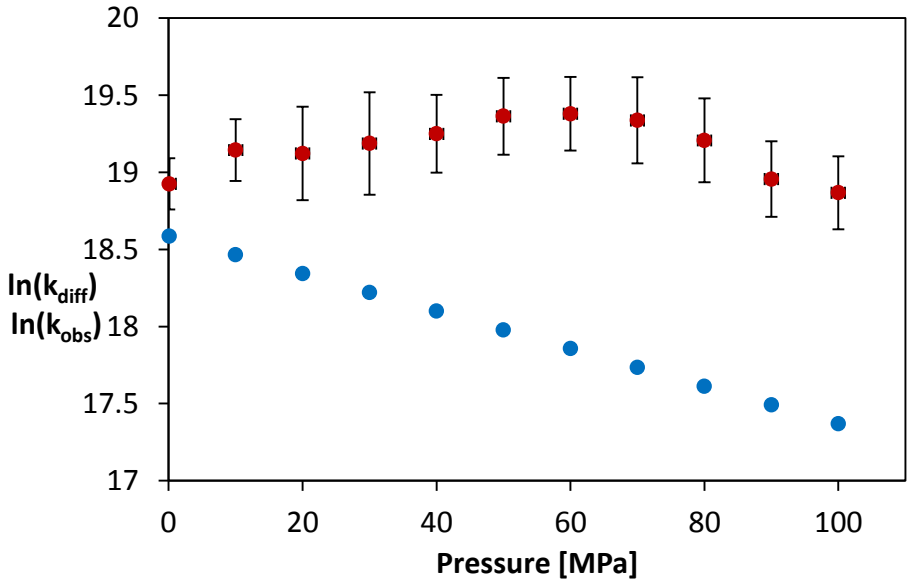

Figure 4.23: Pressure dependence of the experimental observed rate constant k_{obs} (•) and the calculated rate constants of diffusion k_{diff} (•) of the redox couple [TTF/TTF$^{\bullet+}$] in [bmim$^+$][Tf_2N^-] at 296 K .

Figure 4.22 and Figure 4.23 clearly show that the observed rate constants are higher than expected from the observed diffusion control in the temperature dependent experiments. Figure 4.22 shows nicely that it seems to be that until 20 MPa the diffusion control, observed by the temperature experiments, can be observed as well but from that point on the observed rate constants deviate from the calculated rate constants of diffusion. This indicates that upon reaching a certain viscosity a breakdown of the diffusion model or possibly a break of the diffusion per se occurs, something which will be discussed in more detail later.

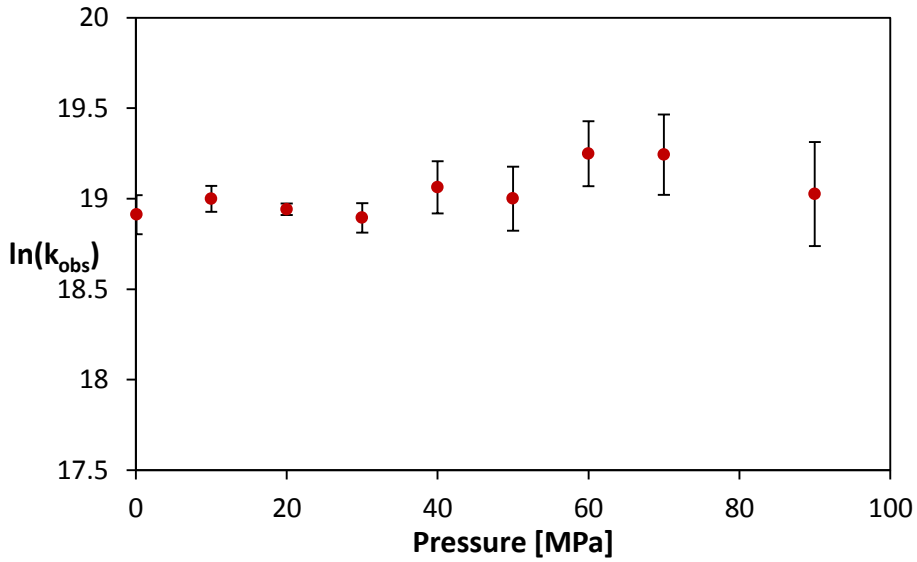

Figure 4.24: Pressure dependence of the experimental observed rate constant k_{obs} (•) of the redox couple [TTF/$TTF^{\bullet+}$] in DMP at 296 K .

The difference between the calculated rate constants of diffusion and the observed rate constants in acetonitrile is large enough to perform the diffusion correction via equation (2.11). The rate constants k_{et} obtained are listed in Table 4-7.

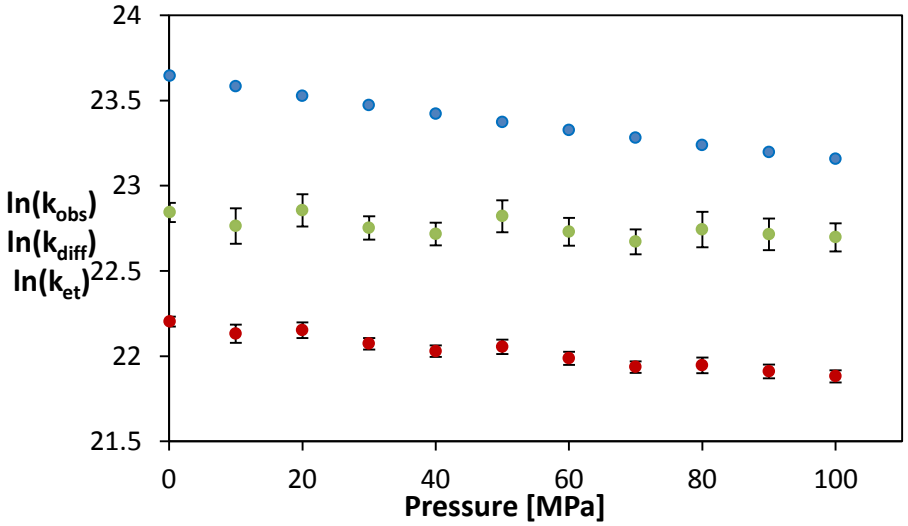

Figure 4.25: Pressure dependence of the experimental observed rate constant k_{obs} (•), the calculated rate constants of diffusion k_{diff} (•) and the rates for the electron transfer k_{et} (•) of the redox couple [TTF/TTF$^{\bullet+}$] in AN at 296 K .

4.2.1 Activation volume / Discussion

From the plot ln(k_{et}) vs. p in Figure 4.25 and from the resulting slope, the activation volume $\Delta V_{et}^{\ddagger}$ could be calculated using equation (2.46). The observed activation volumes $\Delta V_{obs}^{\ddagger}$ for the redox couple [TTF/TTF$^{\cdot+}$] in [emim$^+$][Tf_2N^-], [bmim$^+$][Tf_2N^-] and DMP were obtained from the slopes in Figure 4.22 - Figure 4.24 and listed in Table 4-8.

Table 4-8: Activation volumes obtained from the plots ln(k_{obs}) vs. p and ln(k_{et}) vs. p.

solvent	$\Delta V_{diff}^{\ddagger}$ [cm^3 mol^{-1}]	$\Delta V_{obs}^{\ddagger}$ [cm^3 mol^{-1}]	$\Delta V_{et}^{\ddagger}$ [cm^3 mol^{-1}]	Pressure range [MPa]
[bmim$^+$][Tf_2N^-]	30.1	-10 ±3		0.1-80
[emim$^+$][Tf_2N^-]	27.2	-4±1		0.1-100
dimethylphthalate	-	-11±3		0.1-70
acetonitrile	12	7.7±0.6	3±1	0.1-100

Figure 4.22 and Figure 4.23 show that the observed rates are higher than predicted from the calculated rate constants for diffusion. This leads to the assumption that the diffusion model is no longer valid or that no diffusion happens at such high viscosities. This in turn would mean that the observed k_{obs} is expected to be k_{ex}. The formation of a strong solvent cage around the redox couple would be possible. Strehmel et al published rates of the lophyl radical dimerization [3, 64] in ILs and reporting also higher rates in higher viscous ILs as expected. This fits to the present results and affirmed the assumption that the electron transfer reaction occurs within a solvent cage. This would mean that no diffusion occurs and the redox couple is captured within the solvent cage. It is known from literature [9, 25] that ILs have an organized local structure as well in the solid phase as in the liquid phase, containing free space within the alternating pattern of the ions. These spaces can act like a cage and host molecules, as reported by Castiglione[6]. By a ^{129}Xe chemical shift NMR-experiment, the authors could prove the cage-like structure in several ILs and conclude from the chemical shift to the cage size. The reported cage size of 9.2 Å in [$bmim^+$][Tf_2N^-] is in the region of the size of a [$TTF/TTF^{\bullet+}$] precursor complex dimension (given in Ref.[20] in approximation via an ellipsoid model). The melting points, T_m, for the solvents [$emim^+$][Tf_2N^-], [$bmim^+$][Tf_2N^-] and DMP at atmospheric pressure are relatively high (T_m: [$emim^+$] [Tf_2N^-], 256 K [16], [$bmim^+$][Tf_2N^-], 271 K [16] and DMP, 279 K [38]). Under the assumption that the melting points increase with increasing pressure it may be possible that the melting points are reached or at least the region around the points where the flexibility of ions in the ILs is reduced. A reduced flexibility of the ions in ILs could prevent the further diffusion of the reaction partners through the solution. The redox couples which are captured in the cages of the ILs still undergo electron transfer. This assumption could be a possible explanation for the worse reproducibility of the measured points at high pressures in the ionic liquids. It is thinkable that the rate of pressure increase during the measurements plays an important role. How fast the point is reached, from where the redox partner cannot diffuse anymore, decides how many redox couples are captured together in a solvent cage. Within this work the pressure increasing rate was not considered but it would make sense to consider it in the further work on in this field.

The calculation of the diffusion rates in DMP was not possible because of missing pressure dependent viscosity data. But, the observed activation volume of -10 cm^3mol^{-1} is in the same range like the activation volumes in [$bmim^+$][Tf_2N^-]. This could also be due to a present solvent cage in the DMP. DMP has the highest melting point within the measured solvents. It could be that the DMP reached its melting point by the increase in pressure and the redox couples are captured in the freezing structure of DMP.

In comparison to the experimental $\Delta V_{obs}^{\ddagger}$, the volume describing the compression of the ILs surrounding the [TTF/$TTF^{\bullet+}$] couple was calculated according to Swaddle [65](see equation (2.51)).This approach yielded values of -4 cm^3 mol^{-1} and -3 cm^3 mol^{-1} for [$emim^+$][Tf_2N^-], [$bmim^+$][Tf_2N^-], respectively. It appears that the negative experimentally determined activation volume $\Delta V_{obs}^{\ddagger}$ in the ILs simply reflects their compression.

The experimental activation volume for the redox couple [TTF/$TTF^{\bullet+}$] in the low-viscous organic solvent acetonitrile is found as 3 cm^3/mol. This is comparable to other organic redox couples in acetonitrile, like [DDQ/$DDQ^{\cdot-}$] and [TCNE/$TCNE^{\cdot-}$] (7,0 cm^3 $mol^{-1}$and 8,2 cm^3 mol^{-1})[57].

4.3 Self- exchange reaction of [TCNE/TCNE$^{\bullet-}$] in dependence of temperature

ESR line broadening experiments were carried out in four different ILs. Three of them are ILs with a bis(trifluoromethylsulfonyl)imide anion and variable sidechains on the methylimidazolium cation. Figure 4.26 shows the line broadening effect of the redox couple [TCNE/TCNE$^{\bullet-}$] at 333 K, where the spectrum of the single radical solution of TCNE$^{\bullet-}$ (a) shows nine very narrow lines. The lines get increasingly more broadened by increasing the concentration of [TCNE].

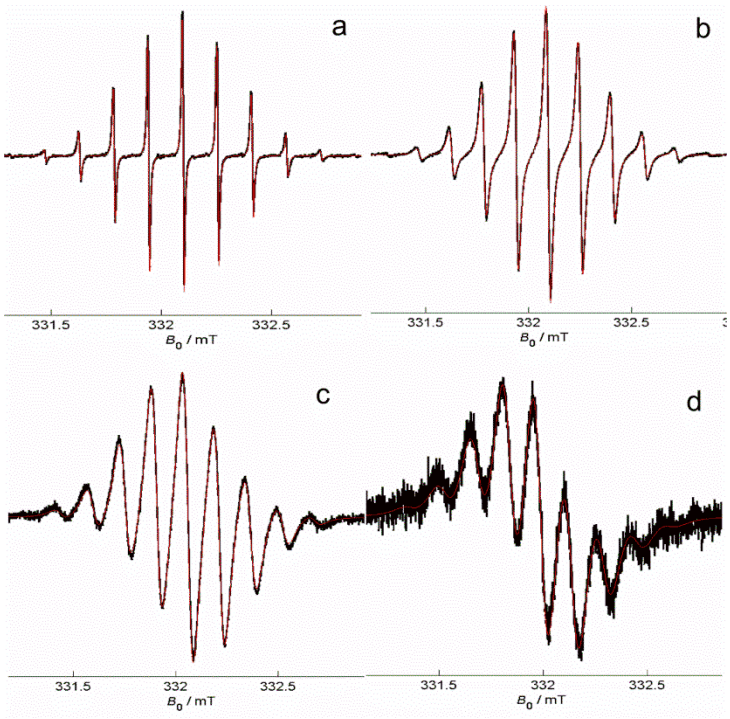

Figure 4.26: ESR spectra of 0.75 mM TCNE$^{\bullet-}$ in [emim$^+$][Tf$_2$N$^-$] at 333 K. (a) [TCNE] = 0 mM, (b) [TCNE] = 12 mM (c) [TCNE] = 40 mM, (d) [TCNE] = 68 mM.

Figure 4.27 shows the effect on the line width without electron exchange by increasing temperature. The lines get narrower by increasing the temperature due to the decreasing viscosity of the ILs.

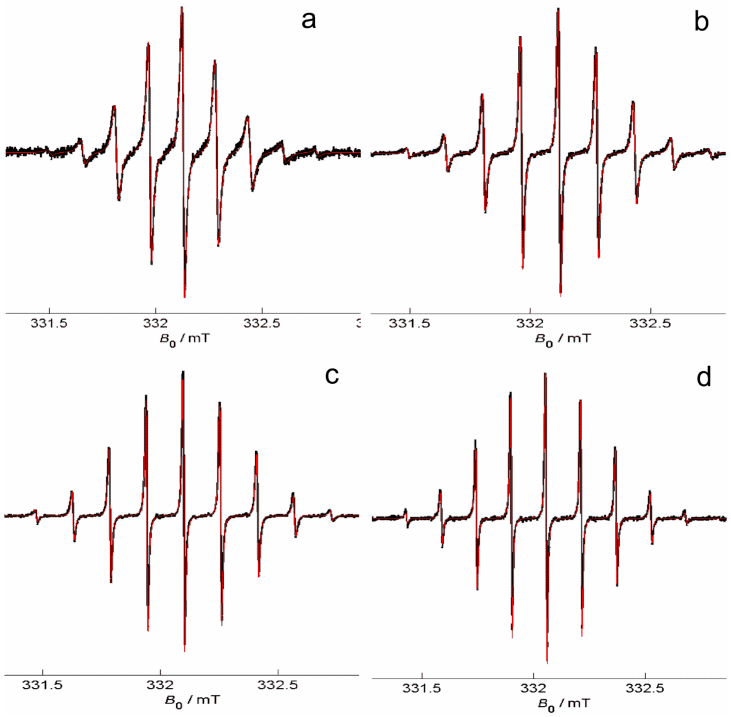

Figure 4.27: ESR spectra of 0.75 mM $TCNE^{\bullet-}$ in [$emim^+$][Tf_2N^-] at (a) 288 K, (b) 308 K (c) 333 K, (d) 358 K.

The rate constants received from the simulation are plotted vs. the concentration of neutral TCNE. Very linear straight lines are obtained in all measured ILs.

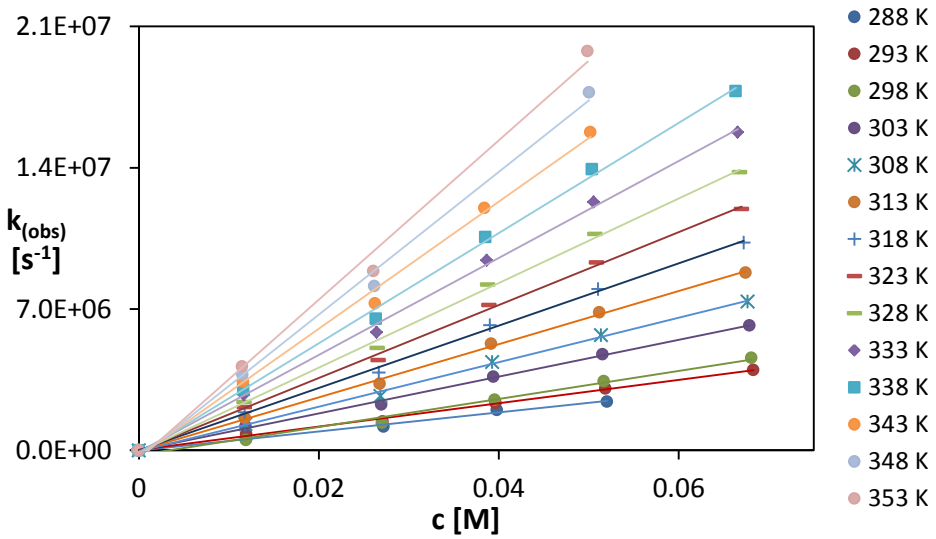

Figure 4.28: Temperature and concentration dependence of the exchange rate [TCNE/$TCNE^{\bullet-}$] in [$emim^+$][Tf_2N^-].

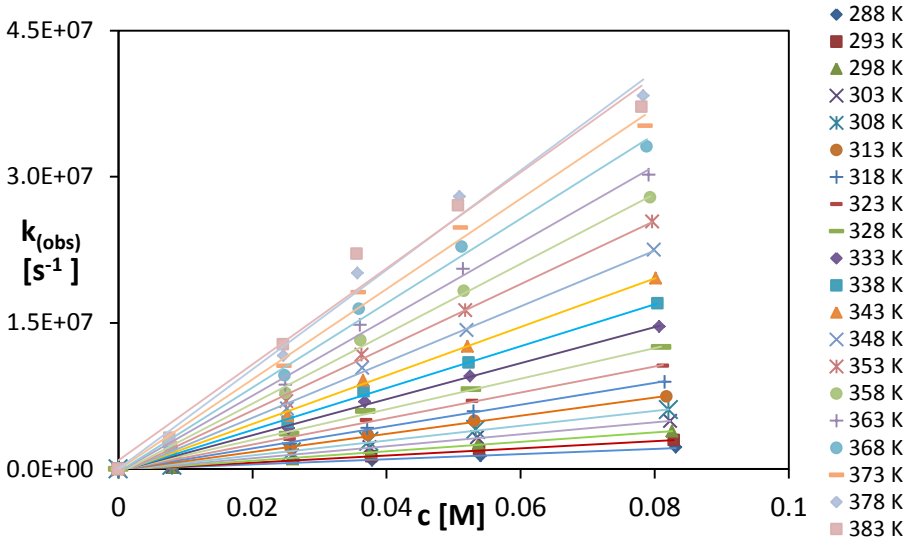

Figure 4.29: Temperature and concentration dependence of the exchange rate [TCNE/$TCNE^{\bullet-}$] in [$bmim^+$][Tf_2N^-].

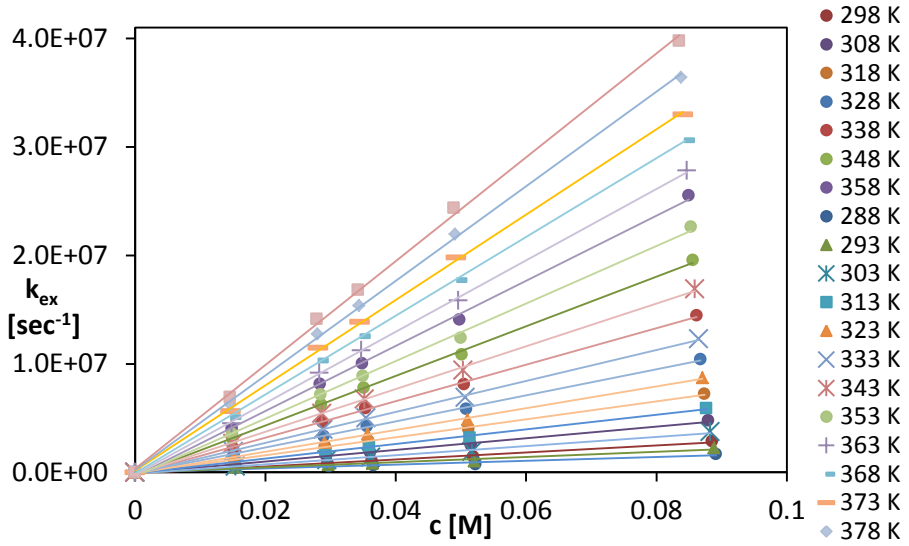

Figure 4.30: Temperature and concentration dependence of the exchange rate [TCNE/$TCNE^{\bullet-}$] in [$hmim^+$][Tf_2N^-].

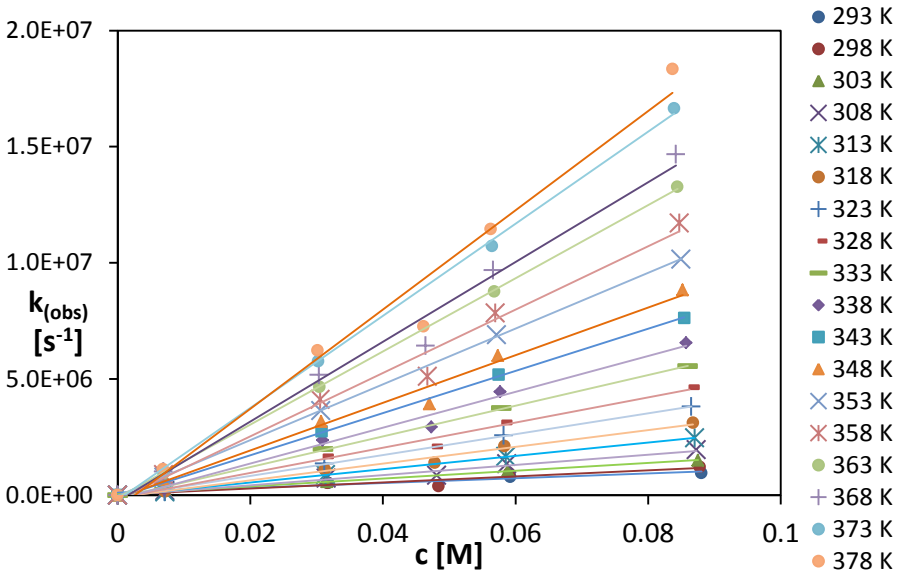

Figure 4.31: Temperature and concentration dependence of the exchange rate [TCNE/$TCNE^{\bullet-}$] in $[bmim^+][BF_4^-]$.

The slopes from Figure 4.28 to Figure 4.31 give the bimolecular rate constants k_{obs} which are listed together with the calculated rate constants for diffusion k_{diff} in Table 4-9 and Table 4-10. The electron transfer rate could be calculated for all measured ILs and are listed also in the tables mentioned before. For comparison of k_{obs}, k_{diff} and k_{et} all of them are plotted together in the following figures.

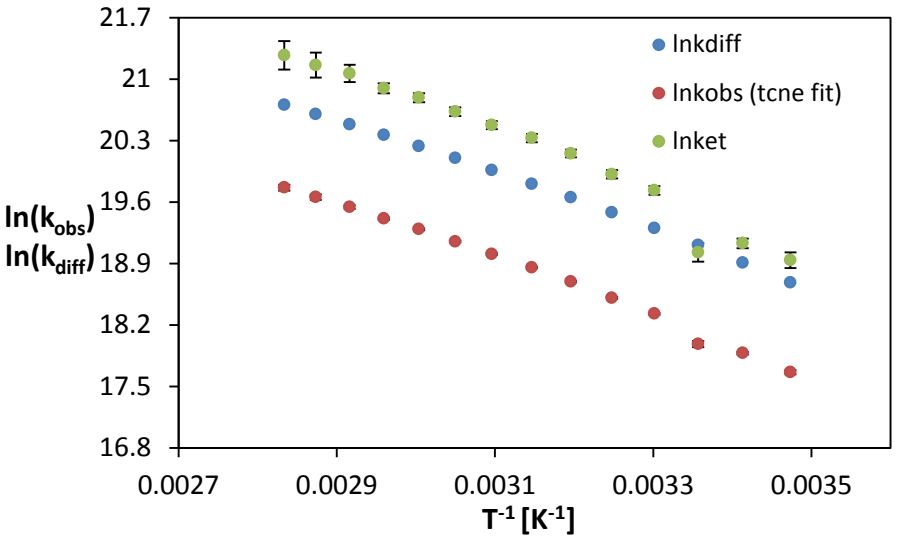

Figure 4.32: Temperature dependence of the experimental observed rate constant k_{obs} (•), the calculated rate constants of diffusion k_{diff} (•) and the rates for the electron transfer k_{et} (•) of the redox couple [TCNE/$TCNE^{\bullet-}$] in [$emim^+$][Tf_2N^-].

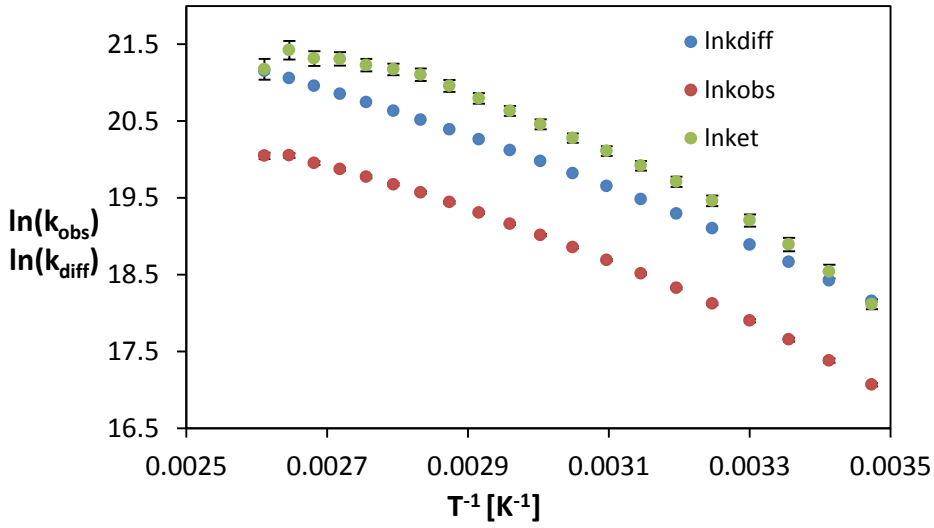

Figure 4.33: Temperature dependence of the experimental observed rate constant k_{obs} (•), the calculated rate constants of diffusion k_{diff} (•) and the rates for the electron transfer k_{et} (•) of the redox couple [TCNE/$TCNE^{\bullet-}$] in [$bmim^+$][Tf_2N^-].

Table 4-9: Rates for the self-exchange reaction of [TCNE/$TCNE^{\bullet-}$] in [$emim^+$][Tf_2N^-] and [$bmim^+$][Tf_2N^-] in dependence of temperature. Observed rate constants k_{obs} , electron transfer rates k_{et} (via equation (2.8)) and rates for diffusion k_{diff} (via equation (2.11)).

T [K]	[$emim^+$][Tf_2N^-]				[$bmim^+$][Tf_2N^-]			
	η [mPa s]	k_{obs} [10^7 $M^{-1}s^{-1}$]	k_{diff} [10^7 $M^{-1}s^{-1}$]	k_{et} [10^7 $M^{-1}s^{-1}$]	η [mPa s]	k_{obs} [10^7 $M^{-1}s^{-1}$]	k_{diff} [10^7 $M^{-1}s^{-1}$]	k_{et} [10^7 $M^{-1}s^{-1}$]
288	49.06	4.7±0.1	13.0	16.8±2	80.41	2.58±0.06	7.94	7.4±0.5
293	39.86	5.8±0.1	16.3	20.3±1	62.99	3.5±0.1	10.3	11±1
298	33.13	6.5±0.2	19.9	18.3±2	50.50	4.6±0.1	13.1	16±2
303	27.80	9.1±0.1	24.2	37.1±2	41.15	5.9±0.1	16.3	22±2
308	23.60	10.9±0.1	28.9	44.6±2	34.02	7.4±0.1	20.1	28±2
313	20.26	13.1±0.1	34.2	56.6±3	28.59	9.1±0.2	24.3	36±3
318	17.60	15.4±0.2	40.0	67.5±3	24.22	11.0±0.2	29.1	45±3
323	15.31	18.0±0.2	46.8	78.0±4	20.74	13.1±0.2	34.5	54±4
328	13.53	20.7±0.2	53.7	91.1±5	17.88	15.4±0.2	40.7	64±4
333	12.01	23.9±0.3	61.4	107±6	15.60	18.1±0.3	47.3	77±5
338	10.74	27.0±0.3	69.8	119±7	13.75	21.0±0.3	54.5	91±6
343	9.66	30.8±0.6	78.7	141±15	12.15	24.2±0.4	62.6	107±8
348	8.72	34±1	88.5	155±24	10.83	27.8±0.5	71.2	126±10
353	7.94	38±1	98.5	173±30	9.72	31.6±0.5	80.5	146±12
358					8.79	35.1±0.6	90.3	157±12
363					7.97	38.7±0.7	101	166±14
368					7.27	42.8±0.9	112	180±17
373					6.65	46±1	124	181±18
378					6.11	51±2	137	201±26
383					5.63	51±2	151	157±22

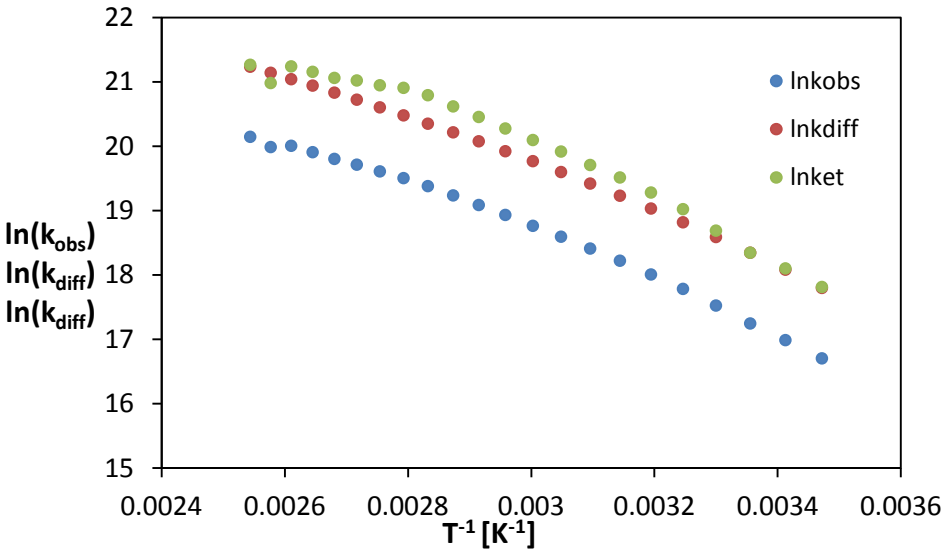

Figure 4.34: Temperature dependence of the experimental observed rate constant k_{obs} (•), the calculated rate constants of diffusion k_{diff} (•) and the rates for the electron transfer k_{et} (•) of the redox couple [TCNE/$TCNE^{\bullet-}$] in [$hmim^+$][Tf_2N^-].

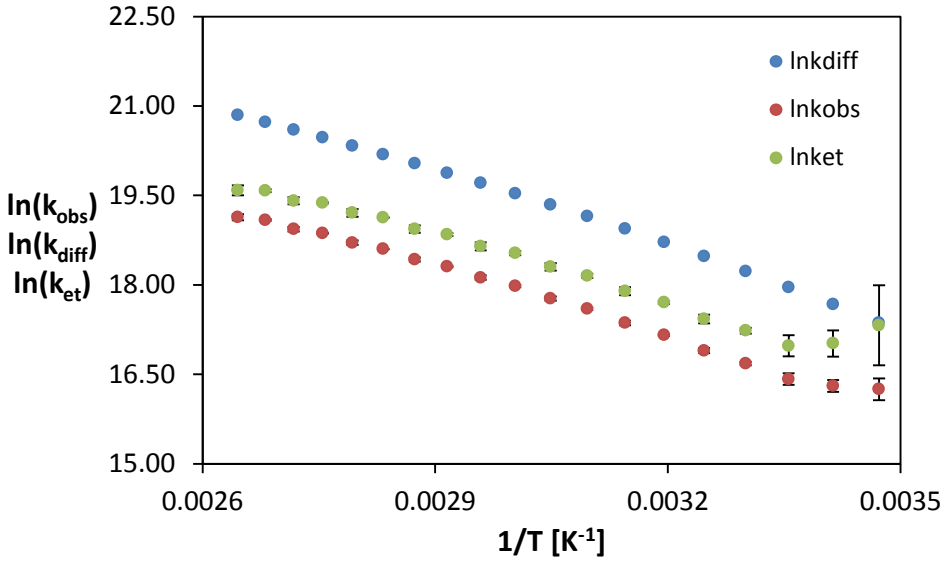

Figure 4.35: Temperature dependence of the experimental observed rate constant k_{obs} (•), the calculated rate constants of diffusion k_{diff} (•) and the rates for the electron transfer k_{et} (•) of the redox couple [TCNE/$TCNE^{\bullet-}$] in [$bmim^+$][BF_4^-].

Table 4-10: Rates for the self-exchange reaction of [TCNE/$TCNE^{\bullet-}$] in [$hmim^+$][Tf_2N^-] and [$bmim^+$][BF_4^-] in dependence of temperature. Observed rate constants k_{obs}, electron transfer rates k_{et} (via equation (2.8)) and rates for diffusion k_{diff} (via equation (2.11)).

T [K]	[$hmim^+$][Tf_2N^-]				[$bmim^+$][BF_4^-]			
	η [mPa s]	k_{obs} [10^7 $M^{-1}s^{-1}$]	k_{diff} [10^7 $M^{-1}s^{-1}$]	k_{et} [10^7 $M^{-1}s^{-1}$]	η [mPa s]	k_{obs} [10^7 $M^{-1}s^{-1}$]	k_{diff} [10^7 $M^{-1}s^{-1}$]	k_{et} [10^7 $M^{-1}s^{-1}$]
288	120.08	1.8±0.1	5.32	5±1	187.17	1.1±0.2	3.47	3±1
293	91.94	2.4±0.1	7.07	7±1	139.18	1.2±0.1	4.73	2.5±0.6
298	71.85	3.1±0.1	9.20	9±1	105.97	1.4±0.1	6.31	2.4±0.5
303	57.17	4.1±0.1	11.8	13±1	82.40	1.75±0.05	8.26	3.1±0.2
308	46.23	5.3±0.1	14.8	18±1	65.28	2.18±0.09	10.6	3.7±0.3
313	37.93	6.6±0.1	18.3	23±1	52.59	2.83±0.03	13.4	4.9±0.1
318	31.53	8.1±0.1	22.4	30±1	43.00	3.5±0.1	16.8	5.9±0.4
323	26.53	9.8±0.1	27.0	36±2	35.65	4.39±0.09	20.7	7.6±0.3
328	22.55	11.8±0.1	32.2	44±2	29.91	5.2±0.2	25.2	8.9±0.6
333	19.36	14.0±0.1	38.1	53±2	25.38	6.4±0.1	30.4	11.2±0.4
338	16.77	16.5±0.2	44.7	64±3	21.76	7.4±0.3	36.2	12.6±0.9
343	14.65	19.4±0.2	51.9	76±3	18.82	8.9±0.1	42.9	15.3±0.4
348	12.89	22.4±0.3	59.9	90±4	16.42	10.1±0.4	50.3	17±01
353	11.42	25.9±0.4	68.5	106±6	14.44	11.96±0.06	58.5	20±0.2
358	10.18	29.4±0.4	78.0	120±6	12.78	13.3±0.5	67.6	22±1
363	9.13	32.6±0.1	88.1	125±2	11.40	15.6±0.1	77.6	26.0±0.3
368	8.23	36.2±0.1	99.1	134±2	10.22	16.7±0.6	88.5	27±2
373	7.46	39.6±0.3	111	139±3	9.22	19.5±0.3	100	31.9±0.7
378	6.79	44.0±0.3	123	1534±	8.35	20±1	113	32±3
383	6.21	48.5±0.5	137	1676±				

4.3.1 Solvent dynamics

So-called Weaver plots [70, 71] were used to clarify whether this reaction shows a solvent dynamic effect as described in chapter 2.4. In organic solvents the self-exchange reaction of the [TCNE/$TCNE^{\bullet-}$] redox couple is controlled by adiabatic solvent dynamics as published by Grampp and Janicke [20]. To prove the solvent dynamic effect in the case of ionic liquids, plots were made according to equation (2.41), which should result in slopes of unity for the diabatic case and according to equation (2.42), which should result in slopes of unity for the adiabatic case. It is apparent from Table 4-11 that the difference between the ε_∞ and n_D^2 is significant. Therefore, for comparison, calculations of reorganization energies with experimental values of ε_∞ and with n_D^2 as an approximation are listed in Table 4-12.

Table 4-11: Square of the refractive indices n_D^2, dielectric parameters ε_∞ and ε_s and the relaxation times τ_L at 298 K for the listed ILs.

Solvent	n_D^2	ε_∞	ε_s	τ_L [ps]
[$emim^+$][Tf_2N^-]	2.02	3.23	12.25	58.92
[$hmim^+$][Tf_2N^-]	2.05	2.58	12.5	40.40
[$bmim^+$][Tf_2N^-]	2.04	3.03	11.52	112.12
[$bmim^+$][BF_4^-]	2.03	2.21	13.97	28.54

Table 4-12: Pekar factors γ and reorganization energies for the redox couple [TCNE/$TCNE^{\bullet-}$] in different ionic liquids

Solvent	γ(1)	γ(2)	$(\kappa_{el}\nu_n)_{obs}^{(1)}$ [$10^{10}s^{-1}$]	$(\kappa_{el}\nu_n)_{obs}^{(2)}$ [$10^{10}s^{-1}$]	$\Delta G^*_{calc}{}^{(1)}$ [kJ mol^{-1}]	$\Delta G^*_{calc}{}^{(2)}$ [kJ mol^{-1}]
[$emim^+$][Tf_2N^-]	0.228	0.413	1.62	19.4	11.10	17.26
[$hmim^+$][Tf_2N^-]	0.308	0.409	2.37	9.25	13.76	17.13
[$bmim^+$][Tf_2N^-]	0.243	0.404	1.74	1.52	11.61	16.98
[$bmim^+$][BF_4^-]	0.381	0.421	1.63	2.80	16.20	17.54

(1)…Pekar factor calculated via (2.22)

(2)…Pekar factor calculated via(2.22) using the approximation $1/\varepsilon_\infty \approx 1/n_D^2$

ΔG^*_{calc}… calculated via equation (2.15), used V_{RP}=4.7 kJ/mol[20]

The following double logarithmic plots according to Weaver use values from Table 4-12, once with the approximation $\varepsilon_\infty \approx n_D^2$ and once with the experimental ε_∞.

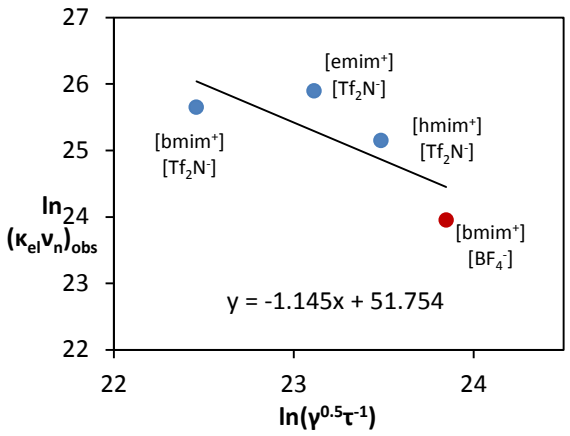

Figure 4.36: Weaver application for the adiabatic case by using n_D^2.

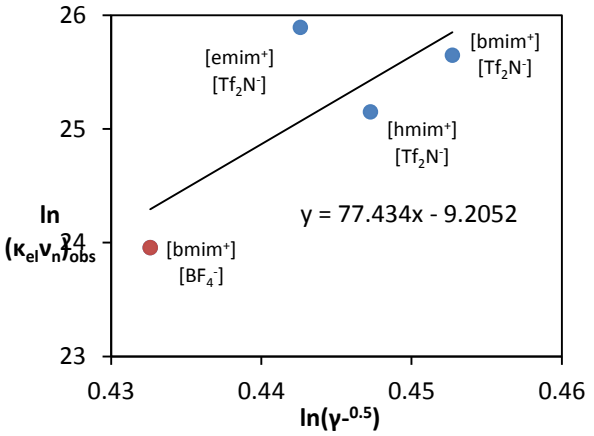

Figure 4.37: Weaver application for the diabatic case by using n_D^2.

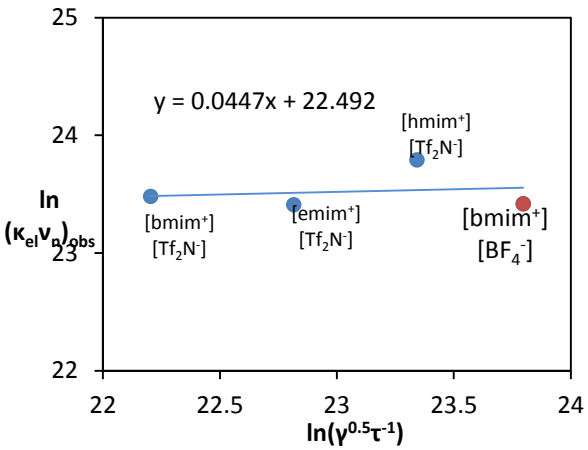

Figure 4.39: Weaver application for the adiabatic case by using ε_∞.

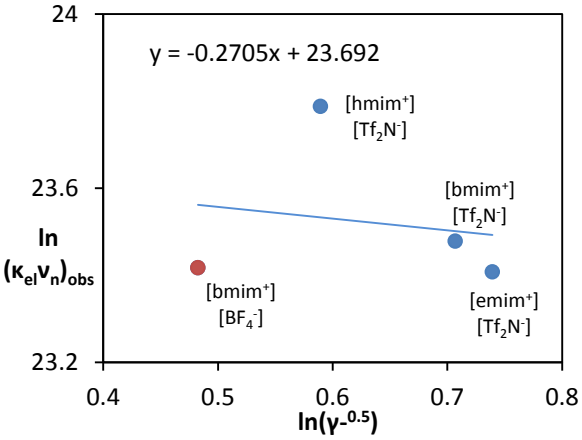

Figure 4.38: Weaver application for the diabatic case by using ε_∞.

It is obviously from Figure 4.36 -Figure 4.37 that both, the adiabatic and the diabatic application, do not result in a slope of unity. Why Weaver plots completely failed generates the perception that the approximation of $n_D^2 \approx \varepsilon_\infty$ is not effective for the investigated ionic liquids. But, the Weaver plots in Figure 4.38 and Figure 4.39, with Pekar factors calculated

from ε_∞ values, also failed. Is not really astonishing that the diabatic application failed because according to Grampp *et al.* [20] one would expect an adiabatic solvent dynamic effect for the self-exchange reaction of the redox couple [TCNE/TCNE$^{\bullet-}$]. The application for the adiabatic case in Figure 4.39 shows a more or less solvent independent trend. There are two possible explanations for that, one is that the application of a Pekar factor for ILs is questionable in general. Because ILs are composed of discrete charged parts and have no dipole moments like organic solvent molecules. Of course, the measurement of a dielectric constant is possible and values are available in literature, but the published dielectric constants for ILs are very different. And this could be another reason for the strange behaviour in Figure 4.39. The used dielectric constants are from different authors and especially the values available in literature for [emim$^+$][Tf_2N^-] and [bmim$^+$][Tf_2N^-] are very different. To exclude an error from using different sources of the dielectric parameters, a Weaver plot with temperature dependent dielectric parameters of [hmim$^+$][Tf_2N^-] and [bmim$^+$][BF_4^-] was made (see Figure 4.40). Values used for the plot below, are listed in Table 4-13.

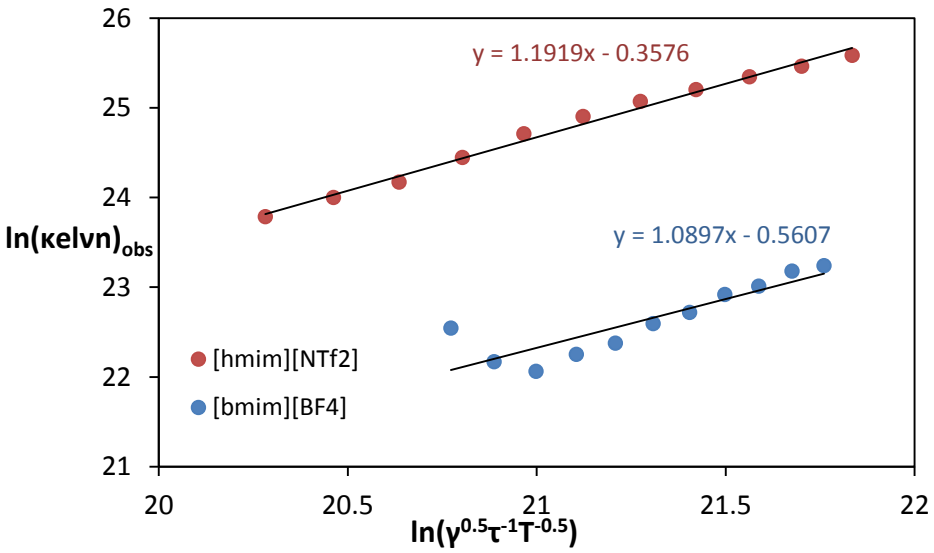

Figure 4.40: Weaver plots with temperature dependent values for the ILs [hmim$^+$][Tf_2N^-] (red) and [bmim$^+$][BF_4^-] (blue).

Table 4-13: Temperature dependent Pekar factors γ and reorganization energies for the redox couple [TCNE/TCNE$^{\bullet-}$] in different ionic liquids

Solvent	T	$\gamma^{(a)}$	$(\kappa_{el}\nu_n)_{obs}$ [$10^{10}s^{-1}$]	$\lambda_o^{(b)}$ [kJ mol^{-1}]	$\lambda_i^{(c)}$ [kJ mol^{-1}]	$\Delta G^*_{calc}{}^{(d)}$ [kJ mol^{-1}]
[$hmim^+$][Tf_2N^-]	288	0.410	2.14	54.62	12.61	12.12
	293	0.409	2.65	54.55	12.99	12.15
	298	0.409	3.14	54.48	13.36	12.18
	303	0.408	4.13	54.41	13.72	12.21
	308	0.407	5.38	54.33	14.07	12.24
	313	0.407	6.51	54.25	14.42	12.26
	318	0.406	7.72	54.16	12.61	12.28
	323	0.405	8.81	54.07	12.99	12.30
	328	0.405	10.2	53.97	13.36	12.32
	333	0.404	11.4	53.86	13.72	12.34
	338	0.403	12.9	53.75	14.07	12.36
[$bmim^+$][BF_4^-]	288	0.421	0.618	56.17	12.66	12.51
	293	0.421	0.425	56.16	12.85	12.55
	298	0.421	0.381	56.15	13.04	12.60
	303	0.421	0.460	56.13	13.22	12.64
	308	0.421	0.523	56.11	13.41	12.68
	313	0.421	0.648	56.09	13.59	12.72
	318	0.420	0.736	56.07	13.77	12.76
	323	0.420	0.896	56.04	13.95	12.80
	328	0.420	0.984	56.01	14.12	12.83
	333	0.420	1.17	55.98	14.30	12.87
	338	0.419	1.24	55.94	14.47	12.90

(a)…Pekar factor calculated via $\gamma=1/n_D^2-1/\varepsilon$

(b)…calculated via equation (2.21)

(c)…calculated via equation (2.20), used $\lambda i\infty$=27.2 kJ/mol[59]

(d)…calculated via equation (2.15), used V_{RP}=4.7 kJ/mol[20]

For both ILs slopes of approximately unity are obtained which indicates a dependence of the pre-exponential factor on the longitudinal relaxation times τ_L, as suggested by Weaver for the adiabatic case. But, the plot results in straight lines with slightly different slopes. This possibly explains the behaviour in Figure 4.36, the reason therefore could be a potentially different reaction distance in the different ILs. But, we now can conclude that the electron transfer in the ILs seems to be adiabatic. Now it is possible to determine an experimental value for g(r,d) via equations (2.44) and (2.45). The temperature dependence was included by the application of γ/T.

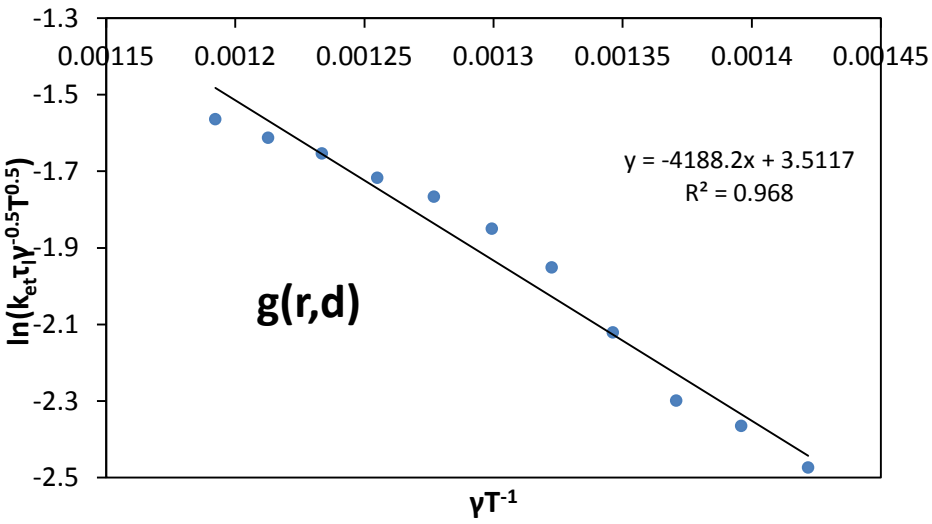

Figure 4.41: Determination of g(r,d) of the redox couple [TCNE/TCNE$^{\bullet-}$] in [hmim$^+$][Tf_2N^-]. Calculations of the Pekar factor via n_D^2.

For comparison, the same plot as above with Pekar factors calculated via ε_∞ shows in Figure 4.42 a nonlinear dependence. This makes no sense and was crucial to decide in the following and in the calculations for Figure 4.40 the Pekar factors calculated via the refractive indices will be solely concentrate on.

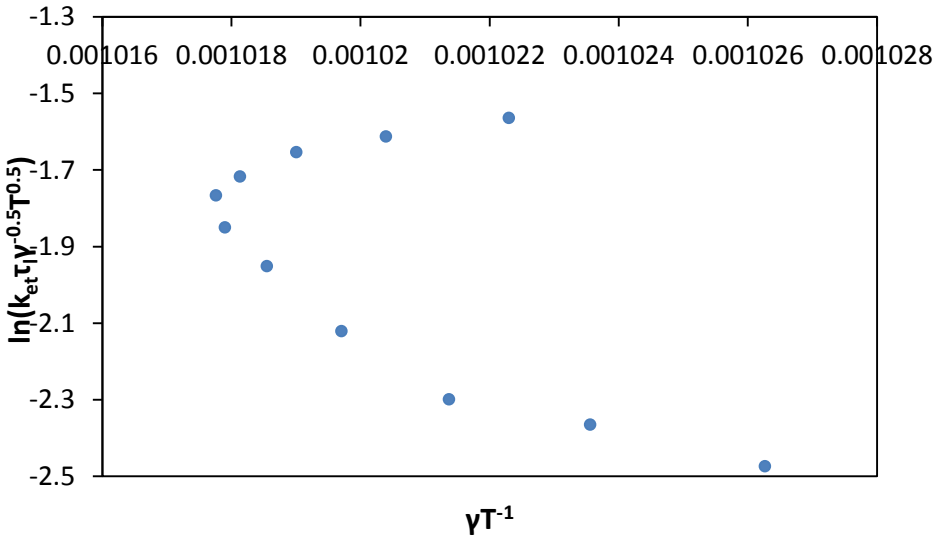

Figure 4.42: Determination of g(r,d) of the redox couple [TCNE/TCNE$^{\bullet-}$] in [hmim$^+$][Tf_2N^-]. Calculations of the Pekar factor via ε_∞

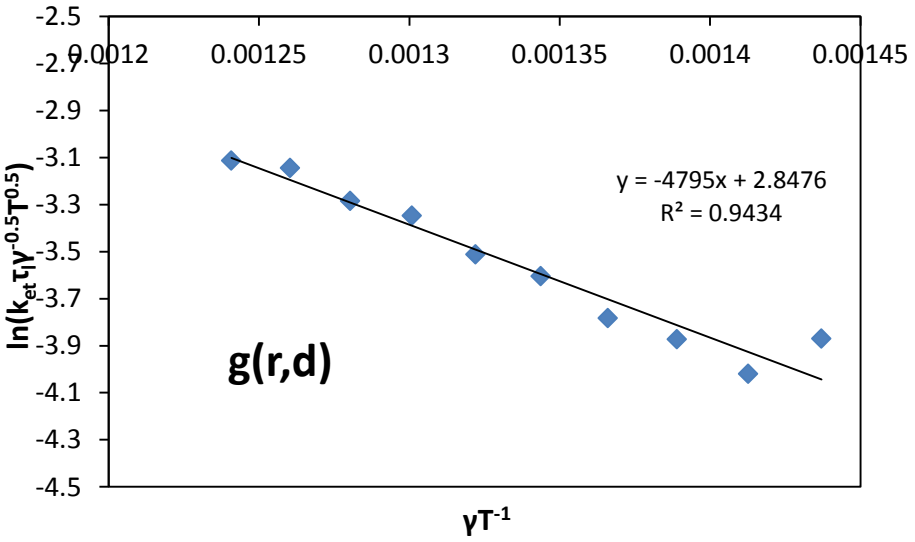

Figure 4.43: Determination of g(r,d) of the redoxcouple [TCNE/TCNE$^{\bullet-}$] in [bmim$^+$][BF_4^-].

The obtained experimental values for $g(r,d)_{exp}$ and d_{exp} are listed in Table 4-14. The observed distance in the precursor complex of the redox couple [TCNE/TCNE$^{\bullet-}$] in the IL [hmim$^+$][Tf_2N^-] is with 4.5 Å in a very good agreement with the 4.4 Å distance in nonethereal solvents published in ref. [20]. The reaction distance in the IL [bmim$^+$][BF_4^-] is

with 4.8 Å slightly larger but this discrepancy is within the given error margin (see Table 4-14).

Table 4-14: Experimental values for g(r,d) and the resulted experimental reaction distance d_{exp}

Solvent	$g(r,d)_{exp}$ [10^8 m^{-1}]	$d_{exp}^{(a)}$ [nm]
$[hmim^+][Tf_2N^-]$	10.0±0.6	0.45±0.01
$[bmim^+][BF_4^-]$	11±1	0.48±0.02

(a) calculation via equation(2.24) with $g(r,d)_{exp}$

4.3.2 Activation energies / Discussion

For the calculation via the Arrhenius plots, only the temperature ranges with published solvent parameters were used. The data used for each measured IL are plotted together in Figure 4.44. Resulting activation energies E_a, obtained from the slopes are listed in Table 4-15.

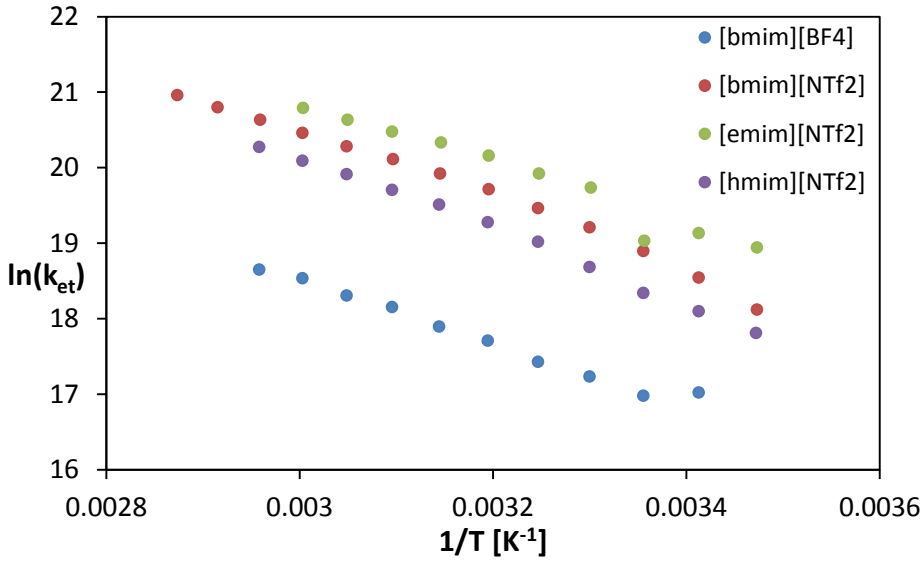

Figure 4.44: Arhenius plots for the self- exchange reaction of the redox couple [TCNE/$TCNE^{\bullet-}$] in different ionic liquids.

Table 4-15: Activation energies E_a, activation enthalphies of the viscosity H_η and activation enthalpies of the relaxation process H_τ of self- exchange reaction of the redox couple [TCNE/$TCNE^{\bullet-}$] in different ionic liquids.

solvent	E_a [kJ mol^{-1}]	H_η [kJ mol^{-1}]	H_τ [kJ mol^{-1}]	temperature range [K]
[$bmim^+$][Tf_2N^-]	38±1[(a)]	27.6±0.5	-	288 - 348
[$emim^+$][Tf_2N^-]	35±2[(a)]	24.8±0.1	-	288 – 333
[$hmim^+$][Tf_2N^-]	40.7±0.9[(a)]	31.7±0.5	27±3	288 - 338
[$bmim^+$][BF_4^-]	35.7±0.7[(a)]	33.1±0.5	17±3	298 - 338

H_τ from $\ln\tau$ = const + H_τ/RT, H_η from $\ln\eta$ = const + H_η/RT

τ…longitudinal relaxation time

[(a)]…from $\ln k_{et}$=ln A – E_a/RT

Based on the assumption mentioned before that the electron transfer appears adiabatic, the ΔG^*_{exp} were obtained via equation (4.1) described in chapter 4.1.1.

For the solvents with no data available for calculations of values of the longitudinal relaxation energy H_τ the approximation $H_\tau \approx H_\eta$ was used. The comparison of H_τ and H_η values in Table 4-15 indeed shows that this approximation is not really perfect. H_η for the IL [$bmim^+$][BF_4^-] is almost twice as high than the value for H_τ. The so obtained ΔG^*_{exp} are listed in the direct comparison to the calculated ones ΔG^*_{calc} in Table 4-16. Additionally, calculated energies are listed using the experimental g(r,d) values out of Table 4-14.

Table 4-16: Comparison of the calculated and experimental free Gibbs energies for the electron transfer reaction of the redox couple [TCNE/$TCNE^{\bullet-}$]

solvent	ΔG^*_{exp} [kJ mol^{-1}]	ΔG^*_{calc}[(a)] [kJ mol^{-1}]	$\Delta G^*_{calc,dexp}$[(b)] [kJ mol^{-1}]	temperature range [K]
[$bmim^+$][Tf_2N^-]	10±2	12.03	-	288 - 348
[$emim^+$][Tf_2N^-]	11±2	12.31	-	288 – 333
[$hmim^+$][Tf_2N^-]	14±1	12.18	12.75	288 - 338
[$bmim^+$][BF_4^-]	18±1	12.59	15.36	298 - 338

(a) calculated via equation (2.15), using V_{RP}=4.7 kJ mol^{-1}[20] and $\lambda i\infty$=27.2 kJ mol^{-1}[59]

(b) calculated via equation (2.15) with λ_o calculated via equation (2.21) with $g(r,d)_{exp}$ from Table 4-14, using V_{RP}=4. kJ mol^{-1}[20] and $\lambda i\infty$=27.2 kJ mol^{-1}[59]

By using experimental values of ΔG^*_{exp} for a Weaver plot in Figure 4.36, a straight line with slope of unity is found (see Figure 4.45). This indicates clearly that the calculation of the Marcus energy via the reorganization energy given by $\lambda/4\text{-}V_{RP}$ seems to be incorrect. The used V_{RP} = 4.7 kJ mol^{-1} does not influence the slope in the weaver plot. This leads to the assumption that just the calculation of the reorganization energy λ failed. The comparison in Table 4-16 shows that the ΔG^*_{calc} values for the listed ILs are very similar which could not confirmed by the experimental values ΔG^*_{exp}. One reason for that could be the reaction distance, d. By using the experimental g(r,d) values extracted from Table 4-14 for the calculation of $\Delta G^*_{calc.obs}$ changes the situation a bit (see Table 4-16, column 4). Especially in ILs it is conceivable that the reaction distance of precursor complex is dependent on the solvent because the ILs has, as already mentioned before, an ordered structure like in a crystal. The structure in the ILs [6, 9, 25, 51] and their cavities in between the alternating pattern could influence the reaction distance a bit. Another reason for an insufficient λ calculation is, as already mentioned before, the Pekar factor. The calculation of the λ_o via the dielectric continuum model as suggested by Marcus is still questionable and the produced errors in calculations via this model are conceivable.

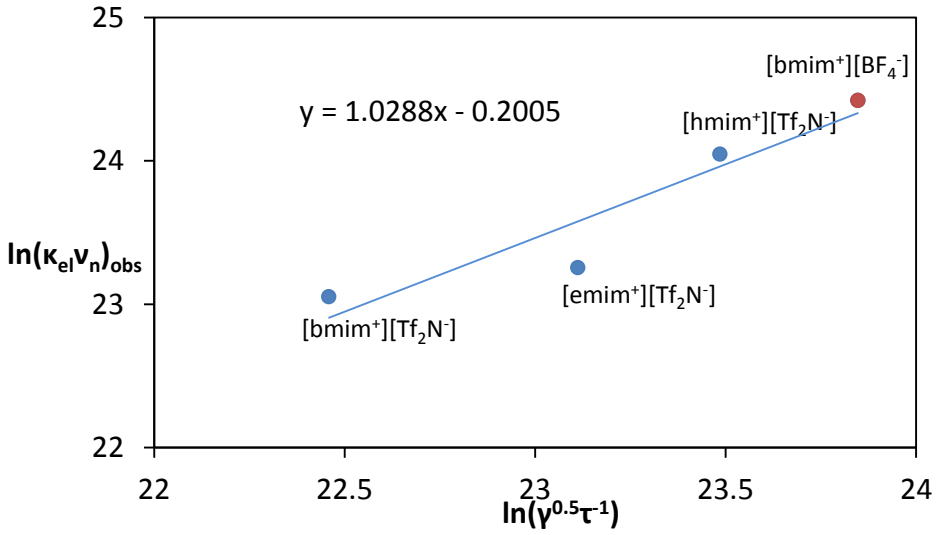

Figure 4.45: Weaver plot with experimental observed ΔG* values and pekar factors calculated via the refractive indices.

4.4 Self-exchange reaction of [DDQ/DDQ$^{\bullet-}$] in the solvent mixtures

ESR spectra from DDQ$^{\bullet-}$ radical anion were recorded in different solvent mixtures as listed in chapter 3.1.8. The concentration of the radical [DDQ$^{\bullet-}$] in the solution was kept constant at approximately $1 \cdot 10^{-4}$ M. A concentration change by added neutral substance [DDQ] gave rise to the line broadening effect. The exchange rates received from the simulation in dependence on [DDQ] are displayed in the following plots.

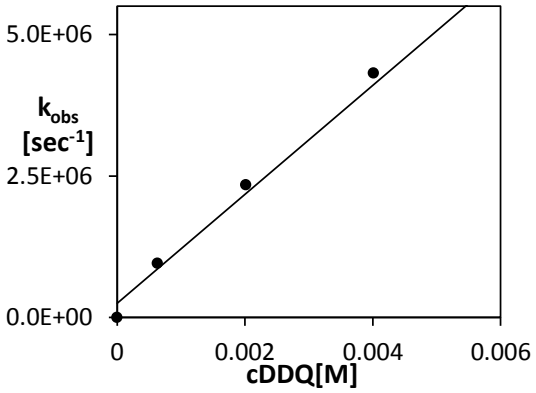

Figure 4.46: Observed rates 298 K in dependence of [DDQ] in solvent mixture M1a

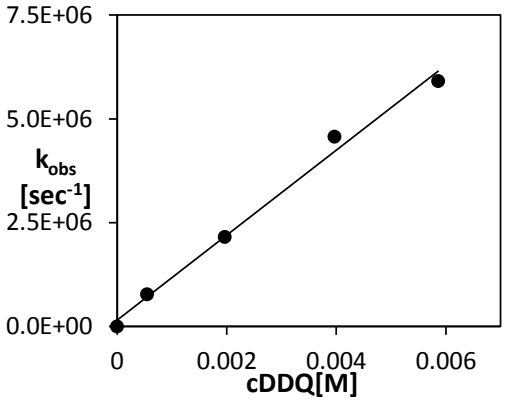

Figure 4.47: Observed rates 298 K in dependence of [DDQ] in solvent mixture M1b

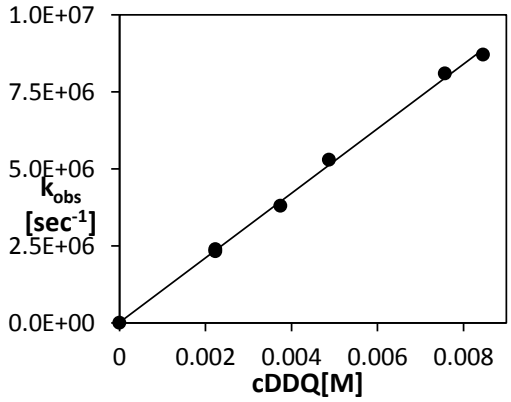

Figure 4.48: Observed rates 298 K in dependence of [DDQ] in solvent mixture M1c

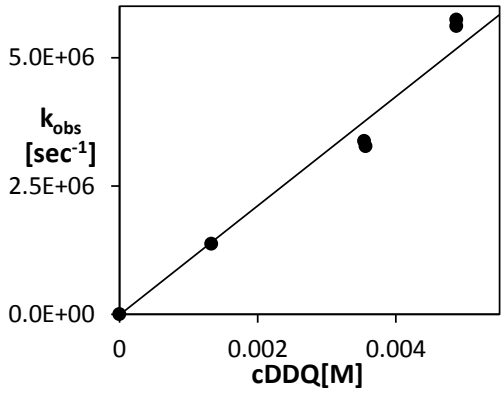

Figure 4.49: Observed rates 298 K in dependence of [DDQ] in solvent mixture M1d.

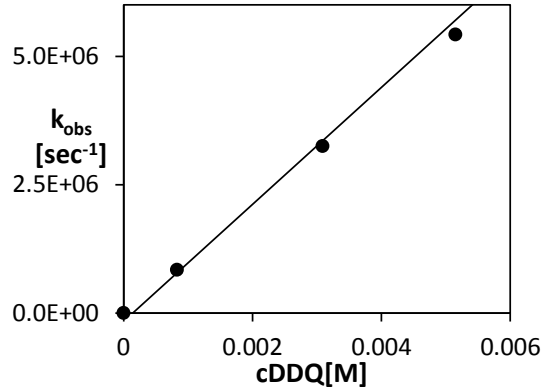

Figure 4.50: Observed rates 298 K in dependence of [DDQ] in solvent mixture M1f.

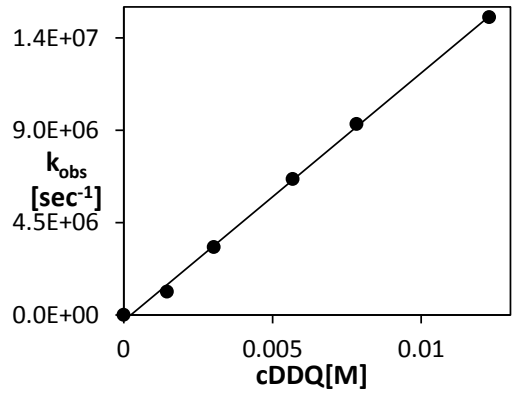

Figure 4.51: Observed rates 298 K in dependence of [DDQ] in solvent mixture M1e.

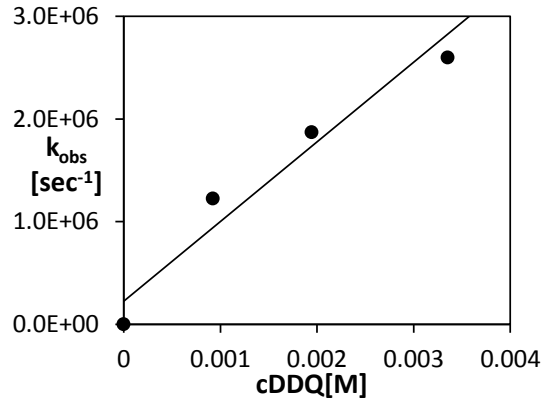

Figure 4.52: Observed rates 288 K in dependence of [DDQ] in solvent mixture M1j.

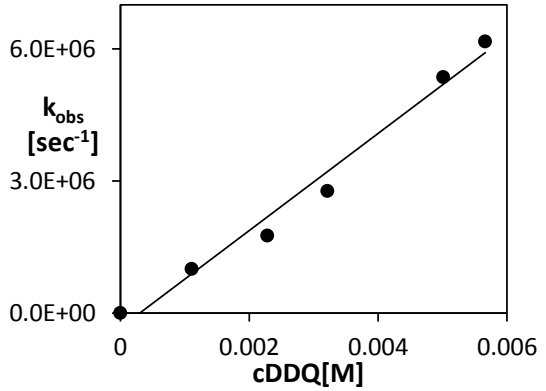

Figure 4.53: Observed rates at 288 K in dependence of [DDQ] in solvent mixture M1h.

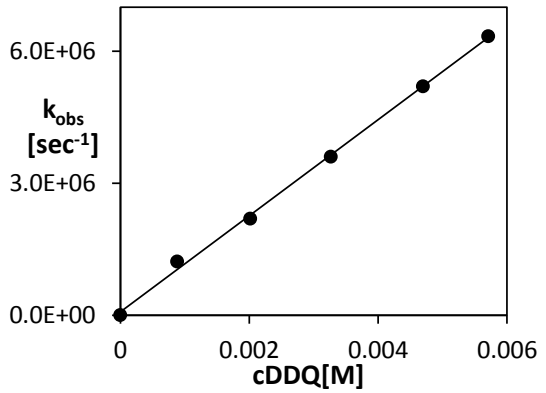

Figure 4.54: Observed rates at 288 K in dependence of [DDQ] in solvent mixture M1i.

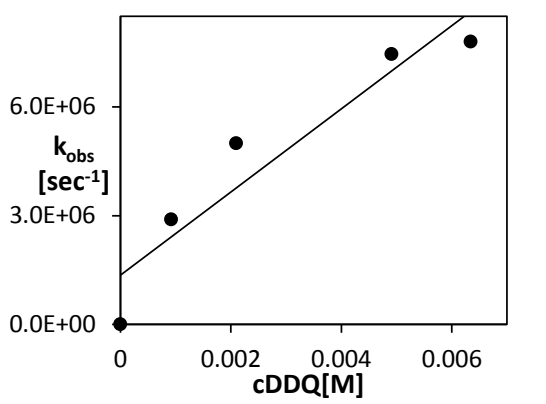

Figure 4.55: Observed rates at 328 K in dependence of [DDQ] in solvent mixture M155b.

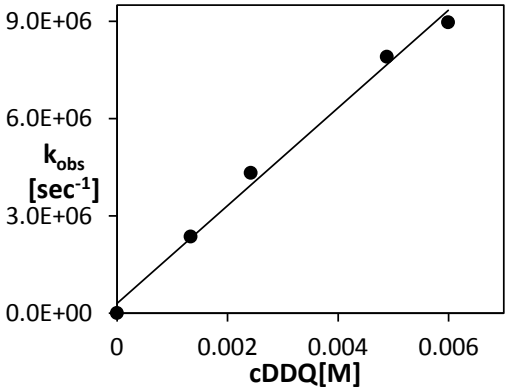

Figure 4.56: Observed rates at 328 K in dependence of [DDQ] in solvent mixture M155c.

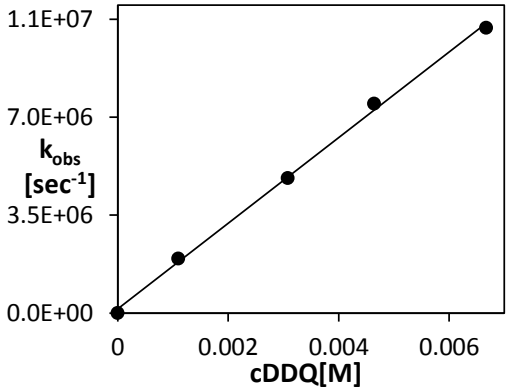

Figure 4.57: Observed rates at 328 K in dependence of [DDQ] in solvent mixture M155e.

The bimolecular rate constants k_{obs} observed from the slopes in Figure 4.46 - Figure 4.57 are listed in Table 4-17 together with the calculated rate constants of diffusion k_{diff} and the rate constants of the electron transfer k_{et}.

Table 4-17: Rates for the self-exchange reaction of [DDQ/DDQ$^{\bullet-}$] in different solvent mixtures at given temperature. Observed rate constants k_{obs}, electron transfer rates k_{et} (via equation (2.8)) and rates for diffusion k_{diff} (via equation (2.11)).

Solvent mixture	T [K]	ε_s	k_{obs} [$10^8 M^{-1}s^{-1}$]	k_{diff} [$10^{10} M^{-1}s^{-1}$]	k_{et} [$10^8 M^{-1}s^{-1}$]
M1a	298	5.9	9.1±0.4	1.077	11.0±0.6
M1b	298	8.6	9.9±0.7	1.091	13±1
M1c	298	11.6	10.5±0.3	1.090	13.3±0.4
M1d	298	15.1	10.7±0.6	1.082	16±1
M1e	298	18.7	12.3±0.2	1.090	14.7±0.3
M1f	298	23.4	11.6±0.4	1.091	12.1±0.6
M1j	288	8.9	7.4±0.5	1.017	86.6±0.7
M1h	288	16	11.8±0.9	1.016	15±2
M1i	288	25.2	10.7±0.3	1.014	13.6±0.5
M155b	328	7.5	9±2	1.207	10±2
M155c	328	9.6	14.3±0.9	1.202	19±2
M155e	328	14.8	14.9±0.4	1.202	19.9±0.8

4.4.1 Solvent dynamics

Weaver plots were used to clarify if there is a solvent dynamic effect as described in chapter 2.4 . The self- exchange reaction of the redox couple [DDQ/DDQ$^{\bullet-}$] is in organic solvents controlled by adiabatic solvent dynamics as published by Grampp et al. [21]. To prove the adiabatic solvent dynamic effect in the solvent mixtures, plots were made according equation (2.42), which should result in a slope of unity for the adiabatic case.

Table 4-18: temperature dependent Pekar factors γ and reorganization energies for the redox couple [DDQ/DDQ$^{\bullet-}$] in different solvent mixtures at at given temperatures.

Solvent mixture	T	γ(a)	τL [ps]	$(\kappa_{el}\nu_n)_{obs}$ [$10^{11}s^{-1}$]	λ_o [b] [kJ mol^{-1}]	ΔG^*_{calc} [c] [kJ mol^{-1}]
M1a	298	0.349	26.6	8.3	46.10	3.03
M1b	298	0.402	17.6	18.5	53.07	4.77
M1c	298	0.433	12.5	29.6	57.11	5.78
M1d	298	0.452	9.1	39.2	59.64	6.41
M1e	298	0.465	6.9	56.2	61.41	6.85
M1f	298	0.476	5.2	59.7	62.82	7.20
M1j	288	0.407	17.9	17.3	53.77	4.80
M1h	288	0.458	9.0	61.4	60.39	6.46
M1i	288	0.480	5.1	73.6	63.31	7.19
M155b	328	0.376	18.5	6.91	49.64	4.32
M155c	328	0.406	13.8	17.7	53.53	5.29
M155e	328	0.442	8.1	29.0	58.27	6.48

[a]…pekar factor calculated via $\gamma=1/n_D^2-1/\varepsilon$

[b]…calculated via equation (2.21)

[c]…calculated via equation (2.15), used V_{RP}=13.4 kJmol^{-1} [20] and λ_i calculated via eq.(2.20) with λ_∞=40.9 kJmol^{-1}

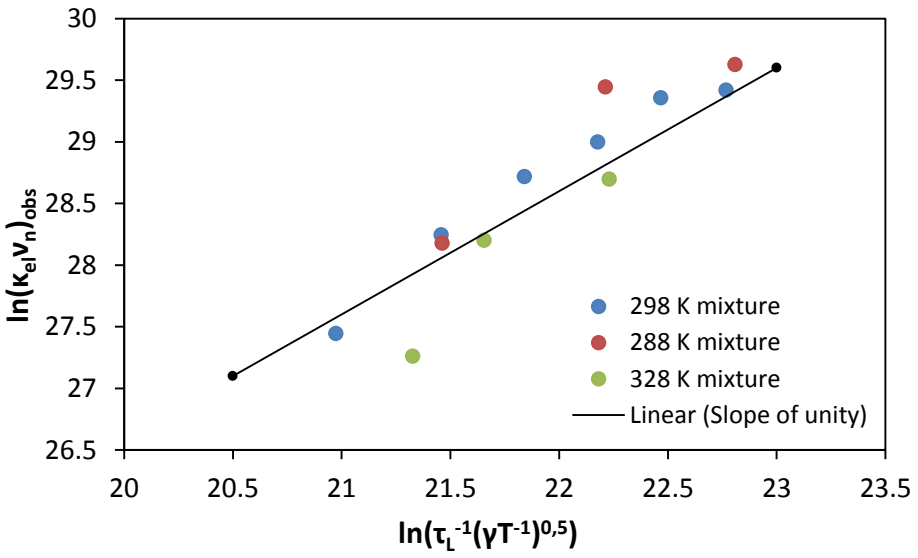

Figure 4.58: Weaver plot for the adiabatic case with calculated ΔG* values.

The plot in Figure 4.58 confirmed the adiabatic solvent dynamic effect. This allows a determination of an experimental value for g(r,d) via the slope of the line in Figure 4.59.

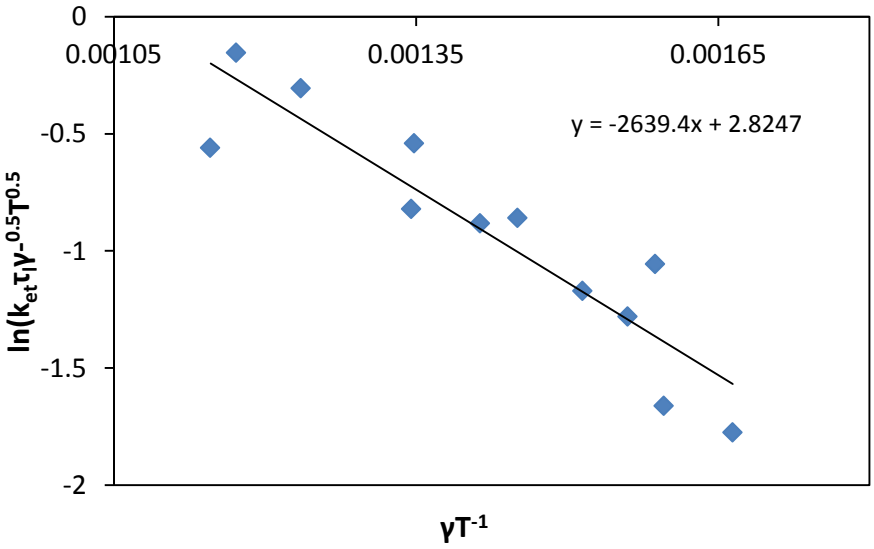

Figure 4.59: Determination of $g(r,d)_{exp}$ via equations equations (2.44) and (2.45).

This resulted in an experimental value for $g(r,d)_{exp}$ of $6.23 \cdot 10^{8} m^{-1}$ and this in turn results in an experimental reaction distance d_{exp} of 2.7Å by using equation (2.24) with an r = 2.3Å. This reaction distance is in a good agreement with literature values of 2.9 and 3.0 Å respectively (for references see Table 3-37).

4.5 Self- exchange reaction of [TCNE/TCNE$^{\bullet-}$] in the solvent mixtures

The self-exchange reaction of the redox couple [TCNE/TCNE$^{\bullet-}$] were also investigated in the solvent mixtures. The composition of the used mixtures is described in chapter 3.1.8. The following graphs show the observed exchange rates k_{obs} in dependence of the concentration neutral TCNE.

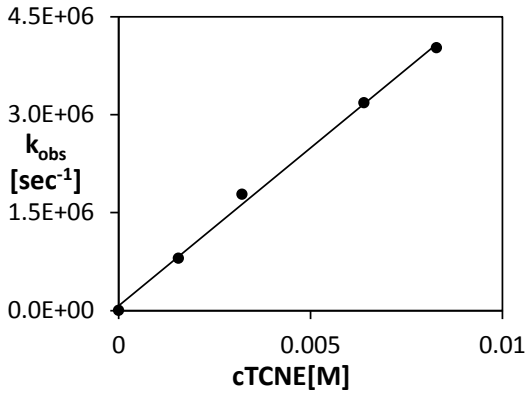

Figure 4.60: Observed rates 298 K in dependence of [TCNE] in solvent mixture M1a

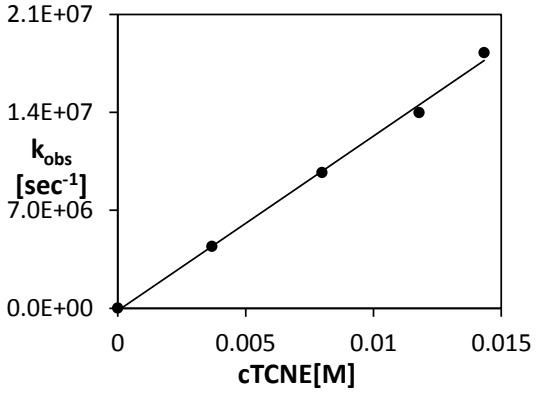

Figure 4.62: Observed rates 298 K in dependence of [TCNE] in solvent mixture M1d

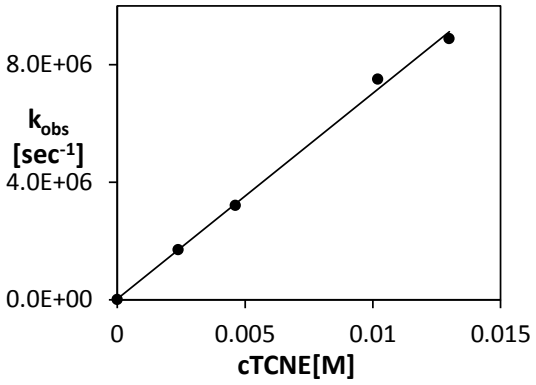

Figure 4.61: Observed rates 298 K in dependence of [TCNE] in solvent mixture M1b

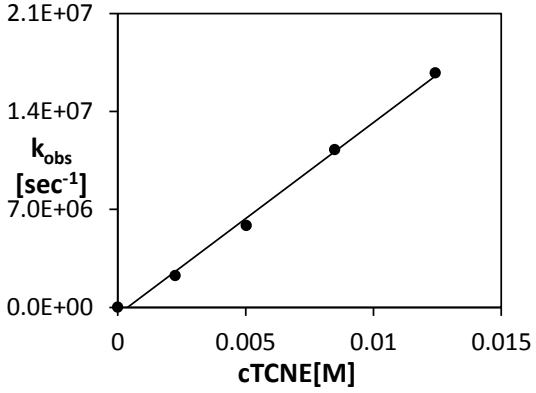

Figure 4.63: Observed rates 298 K in dependence of [TCNE] in solvent mixture M1f

The slopes of the lines in the figures above give the bimolecular rate constants of the redox couple [TCNE/$TCNE^{\bullet-}$] in the different solvent mixtures. The so obtained rate constants k_{obs} and the rate constants of electron transfer k_{et}, calculated via equation (2.8) with k_{diff} from equation (2.11), are listed in the following table.

Table 4-19: Rates for the self-exchange reaction of [TCNE/TCNE$^{\bullet-}$] in different solvent mixtures at 298 K. Observed rate constants k_{obs} ,electron transfer rates k_{et} (via equation (2.8)) and rates for diffusion k_{diff} (via equation (2.11)).

Solvent mixture	T [K]	ε_S	k_{obs} [$10^8 M^{-1}s^{-1}$]	k_{diff} [$10^{10} M^{-1}s^{-1}$]	k_{et} [$10^8 M^{-1}s^{-1}$]
M1a	298	5.9	4.7±0.2	1.077	5.1±0.2
M1b	298	8.6	6.9±0.3	1.091	8.0±0.5
M1d	298	15.1	12.7±0.7	1.082	16±1
M1e	298	18.7	12.9±0.5	1.089	17±1
M1f	298	23.4	14.4±0.3	1.091	19.5±0.6

4.5.1 Solvent dynamics

A Weaver plot (Figure 4.64) was done to prove the adiabatic solvent dynamic effect in the solvent mixtures. A plot was made according to equation (2.42), which should result in a slope of unity for the adiabatic case. The used values for the plot in Figure 4.64 are listed in Table 4-20.

Table 4-20: Temperature dependent Pekar factors γ and reorganization energies for the redox couple [TCNE/TCNE$^{\bullet-}$] in different solvent mixtures at 298 K.

Solvent mixture	T	$\gamma^{(a)}$	τ_L / ps	$(\kappa_{el}\nu_n)_{obs}$ [$10^{10}s^{-1}$]	$\lambda o^{(b)}$ [kJ mol^{-1}]	$\Delta G^*_{calc}{}^{(d)}$ [kJ mol^{-1}]
M1a	298	0.349	26.6	23.4	46.59	10.46
M1b	298	0.402	17.6	73.4	53.62	12.22
M1d	298	0.452	9.1	299	60.26	13.87
M1e	298	0.465	6.9	364	62.05	14.32
M1f	298	0.476	5.1	485	63.47	14.68

(a)…Pekar factor calculated via $\gamma=1/n_D^2-1/\varepsilon$

(b)…calculated via equation (2.21)

λ_i=13.36 is calculated via equation (2.20), used λ_i^{∞}=27.1 kJ/mol[59]

(d)…calculated via equation (2.15), used V_{RP}=4.7 kJ/mol[20]

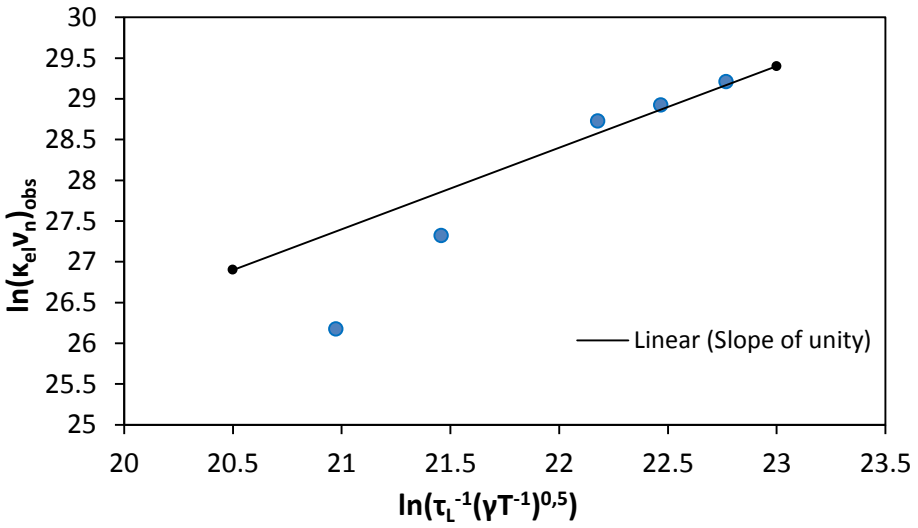

Figure 4.64: Weaver plot for the adiabatic case with calculated ΔG* values. A linear with a slope of unity is marked in the picture.

The figure above indicates that three solvent mixtures are on the line but the other two drifting from the linearity. The mixtures, which are drifting from the line, are M1a and M1b. Those are composed of a high molar fraction of propyl acetate as described in chapter 3.1.8. This brings again the assumption that the reaction distance in the precursor complex is dependent on the solvent. Grampp et al.[20] found a differentiation between ethereal and non-ethereal solvents. This would fit to the present results that in the mixtures with dominant ethereal molar fractions the values drifting from the ones with explicit lower molar fractions of propyl acetate. To prove this assumption, experimental rate constants from ref. [20] were used to calculate $(\kappa_{el}\nu_n)_{obs}$ with the same data for λ_i and V_{RP} as given at Table 4-20.

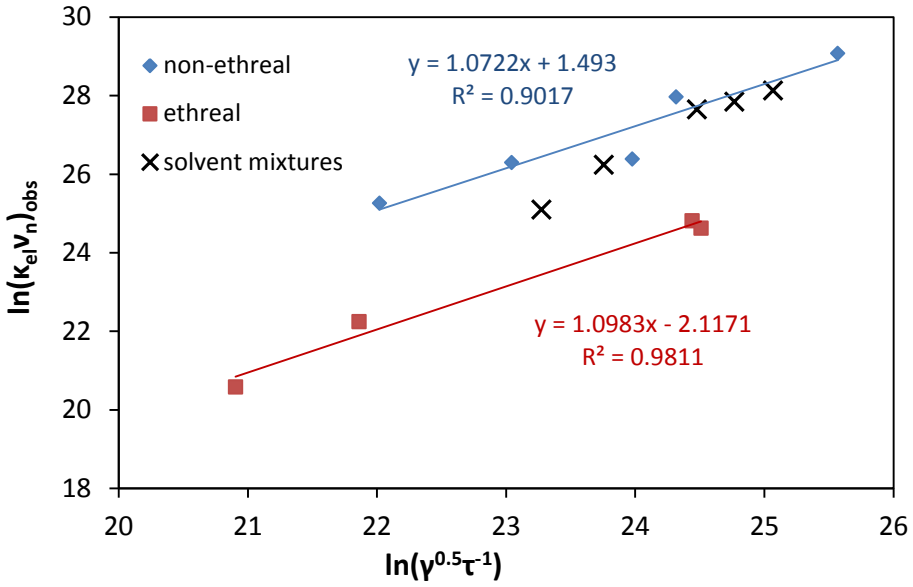

Figure 4.65: Weaver plot with points calculated with exp. data of ket extracted from ref. [20] **in ethereal (blue) and in non-ethereal together with values of this work (black).**

Figure 4.65 supports this assumption clearly. The solvent mixtures with lower molar fractions of propyl acetate are nicely in line with the results extracted from ref. [20], whereas the solvent mixtures with high molar fractions of propyl acetate seems to drift to the other line for ethereal solvents.

5. Conclusion and Outlook

In the course of this work the self-exchange reaction of three different redox couples, tetracyanoethylene and its radical anion [$TCNE^{\bullet-}$/TCNE], 2,3-dichloro-5,6-dicyanobenzoquinone and its radical anion [$DDQ^{\bullet-}$/DDQ] and tetrathiavulvalene and its radical cation [$TTF^{\bullet+}$/TTF], was investigated. The self-exchange reactions of the mentioned redox couples were investigated in different ionic liquids, organic solvents as well as special solvent mixtures under variation of temperature and pressure. To investigate the solvent dependences on the rate constants it was necessary to have a good knowledge related to various solvent properties like the viscosity η, the refractive index n_D the density ρ and the dielectric parameters such as the static dielectric constant ε_S, the optical dielectric constant ε_∞ and longitudinal relaxation time τ_L. To find trustworthy values of these solvent properties in dependence of temperature and pressure was a challenge by itself. Especially to find values at elevated pressures in literature is very difficult. Some of the viscosity and density data were measured within this work in dependence on temperature. Furthermore was it necessary to purify the used ILs for measurements with the redox couple [$TCNE^{\bullet-}$/TCNE]. Indeed the purchased ILs are of a very good purity grade but a very small amount of disturbing reducing impurity (methylimidazolium) had to be removed before the investigations on [$TCNE^{\bullet-}$/TCNE] could be started. Appropriate purification methods for the investigated ILs were successfully found.

To investigate the self-exchange reactions in dependence of pressure it was first necessary to build a high-pressure ESR cell which is tight until pressures as much as possible. The formerly used high pressure ESR cell withstands only pressures until 50 MPa. With the new designed ESR cell, made of a bent quartz capillary, was it possible to do ESR high-pressure experiments until 100 MPa.

The electron self-exchange reaction of the redox couple [$TTF^{\bullet+}$/TTF] investigated in the ILs [$emim^+$][Tf_2N^-] and [$bmim^+$][Tf_2N^-] is diffusion controlled. This was shown by the results from the temperature dependent experiments. This behaviour allows no conclusions about

the applicability of the Marcus Theory because it is not possible to extract any rate constants for the electron transfer. The observed rate constants are in a very good agreement with the calculated rate constants for diffusion via the equations of Smoluchowski and Stokes-Einstein. The experimental ΔG* value of the self-exchange reaction [$TTF^{\bullet+}$/TTF] in the high viscous organic solvent DMP is not in a good agreement with the calculated once via the Marcus Theory unless the resonance splitting energy V_{RP} is negligible small. The used V_{RP} for the calculations seems to be overestimated.

The pressure dependent measurements of the self-exchange reaction [$TTF^{\bullet+}$/TTF] in the ionic liquids did not reflect the, from the temperature dependent experiments observed, diffusion control over the whole measured pressure range. Instead, after a slight pressure increase the observed rate constants deviated completely from the calculated rate constants of diffusion. The observed rate constants at higher pressures were higher than these, thus agreeing with similar publications of higher observed rate constants in very high-viscous ILs. By increasing the pressure the viscosities of the ILs gets very high and it seems that the diffusion stops completely and the redox couple is trapped in a kind of cage in the structure of the IL. Publications of cage-like liquid structures of ILs verify spaces between the layers in the IL. The size of the spaces is in the dimension of the precursor complex which confirms the assumption that the redox couple is captured in these spaces and changes the electron back and forth.

Investigations on the redox couple [$TCNE^{\bullet-}$/TCNE] were done in four different ILs, [$emim^+$][Tf_2N^-], [$bmim^+$][Tf_2N^-], [$hmim^+$][Tf_2N^-] and [$bmim^+$][BF_4^-] and five different organic solvents mixtures. The electron transfer reaction [$TCNE^{\bullet-}$/TCNE] is not diffusion controlled in the mentioned ILs, thus the measurements provided rate constants of the electron transfer and activation energies which allowed interpretations related to the Marcus Theory. The observed rate constants shows an adiabatic solvent dynamic effect and results in the determination of the reaction distances in the precursor complex, d_{exp}. The results are in a good agreement with other published values of the reaction distance. The comparison of the experimental observed ΔG* values with the calculated ones via the Marcus energies shows deviations. The calculated energies are in the same range as the

experimentally observed ones but it seems that the calculation of the reorganisation energy via Marcus failed to some extent. The experiments gave hints that possibly the reaction distance varies slightly in the different ILs. The already discussed cavity sizes present in the ionic liquid structure maybe could influence the reaction distance of the redox couple. Furthermore the calculation of the outer reorganisation energies via Marcus is based on a dielectric continuum, something which cannot be applied to ILs. A wrong calculation based on the adoption of a dielectric continuum in ILs would therefore be no surprise and makes the application of the Marcus Theory to ILs difficult. Possibly the outer reorganisation energy should be made subject to a new approach which is applicable on ILs.

The Marcus Theory however was a great tool to prove the applicability of the solvent mixtures. The investigated redox couple [$TCNE^{\bullet-}$/TCNE] in the solvent mixtures shows an adiabatic solvent dynamic effect. The results showed that the solvent dynamic effect is dependent on the fraction of propyl acetate. These results are supported by the findings of other researchers, observing that there is a difference in solvent dependence between ethereal and nonethereal solvents. A direct comparison between their results and the ones presented in this work shows a good agreement and confirmed the findings. The more extensive series of measurements with the redox couple [$DDQ^{\bullet-}$/DDQ] in twelve different solvent mixtures and three different temperatures shows also clearly an adiabatic solvent dynamic effect. The observed reaction distances are in a very good agreement with other published ones. The observed solvent effects on both tested redox couples indicates clearly that, whatever the composition, the mixture preforms like a single solvent. This understanding permits the use of the solvent mixture for investigation on chemical reactions in dependence only on the dielectric constant.

Finally, some words to the outlook with respect to the results and the aim of this work shall be summarized here. A future refinement of the high pressure cell would be beneficial for the signal to noise ratio. For this purpose, an increase in the number of bends and a closer arrangement of the single capillary strands would be an upgrade. This would simplify measurements in high viscous solvents and provide a better reproducibility. The pressure

increase rate should definitely be included in the future. Furthermore it could be of interest to combine pressure and temperature variation. This would offer a tool to investigate redox reactions in Ils at high temperatures, where the viscosity is lower, in dependence on pressure. Generally the investigation under elevated pressures of other redox couples and in different ILs, especially with different anions, could give more information about the present solvent cages. Additional temperature dependent investigations in several ILs on different redox couples, which are not diffusion controlled, are necessary to get a clear picture on the applicability of the Marcus Theory. The availability of good dielectric parameters is desirable for the future and essential to prove the validity of the calculation of the reorganization energy.

6. Bibliography

[1] Ahosseini, A. and Scurto, A.M. 2008. Viscosity of Imidazolium-Based Ionic Liquids at Elevated Pressures: Cation and Anion Effects. *Int. J. Thermophys.* 29, (2008), 1222–1243.

[2] Asano, T. and Noble, W.J.L. 1978. Activation and Reaction Volumes in Solution. *Chem. Rev.* 78, (1978), 407–489.

[3] Berdzinski, S., Horst, J., Straßburg, P. and Strehmel, V. 2013. Recombination of Lophyl Radicals in Pyrrolidinium-Based Ionic Liquids. *ChemPhysChem*. 14, (2013), 1899–1908.

[4] Bixon, M. and Jortner, J. 1993. Solvent relaxation dynamics and electron transfer. *Chemical Physics*. 176, (1993), 467–481.

[5] Brustolon, M. and Giamello, E. eds. 2009. *ELECTRON PARAMAGNETIC RESONANCE*. John Wiley & Sons, Inc., Hoboken, New Jersey.

[6] Castiglione, F., Simonutti, R., Mauri, M. and Mele, A. 2013. Cage-Like Local Structure of Ionic Liquids Revealed by a 129Xe Chemical Shift. *J. Phys. Chem. Lett.* 4, (2013), 1608−1612.

[7] Ciocirlan, O., Croitoru, O. and Iulian, O. 2011. Densities and Viscosities for Binary Mixtures of 1-Butyl-3-Methylimidazolium Tetrafluoroborate Ionic Liquid with Molecular Solvents. *J. Chem. Eng. Data*. 56, (2011), 1526–1534.

[8] Corinne Daguenet, Paul J. Dyson Ingo Krossing Alla Oleinikova John Slattery Chihiro Wakai and Weingaertner, H. 2006. Dielectric Response of Imidazolium-Based Room-Temperature Ionic Liquids. *J. Phys. Chem. B*. 110, (2006), 12682–12688.

[9] Deetlefs, M., Hardacre, C., Nieuwenhuyzen, M., Padua, A.A.H., Sheppard, O. and Soper, A.K. 2006. Liquid Structure of the Ionic Liquid 1,3-Dimethylimidazolium Bis(trifluoromethyl)sulfonylamide. *J. Phys. Chem. B*. 110, (2006), 12055–12061.

[10] Drljaca, A., Hubbard, C.D., Eldik, R. van, Asano, T., Basilevsky, M.V. and Noble, W.J. le 1998. Activation and Reaction Volumes in Solution. 3. *Chem. Rev.* 98, (1998), 2167–2289.

[11] Eberson, L. and Shaik, S.S. 1990. Electron-Transfer Reactions of Radical Anions: Do They Follow Outer- or Inner-Sphere Mechanisms? *J. Am. Chem. SOC*. 112, (1990), 4484–4489.

[12] Eldik, R. van and Klärner, F.G. 2002. *High Pressure Chemistry, Synthetic, Mechnistic and Supercritical Applications*. Wiley-VCH: Weinheim.

[13] Eldik, R.V., Asano, T. and Noble, W.J.L. 1989. Activation and Reaction Volumes in Solution. 2. *Chem. Rev.* 89, (1989), 549–688.

[14] Fawcett, W.R. 2004. *Liquids, Solutions, and Interfaces: From Classical Macroscopic Descriptions to Modern Microscopic Details*. Oxford University Press.

[15] Fawcett, W.R. Time dependence of the relaxation parameters in non-Debye solvents. *Chemical Physics Letters*. 199, 153–160.

[16] Fredlake, C.P., Crosthwaite, J.M., Hert, D.G., Aki, S.N.V.K. and Brennecke, J.F. 2004. Thermophysical Properties of Imidazolium-Based Ionic Liquids. *J. Chem. Eng. Data*. 49, (2004), 954–964.

[17] French, C.M. and Singer, N. 1956. The Conductivity of Solutions in which the Solvent Molecule is " Large." Part I. Solutions of Tetraethylammonium Picrate in Some Phtalate Esters. (1956).

[18] Ganesan, V., Rosokha, S.V. and Kochi, J.K. 2003. Isolation of the latent precursor complex in electron-transfer dynamics. Intermolecular association and self-exchange with acceptor anion radicals. *Journal of the American Chemical Society*. 125, 9 (2003), 2559–2571.

[19] German, E.D. and Kuznetsov, A.M. 1981. Outer Sphere Energy of Reorganization in Charge Transfer Processes. *Electrochim. Acta*. 26, (1981), 1595–1607.

[20] Grampp, G. and Jaenicke, W. 1991. Kinetics od diabatic and adiabatic electron exchange in organic systems. Comperison of Theory and Expperiment. *Ber. Bunsenges. Phys. Chem.* 95, (1991), 904–927.

[21] Grampp, G., Landgraf, S. and Rasmussen, K. 1999. Electron self-exchange kinetics between 2,3-dicyano-5,6-dichloro-pbenzoquinone (DDQ) and its radical anion. Part 1. Solvent dynamical effects. *J. Chem. Soc., Perkin Trans. 2*. (1999), 1897–1899.

[22] Grampp, G., Mladenova, B.Y., Kattnig, D.R. and Landgraf, S. 2006. ESR and ENDOR Investigations of the Degenerate Electron Exchange Reactions of Various Viologens in Solution. Solvent Dynamical Effects. *Applied Magnetic Resonance*. 30, (2006), 145–164.

[23] Grampp, G. and Stiegler, G. 1986. *Journal of Magnetic Resonance*. 70, (1986), 1–10.

[24] Gritti, F. and Guiochon, G. 2008. Ultra high pressure liquid chromatography Column permeability and changes of the eluent properties. *Journal of Chromatography A*. (2008), 165–179.

[25] Hardacre, C., Holbrey, J.D., Nieuwenhuyzen, M. and Youngs, T.G.A. 2007. Structure and Solvation in Ionic Liquids. *Acc. Chem. Res.* 40, (2007), 1146–1155.

[26] Harris, K.R., Kanakubo, M. and Woolf, L.A. 2007. Temperature and Pressure Dependence of the Viscosity of the Ionic Liquids 1-Hexyl-3-methylimidazolium Hexafluorophosphate and 1-Butyl-3-methylimidazolium Bis(trifluoromethylsulfonyl)imide. *J. Chem. Eng. Data*. 52, (2007), 1080–1085.

[27] Heitele, H. 1993. Dynamic Solvent Effects on Electron-Transfer Reactions. *Angew. Chem. In. Ed. EngI.* 32, (1993), 359–317.

[28] Hill, W.W., Rosenzweig, S. and Franck, E.U. 1990. The Static Constant of Methyl Cyanide to 350°C and 2000 bar. *Ber. Bunsenges. Phys. Chem.* 94, (1990), 564–568.

[29] Holstein, T. 1978. *Philos. Mag. B.* 37, (1978), 499.

[30] Hünig, S., Kießlich, G., Quast, H. and Scheutzow, D. 1973. Tetrathio-äthylene und ihre höheren Oxidationsstufen. *Liebigs Ann. Chem.* (1973), 310–323.

[31] Hynes, J.T. 1986. Outer-Sphere Electron-Transfer Reactions and Frequency-Dependent Friction. *J. Phys. Chem.* 90, (1986), 3701–3706.

[32] Jacquemin, J., Husson, P., Mayer, V. and Cibulka, I. 2007. High-Pressure Volumetric Properties of Imidazolium-Based Ionic Liquids: Effect of the Anion. *J. Chem. Eng. Data*. 52, (2007), 2204–2211.

[33] Jeschke, G. Einführung in die ESR-Spektroskopie.

[34] Johannes Hunger, Alexander Stoppa Simon Schrçdle Glenn Hefter and Buchner, R. 2009. Temperature Dependence of the Dielectric Properties and Dynamics of Ionic Liquids. *ChemPhysChem*. 10, (2009), 723–733.

[35] Käb, G., Engel, T., Lanig, H. and Schneider, F.W. 1995. The Inverted Region of Electron Transfer in Intramolecular Fluorescence Quenching of Quinolinium Betaines. *Berichte der Bunsengesellschaft für physikalische Chemie*. 99, (1995), 118–126.

[36] Kharkats, Y. 1976. *Elektrokhimiya*. 12, (1976), 1284–1291.

[37] Kharkats, Y. 1974. *Elektrokhimiya*. 10, (1974), 1137–1141.

[38] Kinjo, N. and Nakagawa, T. 1978. Viscoelastic behavior of some di(normal alkyl) phthalates. *Bull. Chem. Soc. Japan*. 51, (1978), 1024–1026.

[39] Kochi 2003. Stable (Long-Bonded) Dimers via the Quantitative Self-Association of Different Cationic, Anionic, and Uncharged -Radicals: Structures, Energetics, and Optical Transitions. *J. AM. CHEM. SOC.* 125, (2003), 12162–12171.

[40] Kokorin, A.I. ed. 2012. *Nitroxides-Theory, Experiment and Applications*. InTech.

[41] Kramers, H.A. 1940. Brownian Motion in a Field of Force and Diffusion Model of Chemical Reactions. *Physica*. (1940), 284–304.

[42] Ma, S.-H., Zhang, X.-D., Xu, H., Shen, L.-L., Zhang, X.-K. and Zhang, Q.-Y. 2001. Theoretical studies on the self-exchange electron-transfer reaction between 2,3-dicyano-5,6-dichloro-p-benzoquinone (DDQ) and its radical anion DDQ−. *Journal of Photochemistry and Photobiology A: Chemistry*. 139, (2001), 97–104.

[43] Marcus, R. 2000. Tutorial on rate constants and reorganization energies. *Journal of Electroanalytical Chemistry*. 483, 1 (2000), 2–6.

[44] Marcus, R.A. 1993. Electron transfer reactions in chemistry. Theory and experiment. *Reviews of Modern Physics*. 65, (1993), 599–610.

[45] Marcus, R.A. 1992. Electron Transfer Reactions in Chemistry: Theory and Experiment. *Nobel Lecture* (1992).

[46] MARCUS, R.A. 1960. Exchange Reactionsand Electron Transfer Reactions Including Isotopic Exchange. *Disc. Faraday Soc.* 29, (1960), 31–31.

[47] Marcus, R.A. 1965. On the Theory of Electron-Transfer Reactions. VI. Unified Treatment for Homogeneous and Electrode Reactions. *J. Chem. Phys.* 43, (1965), 679–701.

[48] Marcus, R.A. 1956. On the Theory of Oxidation-Reduction Reactions Involving Electron Transfer. I. *J. Chem. Phys.* 24, (1956), 966–978.

[49] Marcus, R.A. and Sutin, N. 1985. Electron transfers in chemistry and biology. *Biochimica et Biophysica Acta*. 811, (1985), 265–322.

[50] McCoy, J. and Hubbell, W.L. 2011. High-pressure EPR reveals conformational equilibria and volumetric properties of spin-labeled proteins. *Proceedings of the National Academy of Sciences*. 108, 4 (2011), 1331–1336.

[51] Mele, A., Roman, G., Giannone, M., Ragg, E., Fronza, G., Raos, G. and Marcon, V. 2006. The Local Structure of Ionic Liquids: Cation–Cation NOE Interactions and Internuclear Distances in Neat [BMIM][BF4] and [BDMIM]-[BF4]. *Angew. Chem. Int. Ed.* 45, (2006), 1123–1126.

[52] Muhammad, A., Mutalib, M.I.A., Wilfred, C.D., Murugesan, T. and Shafeeq, A. 2008. Thermophysical properties of 1-hexyl-3-methyl imidazolium based ionic liquids with tetrafluoroborate, hexafluorophosphate and bis(trifluoromethylsulfonyl)imide anions. *J. Chem. Thermodynamics*. 40, (2008), 1433–1438.

[53] Nakamura, K. and Shikata, T. 2010. Systematic Dielectric and NMR Study of the Ionic Liquid 1-Alkyl-3-Methyl Imidazolium. *ChemPhysChem*. 11, (2010), 285–294.

[54] Nelsen, S.F., Blackstock, S.C. and Kim, Y. 1987. Estimation of Inner Shell Marcus Terms for Amino Nitrogen Compounds by Molecular Orbital Calculations. *J. Am. Chem. Soc.* 109, (1987), 677–682.

[55] Pfund, D.M., Zemanian, T.S., Linehan, J.C., Fulton, J.L. and Yonker, C.R. 1994. Fluid Structure in Supercritical Xenon by Nuclear Magnetic Resonance Spectroscopy and Small Angle X-ray Scattering. *J. Phys. Chem*. 98, (1994), 11846–11857.

[56] Rasmussen, K. 2006. *High-Pressure ESR Spectroscopy Applied to the Kinetics of Electron Self- Exchange Reactions in Solution.* Graz University of Technology.

[57] Rasmussen, K., Hussain, T., Landgraf, S. and Grampp, G. 2012. High Pressure ESR Studies of Electron Self-Exchange Reactions of Organic Radicals in Solution. *J. Phys. Chem. A*. 116, (2012), 193–198.

[58] Rehm, D. and Weller, A. 1970. *Isr. J. Chem.* 8, (1970), 259.

[59] Ren, H., Ming, M., Ma, J. and Li, X. 2013. Theoretical Calculation of Reorganization Energy for Electron Self- Exchange Reaction by Constrained Density Functional Theory and Constrained Equilibrium Thermodynamics. *J. Phys. Chem. A*. 117, (2013), 8017−8025.

[60] Rieger, P.H. 2007. *Electron Spin Resonance*. The Royal Society of Chemistry.

[61] Rosokha, S.V. and Kochi, J.K. 2007. Continuum of Outer- and Inner-Sphere Mechanisms for Organic Electron Transfer. Steric Modulation of the Precursor Complex in Paramagnetic (Ion-Radical) Self-Exchanges. *J. Am. Chem. Soc.* 129, (2007), 3683–3697.

[62] Silverstein, T.P. 2012. Marcus Theory: Thermodynamics CAN Control the Kinetics of Electron Transfer Reactions. *J. Chem. Educ*. 89, (2012), 1159−1167.

[63] Stranks, D.R. 1974. *Pure and Applied Chemistry*. 38, (1974), 303–323.

[64] Strehmel, V., Berdzinski, S. and Rexhausen, H. 2014. Interactions between ionic liquids and radicals. *Journal of Molecular Liquids*. 192, (2014), 153–170.

[65] Swaddle, T.W. 1990. Pressure-Testing" Marcus-Hush Theories of Outer-Sphere Electron-Transfer Kinetics. *Inorganic Chemistry*. 29, (1990), 5017–5025.

[66] Swaddle, T.W. 1996. Reflections on the outer-sphere mechanism of electron transfer. *Can. J. Chem.* 74, (1996), 631–638.

[67] Taib, M.M. and Murugesan, T. 2012. Density, Refractive Index, and Excess Properties of 1-Butyl-3-methylimidazolium Tetrafluoroborate with Water and Monoethanolamine. *J. Chem. Eng. Data*. 57, (2012), 120–126.

[68] Tariq, M., Forte, P.A.S., Gomes, M.F.C., Lopes, J.N.C. and Rebelo, L.P.N. 2009. Densities and refractive indices of imidazolium- and phosphonium-based ionic liquids: Effect of temperature, alkyl chain length, and anion. *J. Chem. Thermodynamics*. 41, (2009), 790–798.

[69] Wankmüller, A. 2012. *Solvent mixtures for studying electron transfer reactions*. Graz University of Technology.

[70] Weaver, M.J. 1992. Dynamical Solvent Effects on Activated Electron-Transfer Reactions: Principles, Pitfalls, and Progress. *Chem. Rev.* 92, (1992), 463–480.

[71] Weaver, M.J. and III, G.. . M. 1990. Dynamical Solvent Effects on Electron-Transfer Processes: Recent Progress and Perspectives. *Acc. Chem. Res.* 23, (1990), 294–300.

[72] Weil, J.A., Bolton, J.R. and Wertz, J.E. 1994. *Electron Paramgnetic Resonance*. John Wiley & Sons, Inc., NY.

[73] Yakushi, K., Nishimura, S., Sugano, T. and Kuroda, H. 1980. The Structure of Tetrathiafulvalenium Perchlorate. *Acta Cryst.* B36, (1980), 358–363.

[74] Zusman, L.D. 1988. The Theory of Electron Transfer Reactions in Solvents with Two Characteristic Relaxation Times. *Chem. Phys.* 119, (1988), 51–61.

[75] Zusman, L.D. 1983. *Chem. Phys.* 80, (1983), 29.

[76] Zusman, L.D. 1980. *Chem. Phys.* 49, (1980), 295.